The Structure of Dark Matter Halos and Disk Galaxy Rotation Curves

by
Eric Hayashi
B.Sc. University of Guelph 1998
M.Sc. University of Victoria 2001

A Thesis Submitted in Partial Fulfillment of the
Requirements for the Degree of

DOCTOR OF PHILOSOPHY

in the Department of Physics and Astronomy

Supervisor: Dr. J. F. Navarro

Abstract

We investigate the mass profile of ΛCDM halos using a suite of numerical simulations spanning five decades in halo mass, from dwarf galaxies to rich galaxy clusters. These halos typically have a few million particles within the virial radius (r_{200}), allowing robust mass profile estimates down to radii within 1% of r_{200}. Our analysis confirms the proposal of Navarro, Frenk & White (NFW) that the shape of ΛCDM halo mass profiles differs strongly from a power law and depends weakly on mass. The fitting formula proposed by NFW provides a reasonably good approximation to the density and circular velocity profiles of individual halos; circular velocities typically deviate from best NFW fits by less than 10% over the radial range which is well resolved numerically. On the other hand, systematic deviations from the NFW profile are also noticeable. In particular, although the dark matter density increases monotonically toward the centre, there is no evidence for a central asymptotic power law in the density profiles. At small radii, the profile of simulated halos gets shallower with radius more gradually than the NFW profile and, as a result, NFW fits tend to underestimate the dark matter density in these regions. We propose a simple formula that reproduces the radial dependence of the slope better than the NFW profile, and so may minimize errors when extrapolating our results inward to radii not yet reliably probed by numerical simulations. We perform a direct comparison of the spherically-averaged circular velocity (V_c) profiles of dwarf- and galaxy-sized halos with Hα rotation curves of low surface brightness (LSB) galaxies from the samples of McGaugh et al. (2001), de Blok and Bosma (2002), and Swaters et al. (2003a). We find that most rotation curves in this sample (about 70%) are consistent with the structure of CDM halos. Of the remainder, 20% are irregular and cannot be well approximated by simple fitting functions, and 10% are inconsistent with CDM halos. Rotation curves in the latter category exhibit a linear rise in velocity with

radius that many authors have interpreted as a signature of solid body rotation, i.e., circular motion in a halo with a constant density core. However, simulations of a gaseous disk in a triaxial halo suggest that deviations from spherical symmetry in the shape of the potential can "mask" the presence of a cusp in a triaxial halo, as the resulting rotation curve often resembles that of a disk in solid body rotation. We conclude that the discrepancies reported between the shape of the rotation curve of low surface brightness galaxies and the structure of CDM halos may well be resolved by accounting for the complex effects of halo triaxiality on the dynamics of the gas component.

Contents

List of Tables

†Table corrected from version of chapter published in refereed journal.

List of Figures

*Figure does not appear in version of chapter published in or submitted to refereed journals.

Preface

The work described in this thesis was undertaken between May 2001 and July 2004 while the author was a Ph.D. candidate under the supervision of Prof. Julio Navarro in the Department of Physics and Astronomy at the University of Victoria.

Chapter 2 has been accepted by Monthly Notices of the Royal Astronomical Society and Chapter 4 has been submitted as a *Letter* to the Astrophysical Journal. Chapter 3 has been published as

> Navarro, J. F., Hayashi, E., Power, C., Jenkins, A. R., Frenk, C. S., White, S. D. M., Springel, V., Stadel, J., and Quinn, T. R.: 2004, *Mon. Not. R. Astron. Soc.* **349**, 1039

The simulations presented in this thesis were performed with the N-body codes `PKDGRAV`, written by Joachim Stadel and Thomas Quinn (Stadel, 2001), and `GADGET` written by Volker Springel (Springel et al., 2001), and the N-body/hydrodynamical code `GASOLINE` written by James Wadsley, Joachim Stadel, and Thomas Quinn.

This work has been supported by computing time at the following facilities: the High Performance Computing Facility at the University of Victoria, the Edinburgh Parallel Computing Centre, and the Institute for Computational Cosmology at the University of Durham.

Acknowledgments

Thanks to everyone who ever believed in me. All the teachers who helped me along the way, who will never read these words. My professors at the University of Guelph: Pal Fischer, Scott MacKenzie, Eric Poisson for a strong foundation; John Dutcher and Kari Dalnoki-Veress for showing confidence in my abilities. Past employers: Iain Campbell and Bill Teesdale at Guelph; Phil Armitage, Cliff Hargroves, Morley O'Neill and others at CRPP. Everyone at UVic who helped me during my graduate career: my supervisor Julio Navarro; David Hartwick for unrelenting enthusiasm. Fellow graduate students Dom, Jeff, Stephen et al for friendship and commiseration. Friends and collaborators: Joachim Stadel and Tom Quinn for their generosity and encouragement; Simon White for invaluable insight; Carlos Frenk - pure class. Thanks Mom and Dad for always supporting me.

This one's for

Baba Booey

Chapter 1

Introduction

Abstract

The history of dark matter in the context of galaxy formation and galactic rotation curves is briefly reviewed. The motivations for cold dark matter (CDM) theory are summarized and particle candidates for non-baryonic dark matter are identified. Modified Newtonian dynamics is briefly discussed as an alternative to dark matter. N-body simulations and their application to investigations of the structure of CDM halos are discussed. The work presented in the remainder of this thesis is outlined.

We live in a strange Universe. To the best of our current knowledge, "normal" baryonic matter represents only 5% of the total energy density of the Universe. This is the stuff that makes up the Earth and its inhabitants, as well as the luminous stars and gas that we see when looking out into the night sky. About 25% of the Universe is made up of dark matter, which at present cannot be directly detected but whose existence we infer from its gravitational influence on visible matter. The remainder is in the form of an even more mysterious "dark energy" component which is responsible for the recently discovered accelerated expansion of the Universe (Riess et al., 1998; Perlmutter et al., 1999).

Galaxies are gravitationally bound systems of stars, gas, dust and dark matter which appear in a variety of different shapes and sizes. Among his many accomplishments, the great astronomer Hubble proposed a classification system (Hubble,

1936) which grouped galaxies by their appearance into three main categories: ellipticals, spirals (or disks), and irregulars. Ellipticals and disks are very different from a kinematical standpoint. Most elliptical galaxies show little or no rotation and are "pressure-supported" by the random motions of their stars. This thesis focuses on the kinematics of "rotationally-supported" disk galaxies in which the stars, gas and dust move on nearly circular orbits about a common centre.

In the currently accepted paradigm, galaxies form at the centre of massive, extended "halos" of dark matter. The dynamics of luminous matter in galaxies are therefore strongly influenced by the internal structure of the dark matter distribution. As a result, rotation curves of disk galaxies represent an important test of the structure of dark matter halos under the assumption that the observed rotational velocity is directly proportional to the spherically-averaged circular velocity, $V_c(r) = \sqrt{GM(r)/r}$, of its host halo.

1.1 A Brief History of Dark Matter

The history of dark matter is intimately linked with the study of disk galaxy kinematics. Although dark matter, or "missing mass," was first proposed by Zwicky (1933) to explain the large velocity dispersion of galaxies in the Coma Cluster, it was subsequent observations of the rotation curves of disk galaxies that conclusively demonstrated its existence to the astronomical community. Observations of the rotation curve of Andromeda (Babcock, 1939; Rubin and Ford, 1970; Roberts and Whitehurst, 1975) and of other galaxies (Rogstad and Shostak, 1972) indicated that the rotational velocity of material in the outer regions of disks remains roughly constant with radius, contrary to the expected Keplerian fall-off if the mass of the galaxy was concentrated in the form of visible matter. In particular, Roberts and Whitehurst (1975) estimated that the mass-to-light ratio in the outer parts of Andromeda was $\gtrsim 200\ M_\odot/L_\odot$.

Further support for the existence of dark matter was provided by the theoretical arguments of Ostriker and Peebles (1973) who concluded that a massive spherical component is needed to stabilize galactic disks from bar instabilities. In another influential paper, Ostriker et al. (1974) compiled evidence from a variety of observational sources which strongly indicated that the mass of disk galaxies increases with radius. These authors estimated a mass-to-light ratio of $\simeq 200\ M_{\odot}/L_{\odot}$ for the Local Group of galaxies (the Milky Way and Andromeda) and used this to estimate a cosmological mass density of $\Omega \simeq 0.2$,[†] remarkably close to the currently accepted value of $\Omega \simeq 0.27$ (Bennett et al., 2003).

According to the review of van den Bergh (1999), "By 1975 the majority of astronomers had become convinced that missing mass existed in cosmologically significant amounts." It was in this context that White and Rees (1978) proposed their classic "Core condensation in heavy halos" scenario which formed the basis of a new paradigm for galaxy formation in a dark matter-dominated universe. In this picture, the dissipational collapse of gas in the gravitational potential wells provided by the dark matter results in highly concentrated luminous cores embedded in extensive dark halos.

As a result, dark matter assumed a crucial role in the theory of galaxy formation, despite the fact that its identity was, and to a large extent still remains, a mystery. Big Bang Nucleosynthesis (BBN) calculations (Wagoner et al., 1967) and the small amplitude of fluctuations in the cosmic microwave background (CMB) both indicated a density in baryonic matter of only $\Omega_b \simeq 0.04$. Neutrinos were first suggested as a non-baryonic dark matter candidate because they were a known, electrically neutral (a requirement for a non-radiating form of matter) particle that possibly had a nonzero rest mass. Because they are highly relativistic at the time of decoupling from the CMB, neutrinos are known as "hot dark matter." Cold dark matter (CDM),

[†]The cosmological density parameter, $\Omega \equiv \rho/\rho_{\rm crit}$, is defined as the density expressed in units of the critical density required for a spatially flat universe

made up of particles with negligible thermal velocities, was subsequently proposed as an alternative by Peebles (1982) and Blumenthal et al. (1984). In a seminal series of papers, White et al. (1983), White et al. (1984), Davis et al. (1985), and White et al. (1987) used cosmological N-body simulations to investigate the clustering properties of the two dark matter models. These authors concluded that the "top-down" structure formation process in hot dark matter-dominated cosmogonies results in galaxies that are not clustered strongly enough, and galaxy clusters that are too large to be consistent with observations. Their simulations strongly favoured the "bottom-up," or hierarchical, clustering of CDM-dominated cosmogonies, which exhibit much better agreement with the observed distribution of galaxies.

1.2 What is the Dark Matter?

Concurrent with these developments and adding confusion to the situation was a measurement for the mass of the electron neutrino of 30 eV/c^2 by a Russian experiment (Lyubimov et al., 1980). This result was significant because it implied a mass density in neutrinos that was a significant fraction of the critical density, and therefore suggested that neutrinos might make up all of the non-baryonic dark matter. In subsequent years, however, this result was invalidated by follow-up experiments by a number of groups and current estimates based on neutrino detector experiments place the contribution of neutrinos at $\Omega_\nu \simeq 0.003$ (Turner, 1999). Parenthetically, we note that this is approximately equal to the contribution in visible stars and gas, and that most of the cosmic baryons predicted by BBN have yet to be accounted for. This so-called "dim matter" may be in the form of failed stars ("brown dwarfs") or massive black holes, but Fukugita et al. (1998) argue that it mostly consists of diffuse warm gas ($T \simeq 10^6$ K) in groups and clusters of galaxies that is difficult to detect.

The best candidates for non-baryonic dark matter are presently the axion and the neutralino. The axion is a very light, 10^{-6} to 10^{-4} eV-mass particle produced

by a symmetry in quantum chromodynamics (QCD) introduced by Peccei and Quinn (1977) to solve the strong CP (charge-parity) violation problem. Although axions are extremely light, they were produced nonthermally by oscillations in a scalar field, and can therefore be very cold. Axions are potentially detectable through their weak coupling to electromagnetism: in the presence of a strong magnetic field, the axionic dark matter could resonantly decay into two photons. Experiments to detect axions via this decay signature have thus far proven unsuccessful (Rosenberg, 1998).

The neutralino belongs to a class of dark matter particle candidates known as weakly interacting massive particles (WIMPs). WIMPs are particles that were in equilibrium with radiation in the hot, early universe. As the Universe expanded and cooled below the temperature corresponding to the WIMP rest mass, the creation and annihilation of these particles became exceedingly rare. The WIMP number density is "frozen" at the time of decoupling from the CMB and as a result, these particles survive as thermal relics of the Big Bang. The number densities derived from thermal equilibrium and freeze-out, combined with the mass dependence of the annihilation cross section of weakly interacting particles, constrains the WIMP particle mass to $1\ \mathrm{GeV} \lesssim m_{\mathrm{WIMP}} \lesssim 100\ \mathrm{GeV}$, provided that $0.1 \lesssim \Omega_{\mathrm{WIMP}} \lesssim 1$ (Peacock, 1999).[1]

Supersymmetry, or SUSY, is an extension of the standard model of particle physics which predicts a stable particle in this mass range called the neutralino. WIMP detection experiments are typically designed to detect energy deposited by elastic scattering of WIMP particles by nucleons in the detector material. If, like the neutralino, the WIMP is a Majorana particle (a particle that is its own anti-particle) a different detection strategy is possible. In this case pair annihilations can occur, producing high energy gamma-rays that could be detectable by gamma-ray telescopes. Since CDM halos are predicted to be centrally concentrated (see §1.4), neutralino

[1] Assuming $m_{\mathrm{WIMP}} = 100$ GeV and a local dark matter density $\rho_{\mathrm{DM}} = 0.0014\ \mathrm{M}_{\odot}/\mathrm{pc}^3$ obtained from local stellar kinematics measurements, Merrifield () gives a WIMP number density of 10 per 1000 cm^3 (approximately the volume of a cup of coffee).

annihilation would result in an enhanced gamma-ray signal towards the centre of the Galaxy (Berezinsky et al., 1992, 1994). Calcáneo-Roldán and Moore (2000), Taylor and Silk (2003), and Stoehr et al. (2003) recently investigated the consequences of this observational signature for current and future gamma-ray detection experiments.

1.3 Alternative Theories

No discussion of dark matter, especially as pertaining to rotation curves, would be complete without mentioning alternative theories proposed to explain the "missing mass" problem. These proposals usually involve a modification of Newtonian gravity that takes effect at distances comparable to the size of galaxies. Attempts to simply modify the form of the gravitational potential on scales larger than some characteristic scale r_0 (see, e.g., Finzi, 1963; Tohline, 1983; Sanders, 1984) have been shown to be incompatible with with observational constraints, including the observed correlation between luminosity and rotational velocity in disk galaxies known as the Tully-Fisher relation (Milgrom, 1983a), and the variation in the rotation curve flattening radius in galaxies of different sizes (Aguirre et al., 2001).

A more fruitful approach was proposed by Milgrom (1983b) in the form of modified Newtonian dynamics (MOND). Rather than modifying the behaviour of gravity at distances larger than some characteristic scale, Milgrom proposed a modification to Newton's second law that takes effect only at low accelerations. When the acceleration is much larger than some characteristic acceleration, a_0, the relationship between force and acceleration is given by Newton's second law:

$$F = ma, \qquad a \gg a_0 \tag{1.1}$$

i.e. force is proportional to acceleration. For accelerations smaller than a_0, however,

force becomes proportional to the square of the acceleration:

$$F = \frac{ma^2}{a_0}, \qquad a \ll a_0 \tag{1.2}$$

In other words, the force needed to generate a given acceleration is smaller than that predicted by Newtonian dynamics. MOND therefore requires less gravity-producing mass to cause the centripetal accelerations responsible for the velocities observed in the outskirts of galaxies. In contrast, Newtonian dynamics requires the presence of dark matter to account for such high rotation speeds.

Substituting the centripetal acceleration $a = v^2/r$ and the gravitational force external to a spherically symmetric body of mass M into eq. 1.2 gives

$$v^4 = GMa_0. \tag{1.3}$$

MOND therefore predicts asymptotically flat rotation curve which tend to the velocity given by eq. 1.3 at low accelerations/large galactic radii. Assuming a constant mass-to-luminosity ratio, M/L, eq. 1.3 also corresponds to the aforementioned Tully-Fisher relation, given by $L \propto v^4$.

The characteristic acceleration a_0 required to match the zero-point of the Tully-Fisher relation and also to flatten galactic rotation curves at the appropriate radius (which varies for galaxies of different masses and sizes as demanded by observed rotation curves) is about equal to the centripetal acceleration experienced by our solar system toward the centre of the Galaxy, $a_0 \simeq 10^{-10} m/s^2$. Unfortunately, laboratory tests in this acceleration regime are infeasible due to the large background acceleration experienced on Earth or in the near solar system (caused by the Earth's gravity, its rotation, its revolution around the Sun, etc.).

Proponents of MOND cite among its successes the ability to reproduce the shapes of rotation curves and the Tully-Fisher relation, as well as the apparent absence of

missing mass in globular star clusters (Sanders and McGaugh, 2002). Potentially serious problems for MOND which have been raised thus far include the missing mass implied by strong gravitational lensing in the central regions of clusters and the isothermal radial temperature profiles observed in clusters (Aguirre et al., 2001). In a recent comparison of CDM and MOND, Binney (2004) remarks that MOND is not a complete theory in the sense that it has not been incorporated into a theory that obeys the principles of general relativity. As a result, Binney states that, unlike CDM, which is "a natural outgrowth of established physics," "MOND itself could never become a member of the Academy of Established Theories" although "its parent theory most certainly could." Despite this inherent shortcoming, MOND remains a provocative and enduring alternative to dark matter. Even if it is falsified, for instance by the direct detection of dark matter, the correct theory of galaxy formation may yet explain the significance of the characteristic acceleration introduced by MOND, as recently attempted in a CDM framework by Kaplinghat and Turner (2002).

1.4 CDM and "N"

N-body simulations played a crucial role in establishing the viability of CDM cosmological models dating back to the early disk stability studies of Ostriker and Peebles (1973) and the galaxy cluster simulations of White (1976), which helped motivate the classic White and Rees (1978) work. The essence of the N-body method is the use of a finite number of discrete particles to sample the phase space distribution function of a given system of stars or dark matter. The evolution of the system is determined by computing the gravitational forces between these particles and integrating their equations of motion. In such a calculation, particles do not represent individual stars or dark matter particles, but clumps of stars or dark matter which occupy the same volume of phase space. Because N-body particles interact with one another only through gravity, their motion is determined by the mean potential of

the system and they are said to be "collisionless" particles; in contrast, the dynamics of "collisional" gas particles are dominated by short-range interactions.

N-body calculations initially relied on direct summation to calculate the total force on each particle due to every other particle in the system. Unfortunately, this brute force method scales as $\mathcal{O}(N^2)$ and is therefore inefficient for large numbers of particles ($N \gg 10^4$). The development of more sophisticated numerical methods has enabled N-body simulators to surpass such limitations. A first class of algorithms is based on the availability of $\mathcal{O}(N \log N)$ Fast Fourier Transform (FFT) techniques, and includes the particle-mesh (PM) method and variations thereof. In this approach, the FFT is used to solve for the gravitational potential of a distribution of particles interpolated onto a regular mesh. This method is ideal for homogeneous, periodic N-body simulations.

The N-body simulations presented in this thesis were performed with tree codes. Tree codes represent a second class of algorithms which improve scaling by recognizing that the precise distribution of particles becomes less important with increasing distance. Particles are organized in a hierarchical tree structure and multipole expansions are used to approximate the gravitational force due to distant particles. This method is also $\mathcal{O}(N \log N)$ and is well-suited for inhomogeneous or heavily clustered simulations. The development of N-body codes based on these approaches, in conjunction with improvements in computer technology and the advent of massively parallel supercomputers, have made it possible to perform cosmological N-body simulations with many millions of particles.

1.5 The Structure of CDM Halos

Over the past two decades, N-body simulations of increasingly high resolution have been used to study the internal structure of dark matter halos. Analytic calculations (Gunn and Gott, 1972; Fillmore and Goldreich, 1984; Hoffman and Shaham,

1985; White and Zaritsky, 1992) and early simulation results (Frenk et al., 1985, 1988; Quinn et al., 1986; Dubinski and Carlberg, 1991; Crone et al., 1994) at first suggested that the density profile of halos in cold dark matter (CDM) cosmological models obeyed a simple power law in radius, similar to the structure of an isothermal sphere, $\rho \propto r^{-2}$. Higher resolution simulations, however, indicated a more complicated radial dependence. In particular, Navarro et al. (1996b, 1997, hereafter NFW) found that simulated dark halos over a wide range of size and mass scales are well fit by a "universal" density profile with a gently changing logarithmic slope

$$\rho_{\rm NFW}(r) \propto \frac{1}{(r/r_s)(1+r/r_s)^2}, \tag{1.4}$$

where r_s is a characteristic scale radius for the halo: it is shallower than isothermal inside r_s, and steeper than isothermal for $r > r_s$. Although both the universality of the NFW profile as well as the innermost value of the logarithmic slope have been debated extensively in the literature (Fukushige and Makino, 1997; Moore et al., 1998; Kravtsov et al., 1998; Moore et al., 1999a; Ghigna et al., 2000; Klypin et al., 2001; Fukushige and Makino, 2001), there is general consensus that the density profile of CDM halos diverges near the centre. Consequently, numerous authors have argued that "cuspy" density profiles like NFW are inconsistent with the constant density "cores" suggested by the shape of some disk galaxy rotation curves (Flores and Primack, 1994; Moore, 1994; de Blok et al., 2001b).

Unfortunately, the constraints provided by rotation curve data are strongest just where numerical simulations are least reliable. Resolving CDM halos down to the kpc-scales probed by the innermost points of rotation curves represents a significant computational challenge which requires extremely high mass and force resolution, as well as careful integration of N-body particle orbits in the central, high density regions of halos, a feat that only recently has been accomplished (Moore et al., 1999a; Power et al., 2003).

1.6 Outline

The work presented in this thesis builds on the body of work described in the previous section by using the highest resolution N-body simulations currently feasible to investigate the inner structure of CDM halos. In the first half of Chapter 2 we use a suite of simulated galaxy-sized halos to verify the numerical convergence criteria presented in Power et al. (2003) and to establish the minimum reliably resolved radius in these halos. We examine the density profile of simulated halos with particular attention to the inner logarithmic slope.

In the latter part of this chapter, we focus on a direct comparison of the structure of simulated halos with the mass distribution in Low Surface Brightness (LSB) galaxies inferred from rotation curve data. LSBs are a type of extremely diffuse disk galaxy that went undiscovered by astronomers until the 1980s due to their very low contrast with the night sky background. Since the baryonic mass fraction of these galaxies is very low ($\lesssim 5\%$, Bothun et al., 1997), the rotation curves of LSB disks are expected to trace rather cleanly the potential of the underlying dark matter halo. To first order, it is therefore justified to compare halo profiles with LSB rotation curves without including complicated mass modelling of the baryonic component of the galaxy.

In Chapter 3 we investigate the universality of CDM halo structure over a wide range of halo mass, from dwarf galaxies to rich galaxy clusters. We investigate deviations between the density profiles of simulated halos and fitting formulae like the one proposed by NFW and present an improved formula which more accurately reproduces the radial dependence of halo density profiles.

Most rotation curve analyses, including the analysis presented in Chapter 2 relies on the assumption that the rotation curve of an observed galaxy is directly proportional to the spherically-averaged circular velocity profile of its host halo. CDM halos are known to be triaxial, however, which may lead disks to deviate significantly from

simple circular motion. In Chapter 4 we explore the effects of a triaxial halo potential on the kinematics and expected rotation curve of a disk galaxy. In particular, we discuss whether deviations from circular motion can "mask" the presence of cuspy halos.

Chapter 3 has already been published in the Monthly Notices of the Royal Astronomical Society (Mon. Not. R. Astron. Soc.) as Navarro et al. (2004). Chapter 2 has been submitted to Mon. Not. R. Astron. Soc. and a previous draft version is available as a preprint (Hayashi et al., 2003). Chapter 4 has also been submitted as a *Letter* to the Astrophysical Journal. Some figures which appear in this thesis are not present in the published or submitted versions and are marked by * in the List of Figures.

Chapter 2

Halo Mass Profiles and LSB Rotation Curves

Abstract

We use a set of high-resolution cosmological N-body simulations to investigate the inner mass profile of galaxy-sized cold dark matter (CDM) halos. These simulations extend the numerical convergence study presented in Power et al. (2003), and demonstrate that the mass profile of CDM galaxy halos can be robustly estimated beyond a minimum converged radius of order $r_{\rm conv} \sim 1\ h^{-1}$kpc in our highest resolution runs. The density profiles of simulated halos become progressively shallower from the virial radius inwards, and show no sign of approaching a well-defined power-law near the centre. At $r_{\rm conv}$, the density profile is steeper than expected from the formula proposed by Navarro, Frenk, and White (1996), which has a $\rho \propto r^{-1}$ cusp, but significantly shallower than the steeply divergent $\rho \propto r^{-1.5}$ cusp proposed by Moore et al. (1999a). We perform a direct comparison of the spherically-averaged dark matter circular velocity profiles with Hα rotation curves of low surface brightness (LSB) galaxies from the samples of McGaugh et al. (2001), de Blok and Bosma (2002), and Swaters et al. (2003a). We find that most galaxies in this sample (about 70%) are consistent with the structure of CDM halos. Of the remainder, 20% have irregular rotation curves that cannot be fit by any simple fitting function with few free parameters, and 10% are inconsistent with CDM halos. However, the latter consist mostly of rotation curves that do not extend to large enough radii to accurately determine their shapes and maximum velocities. We conclude that the inner structure of CDM halos is not manifestly inconsistent with the rotation curves of LSB galaxies.

2.1 Introduction

The structure of dark matter halos and its relation to the cosmological context of their formation has been studied extensively over the past few decades. Early analytic calculations focused on the scale free nature of the gravitational accretion process and suggested that halo density profiles might be simple power laws (Gunn and Gott, 1972; Fillmore and Goldreich, 1984; Hoffman and Shaham, 1985; White and Zaritsky, 1992). Cosmological N-body simulations, however, failed to confirm these analytic expectations. Although power-laws with slopes close to those motivated by the theory were able to describe some parts of the halo density profiles, even early simulations found significant deviations from a single power-law in most cases (Frenk et al., 1985, 1988; Quinn et al., 1986; Dubinski and Carlberg, 1991; Crone et al., 1994). More systematic simulation work concluded that power-law fits were inappropriate, and that, properly scaled, dark halos spanning a wide range in mass and size are well fit by a "universal" density profile (Navarro et al., 1995, 1996b, 1997, hereafter NFW):

$$\rho_{\rm NFW}(r) = \frac{\rho_s}{(r/r_s)(1+r/r_s)^2}. \tag{2.1}$$

One characteristic feature of this fitting formula is that the logarithmic slope, $\beta(r) = -d\log\rho/d\log r = (1+3\ r/r_s)/(1+r/r_s)$, increases monotonically from the centre outwards. The density profile steepens with increasing radius; it is shallower than isothermal inside the characteristic scale radius r_s, and steeper than isothermal for $r > r_s$. Another important feature illustrated by this fitting formula is that the profiles are "cuspy" ($\beta_0 = \beta(r=0) > 0$): the dark matter density (but not the potential) diverges at small radii.

Subsequent work has generally confirmed these trends, but has also highlighted potentially important deviations from the NFW fitting formula. In particular, Fukushige and Makino (1997, 2001) and Moore and collaborators (Moore et al., 1998, 1999a; Ghigna et al., 2000) have reported that NFW fits to their simulated halos (which had

much higher mass and spatial resolution than the original NFW work) underestimate the dark matter density in the innermost regions ($r < r_s$). These authors proposed that the disagreement was indicative of inner density "cusps" steeper than the NFW profile and advocated a simple modification to the NFW formula with $\beta_0 = 1.5$ (rather than 1.0).

The actual value of the asymptotic slope, β_0, is still being hotly debated in the literature (Jing et al., 1995; Klypin et al., 2001; Taylor and Navarro, 2001; Navarro, 2003; Power et al., 2003; Fukushige et al., 2003), but there is general consensus that CDM halos are indeed cuspy. This has been recognized as an important result, since the rotation curves of many disk galaxies, and in particular of low surface brightness (LSB) systems, appear to indicate the presence of an extended region of constant dark matter density: a dark matter "core" (Flores and Primack, 1994; Moore, 1994; Burkert, 1995; Blais-Ouellette et al., 2001; de Blok et al., 2001a,b).

Unfortunately, rotation curve constraints are strongest just where numerical simulations are least reliable. Resolving CDM halos down to the kpc scales probed by the innermost points of observed rotation curves requires extremely high mass and force resolution, as well as careful integration of particle orbits in the central, high density regions of halos. This poses a significant computational challenge that has been met in very few of the simulations published to date.

This difficulty has meant that rotation curves have usually been compared with extrapolations of the simulation data into regions that may be severely compromised by numerical artifact. Such extrapolations rely heavily on the (untested) applicability of the fitting formula used. This practice does not allow either for halo-to-halo variations, temporary departures from equilibrium or deviations from axisymmetry to be taken into account when modelling the observational data.

Finally, the theoretical debate on the asymptotic central slope of the dark matter density profile, β_0, has led at times to unwarranted emphasis on the innermost regions of rotation curves, rather than on an appraisal of the data over its full radial extent.

For example, de Blok et al. (2001a,b) derive constraints on β_0 from the innermost few points of their rotation curves, and conclude that $\beta_0 \sim 0$ for most galaxies in their sample. However, this analysis focuses on the regions most severely affected by non-circular motions, seeing, misalignments and slit offsets. Such effects limit the accuracy of circular velocity estimates based on long-slit spectra. It is perhaps not surprising, then, that other studies have disputed the conclusiveness of these findings. For example, an independent analysis of data of similar quality by Swaters et al. (2003a) (see also van den Bosch et al., 2000) conclude that the data is consistent with both cuspy ($\beta_0 \simeq 1$) and cored ($\beta_0 \simeq 0$) dark matter halos. This issue is further complicated by recent simulation data (Power et al., 2003, hereafter P03) which show scant evidence for a well-defined value of β_0 in CDM halos. Given these difficulties, focusing the theoretical or observational analysis on β_0 does not seem promising.

In this paper, we improve upon previous work by comparing circular velocity curves from simulations directly with the full measured rotation curves of LSB galaxies. We present results from a set of seven galaxy-sized dark matter halos, each of which has been simulated at various resolution levels in order to ascertain the numerical convergence of our results. This allows us to test rigorously the P03 convergence criteria, as well as to clarify the cusp-core discrepancy through direct comparison between observation and simulation. Chapter 3 addresses the issue of universality of CDM halo structure using simulations that span a wide range of scales, from dwarf galaxies to galaxy clusters.

The outline of this paper is as follows. In §2.2 we introduce our set of simulations and summarize briefly our numerical methods. The seven galaxy-sized halos that form the core of our sample have been simulated at various resolutions, and we use them in §2.3 to investigate the robustness of the P03 numerical convergence criteria. The density profiles of these halos are presented and compared with previous work in §2.4. In §2.5 we compare the halo V_c profiles with the LSB rotation curve datasets of McGaugh et al. (2001), de Blok and Bosma (2002), and Swaters et al. (2003a). Our

main conclusions and plans for future work are summarized in §2.6.

2.2 The Numerical Simulations

We have focused our analysis on seven galaxy-sized dark matter halos selected at random from two different cosmological N-body simulations of periodic boxes with comoving size $L_{\rm box} = 32.5\,h^{-1}$Mpc and $35.325\,h^{-1}$Mpc, respectively. Each of these "parent" simulations has $N_{\rm box} = 128^3$ particles, and adopts the currently favoured "concordance" ΛCDM model, with $\Omega_0 = 0.3$, $\Omega_\Lambda = 0.7$, and either $h = 0.65$ (runs labelled G1, G2 and G3) or $h = 0.7$ (G4, G5, G6, and G7, see Table 2.1). The power spectrum in both simulations is normalized so that the linear rms amplitude of fluctuations on spheres of radius $8\,h^{-1}$Mpc is $\sigma_8 = 0.9$ at $z = 0$.

All halos (G1 to G7) have been re-simulated at three or four different mass resolution levels; each level increases the number of particles in the halo by a factor of 8, so that the mass per particle has been varied by a factor 512 in runs G1-G3, and by a factor 64 in runs G4-G7 (see Table 2.1). All of these runs focus numerical resources on the Lagrangian region from where each system draws its mass, whilst approximating the tidal field of the whole box by combining distant particles into groups of particles whose mass increases with distance from the halo. This resimulation technique follows closely that described in detail in P03 and in Chapter 3, where the reader can find full details. For completeness, we present here a brief account of the procedure.

Halos selected for resimulation are identified at $z = 0$ from the full list of halos with circular velocities in the range (150, 250) km s^{-1} in the parent simulations. All particles within a sphere of radius 3 r_{200}[†] centred on each halo are then traced back to the initial redshift configuration ($z_i = 49$). The region defined by these

[†]We define the "virial radius," r_{200}, as the radius of a sphere of mean density 200 times the critical value for closure, $\rho_{\rm crit} = 3\,H^2/8\pi G$, where H is Hubble's constant. We parameterize the present value of Hubble's constant H by $H_0 = 100\,h$ km s^{-1} kpc^{-1}

particles is typically fully contained within a box of size $L_{\rm sbox} \simeq 5\,h^{-1}$Mpc, which is loaded with $N_{\rm sbox} = 32^3$, 64^3, 128^3, or 256^3 particles. Particles in this new high-resolution region are perturbed with the same waves as in the parent simulation as well as with additional smaller scale waves up to the Nyquist frequency of the high resolution particle grid. Particles which do not end up within 3 r_{200} of the selected halo at $z = 0$ are replaced by lower resolution particles which replicate the tidal field acting on the high resolution particles. This resampling includes some particles within the boundaries of the high resolution box, and therefore the high resolution region defines an asymmetrical "amoeba-shaped" three-dimensional volume surrounded by tidal particles whose mass increases with distance from this region.

A summary of the numerical parameters and halo properties is given in Table 2.1. This table also includes reference to 12 further runs, four of them corresponding to dwarf galaxy-sized halos and eight of them to galaxy cluster-sized halos. These systems have been simulated only at the highest resolution ($N_{\rm sbox} = 256^3$), and therefore are not included in our convergence analysis. These runs are discussed in detail in Chapter 3.

Some simulations were performed with a fixed number of timesteps for all particles using Stadel and Quinn's parallel N-body code `PKDGRAV` (Stadel, 2001), while others used the N-body code `GADGET` (Springel et al., 2001). The `GADGET` runs allowed for individual timesteps for each particle assigned using either the `RhoSgAcc` or `EpsAcc` criterion (see P03 for full details). The halo labelled G1 in this paper is the same one selected for the numerical convergence study presented in P03. Although `PKDGRAV` also has individual timestepping capabilities, we have chosen not to take advantage of these for the simulations presented in this paper. We note that P03 finds only a modest computational gain due to multi-stepping schemes provided that the softening parameter is properly chosen.

The softening parameter (fixed in comoving coordinates) for each simulation (with the exception of G1/256^3, see P03) was chosen to match the "optimal" softening

suggested by P03:

$$\epsilon_{\rm opt} = \frac{4\, r_{200}}{N_{200}^{1/2}}, \tag{2.2}$$

where N_{200} is the number of particles within r_{200} at $z = 0$. This softening choice minimizes the number of timesteps required for convergent results by minimizing discreteness effects in the force calculations whilst ensuring adequate force resolution.

At $z = 0$, the mass within the virial radius, M_{200}, of our galaxy-sized halos ranges from $\sim 10^{12}\ h^{-1}M_{\odot}$ to $\sim 3\times10^{12}\ h^{-1}M_{\odot}$, corresponding to circular velocities, $V_{200} = (GM_{200}/r_{200})^{1/2}$, in the range 160 km s^{-1} to 230 km s^{-1}. Figure 2.1 shows M_{200} as a function of redshift for the $N_{\rm sbox} = 256^3$ simulations of all seven halos. Differences in the evolution of the halo mass with redshift reflect the different accretion histories of the halos. More massive halos ($M_{200} > 10^{12}\ h^{-1}M_{\odot}$) experience a major merger at $z \lesssim 1.3$ which increases the mass of halo by a factor of three. In the four less massive halos (G4-G7) this merger occurs earlier, at $z \gtrsim 1.3$, and increases M_{200} by about a factor of two. Halo mass accretion histories are reasonably well-described by the fitting formula proposed by Wechsler et al. (2002):

$$M_{200}(z) = M_0 e^{-\alpha_c z}, \tag{2.3}$$

where $M_0 \equiv M_{200}(z = 0)$, and α_c is a free parameter related to the characteristic formation epoch of the halo.

2.3 Numerical Convergence

2.3.1 Criteria

P03 propose three different conditions that should be satisfied in order to ensure convergence in the circular velocity profile. According to these criteria, convergence to better than 10% in the spherically-averaged circular velocity, $V_c(r)$, is achieved at

radii which satisfy the following conditions:

1. The local circular orbit period $t_{\rm circ}(r)$ is much greater than the size of the timestep Δt:

$$\frac{t_{\rm circ}(r)}{t_{\rm circ}(r_{200})} \gtrsim 15 \left(\frac{\Delta t}{t_0}\right)^{5/6} \tag{2.4}$$

   where t_0 denotes the age of the universe, which is by definition of the order of the circular orbit timescale at the virial radius, $t_{\rm circ}(r_{200})$.

2. Accelerations do not exceed a characteristic acceleration, a_ϵ, determined by V_{200} and the softening length ϵ:

$$a(r) = \frac{V_c^2(r)}{r} \lesssim a_\epsilon = 0.5\,\frac{V_{200}^2}{\epsilon} \tag{2.5}$$

   where $a(r)$ is the mean radial acceleration experienced by particles at a distance r from the centre of the system, $a(r) = GM(r)/r^2 = V_c^2(r)/r$.

3. Enough particles are enclosed such that the local collisional relaxation timescale $t_{\rm relax}(r)$ is longer than the age of the universe[1]:

$$\frac{t_{\rm relax}(r)}{t_{\rm circ}(r_{200})} = \frac{\sqrt{200}}{8}\frac{N(r)}{\ln N(r)}\left(\frac{\overline{\rho}(r)}{\rho_{\rm crit}}\right)^{-1/2} \gtrsim 1 \tag{2.6}$$

   where $N(r)$ is the number of particles and $\overline{\rho}(r)$ is the mean density within radius r.

For "optimal" choices of the softening and timestep, as well as for the typical number of particles in our runs, we find that criterion iii above is the strictest one. The number of high resolution particles thus effectively defines the "predicted" converged radius, $r_{\rm conv}$, beyond which, according to P03, circular velocities should be accurate to

[1] We adopt a slightly more conservative criterion than P03, who require $t_{\rm relax} \gtrsim 0.6\ t_{\rm circ}(r_{200})$.

better than 10%. We emphasize that this accuracy criterion applies to the cumulative mass profile; convergence in properties such as local density estimates, $\rho(r)$, typically extends to radii significantly smaller than $r_{\rm conv}$.

2.3.2 Validating the Convergence Criteria

We assess the validity of the convergence criteria listed above by comparing the mass profile of the highest resolution run corresponding to each halo with those obtained at lower resolution. Figure 2.2 illustrates the procedure. From top to bottom, the three panels in this figure show, as a function of radius, the circular orbit timescale, the mean radial acceleration, and the relaxation timescale, respectively, for the four runs corresponding to halo G3. The small arrows at the bottom of each panel indicate the choice of gravitational softening for each run. The dotted curves in the top and middle panels show the best fit NFW profile to the converged region of the highest resolution $N_{\rm sbox} = 256^3$ run.

The "converged radius" corresponding to each criterion is determined by the intersection of the horizontal dashed lines in each panel with the "true" profile, which we shall take to be that of the highest resolution run (shown in solid black in Figure 2.2). Clearly, the strictest criterion is that imposed by the relaxation timescale (the dotted vertical lines in the lower panel show the converged radius corresponding to this criterion). This suggests, for example, that the lowest-resolution G3 run (with $N_{\rm sbox} = 32^3$, shown in solid blue), should start to deviate from the converged profiles roughly at $r \sim 0.1\ r_{200}$. Indeed, this appears to be the radius at which this profile starts to "peel off" from the highest resolution one, as shown in the top two panels of Figure 2.2. Increasing the number of high resolution particles by a factor of eight typically brings the converged radius inwards by a factor of ~ 2.4. For the medium-resolution run ($N_{\rm sbox} = 64^3$, shown in solid green), $r_{\rm conv}$ is predicted to be $\sim 0.04\ r_{200}$, which, again, coincides well with the radius inside which departures from

the converged profile are apparent. Similarly, $r_{\rm conv} \sim 0.017\, r_{200}$ for the high-resolution ($N_{\rm sbox} = 128^3$) run (shown in red).

The density and circular velocity profiles corresponding to the four G3 runs are shown in Figure 2.3. Panels on the left show the profiles down to the radius that contains 50 particles, whereas those on the right show the profiles restricted to $r \gtrsim r_{\rm conv}$. Figure 2.3 illustrates two important results alluded to above: (i) both $\rho(r)$ and $V_c(r)$ converge well at $r \gtrsim r_{\rm conv}$, and (ii) convergence in $\rho(r)$ extends to radii smaller than $r_{\rm conv}$. Indeed, the top-left panel shows that our choice of $r_{\rm conv}$ is rather conservative when applied to the density profile. Typically, densities are estimated to better than 10% down to $r \sim 0.6\, r_{\rm conv}$.

How general are these results? Figure 2.4 compares the minimum "converged" radius predicted by the P03 criteria, $r_{\rm conv}$, with $r_{10\%vc}$, the *actual* radius where circular velocities in the lower resolution runs deviate from the highest resolution run by more than 10%. In essentially all cases, $r_{\rm conv} \lesssim r_{10\%vc}$, indicating that the P03 criteria are appropriate, albeit at times somewhat conservative. We list our $r_{\rm conv}$ estimates for all runs in Table 2.1.

We note that Stoehr et al. (2003) find similar results for their Milky Way-sized galaxy halo resimulated at four different levels of resolution. For example, they find the V_c profiles for versions of their halo with $N_{200} = 1.4 \times 10^4$ and 1.3×10^5 converge to within 5% of the high resolution profile at about 6.3, and 3.5 h^{-1}kpc, respectively. For our halo G1, we find $r_{10\%vc} = 5.1\ h^{-1}$kpc and 1.3 h^{-1}kpc for simulations with $N_{200} = 4.8 \times 10^4$ and 3.8×10^5, respectively.

2.4 Halo Structure and Fitting Formulae

The dotted curves in Figure 2.3 show the best NFW fits to the density and circular velocity profile of the highest resolution run. The dashed lines correspond to the best fit adopting the modification to the NFW profile advocated by Moore et al.

(1999a),

$$\rho_{\rm Moore}(r) = \frac{\rho_M}{(r/r_M)^{1.5}(1+(r/r_M)^{1.5})}. \quad (2.7)$$

These fits are obtained by straightforward χ^2 minimization in two parameters, r_s or r_M, and the characteristic density ρ_s or ρ_M. The profiles are calculated in bins of equal width in $\log r$, and the fits are performed over the radial range $r_{\rm conv} < r < r_{200}$. Equal weights are assigned to each radial bins because the statistical (Poisson) uncertainty in the determination of the mass within each bin is negligible (each bin contains thousands of particles) so uncertainties are completely dominated by systematic errors whose radial dependence is difficult to assess quantitatively.

The best fits to $\rho(r)$ and $V_c(r)$ shown in Figure 2.3 are obtained independently from each other. Values of the concentration parameter, $c_{\rm NFW} = r_{200}/r_s$, for the best fit NFW profiles are 6.4 and 5.3 for fits to the density and circular velocity profile, respectively; the Moore et al concentrations, $c_{\rm Moore} = r_{200}/r_M$, are 3.0 and 2.9 for the best fits to $\rho(r)$ and $V_c(r)$, respectively. Over the converged region, $r \gtrsim r_{\rm conv}$, both the NFW and Moore et al profiles appear to reproduce reasonably well the numerical simulation results. Indeed, no profile in the G3 runs deviates by more than 10% in V_c or 30% in $\rho(r)$ from the best fits obtained with either eq. 2.1 or eq. 2.7. More substantial differences are expected only well inside $r_{\rm conv}$, but these regions are not reliably probed by the simulations. This suggests that either the NFW or Moore et al profile may be used to describe the structure of ΛCDM halos outside $\sim 1\%$ of the virial radius, but also implies that one should be extremely wary of extrapolations inside this radius.

2.4.1 The Radial Dependence of the Logarithmic Slope

One intriguing feature of Figure 2.3 is that the Moore et al formula appears to fit the G3 density profiles as well or better than NFW but that V_c profiles are somewhat better approximated by NFW (see also P03). This suggests that neither formula

captures fully and accurately the radial dependence of the structure of ΛCDM halos.

This view is confirmed by the radial dependence of the logarithmic slope of the density profile $\beta(r) = -d\log\rho/d\log r$, which is shown in the top-left panel of Figure 2.5 for all the high-resolution runs, and compared with the predictions of the NFW (solid line) and Moore et al (dashed line) formulae. Logarithmic slopes are calculated by numerical differentiation of the density profile, computed in radial bins of equal logarithmic width ($\Delta \log r/r_{200} \simeq 0.2$). The slope profiles in Figure 2.5 are normalized to r_{-2}, the radius where $\beta(r)$ takes the "isothermal" value of 2.[2] In this and all subsequent figures, profiles are shown only down to the minimum converged radius $r_{\rm conv}$. This corresponds typically to a radius $r_{\rm conv} \simeq 0.006\ r_{200}$, or about 1-2 h^{-1}kpc for halos simulated at highest resolution (see Table 2.1).

The top left panel of Figure 2.5 shows that halos differ from the NFW and Moore et al formula in a number of ways:

- there is no obvious convergence to an asymptotic value of the logarithmic slope at the centre; the profile gets shallower all the way down to the innermost radius reliably resolved in our runs, $r_{\rm conv}$.

- the slope at $r_{\rm conv}$ is significantly shallower than the asymptotic value of $\beta_0 = 1.5$ advocated by Moore et al. (1999a). The shallowest value measured at $r_{\rm conv}$ is $\beta \simeq 1$, and the average over all seven halos is $\beta \simeq 1.2$.

- Most halo profiles become shallower with radius more gradually than predicted by the NFW formula; at $r \sim 0.1\ r_{-2}$ the average slope is ~ -1.4, whereas NFW would predict ~ -1.18. The NFW density profile turns over too sharply from $\rho \propto r^{-3}$ to $\rho \propto r^{-1}$ compared to the simulations.

In other words, the Moore et al profile appears to fit better the inner regions of the density profile of some ΛCDM halos (see bottom-left panel of Figure 2.5) *not*

[2] r_{-2} is in this sense equivalent to the scale radius r_s of the NFW profile.

because the inner density cusp diverges as steeply as $\beta_0 = 1.5$, but rather because its logarithmic slope becomes shallower inwards less rapidly than NFW.

It is important to note as well that there is significant scatter from halo to halo, and that two of the seven density profiles are actually fit better by the NFW formula. Are these global deviations from a "universal" profile due to substructure? We have addressed this question by removing substructure from all halos and then recomputing the slopes. Substructure is removed by first computing the local density at the position of each particle, ρ_i, using a spline kernel similar to that used in Smoothed Particle Hydrodynamics (SPH) calculations.[3] Then, we remove all particles whose densities are more than two standard deviations above the spherically-averaged mean density at its location. (The mean and standard deviation are computed in bins of equal logarithmic width, $\Delta \log r/r_{200} \simeq 0.01$). The procedure is iterated until no further particles are removed. The remaining particles form a smoothly distributed system that appears devoid of substructure on all scales, as shown in Figure 2.6 for Halo1/256^3. Figure 2.7 shows the density profiles of all seven galaxy-sized halos plotted as $r^2\rho(r)$ and normalized to r_{-2}. The density profiles are shown before and after the removal of substructure. We find that density profiles are smoother after the removal of substructure but that most of the variation in the overall shapes of the profiles remains. We conclude that the presence of substructure is not directly responsible for the observed scatter in the shape of halo density profiles.

2.4.2 Comparison with Other Work

Are these conclusions consistent with previous work? To explore this issue, we have computed the logarithmic slope profile of three CDM halos run by Moore and collaborators. The halos we have re-analyzed are the Milky Way- and M31-like galaxy halos of the Local Group system from Moore et al. (1999a) and the LORES version of

[3]See `http://www-hpcc.astro.washington.edu/tools/smooth.html`

the "Virgo" cluster halo from Ghigna et al. (2000). The $z \simeq 0.1$ output of the Local Group simulation was provided to us by the authors, whereas the Virgo cluster was re-run using initial conditions available from Moore's website.[4] The Virgo cluster run used the same N-body code as the original simulation (**PKDGRAV**) but was run with a fixed number of timesteps (12800). A run with 6400 timesteps was also carried out and no differences in the mass profiles were detected. The number of particles within the virial radius is 1.2×10^6, 1.7×10^6, and 5.0×10^5, for the Milky Way (MW), M31 and LORES Virgo cluster halos, respectively.

Figure 2.5 shows the logarithmic slope (upper right panel) and density (lower right panel) profiles corresponding to these halos, plotted down to the minimum converged radius $r_{\rm conv}$. No major differences between these simulations and ours are obvious from these panels. It is clear, for example, that at the innermost converged point, the slope of the density profile of the two Local Group halos is significantly shallower than $r^{-1.5}$, and shows no signs of having converged to a well-defined power-law behaviour. There is some evidence for "convergence" to a steep cusp ($r^{-1.4}$) in the LORES Virgo cluster simulation but the dynamic range over which this behaviour is observed is rather limited. The Virgo cluster run thus appears slightly unusual when compared with other systems in our ensemble. Although our reanalysis confirms the conclusion of Moore et al. (1998, 1999a) that this particular system appears to have a steeply divergent core, this does not seem to be a general feature of ΛCDM halos.

We also note that the highest resolution simulation of a galaxy halo is currently the $N_{200} = 1.0 \times 10^7$ Milky Way-sized halo of Stoehr et al. (2003). These authors estimate that the V_c profile of this halo is resolved to within 5% of the converged solution down to 0.004 r_{200} or about 0.7 h^{-1}kpc and conclude that the inner slope of the density profile of this halo is significantly shallower than $r^{-1.5}$ at radii greater than this minimum converged radius.

[4] `http://www.nbody.net` We note that all of these runs were evolved in an Standard CDM (SCDM) $\Omega_0 = 1$ cosmogony, rather than the ΛCDM scenario we adopt in this paper.

Our results thus lend support to the conclusions of Klypin et al. (2001), who argue that there is substantial scatter in the inner profiles of cold dark matter halos. Some are best described by the NFW profile whereas others are better fit by the Moore et al formula, implying that studies based on a single halo might reach significantly biased conclusions.

Finally, we note that deviations from either fitting formula in the radial range resolved by the simulations, although significant, are small. Best NFW/Moore et al fits are typically accurate to better than $\sim$ 20% in circular velocity and $\sim$ 40% in density, respectively. We discuss in Chapter 3 the constraints placed by our simulations on extrapolations of these formulae to the inner regions as well as on the true asymptotic inner slope of ΛCDM halo density profiles.

2.5 Halo Circular Velocity Profiles and LSB Rotation Curves

As discussed in § 2.1, an important discrepancy between the structure of CDM halos and the mass distribution in disk galaxies inferred from rotation curves has been noted repeatedly in the literature over the past decade (Moore, 1994; Flores and Primack, 1994; Burkert, 1995; McGaugh and de Blok, 1998; Moore et al., 1999a; van den Bosch et al., 2000; Côté et al., 2000; Blais-Ouellette et al., 2001; van den Bosch and Swaters, 2001; Jimenez et al., 2003). In particular, the shape of the rotation curves of low surface brightness (LSB) galaxies has been identified as especially difficult to reconcile with the cuspy density profiles of CDM halos.

Given the small contribution of the baryonic component to the mass budget in these galaxies, the rotation curves of LSB disks are expected to trace rather cleanly the dark matter potential, making them ideal probes of the inner structure of dark matter halos in LSBs. Many of these galaxies are better fit by circular velocity curves

arising from density profiles with a well-defined constant density "core" rather than the cuspy ones inferred from simulations, a result that has prompted calls for a radical revision of the CDM paradigm on small scales (see e.g., Spergel and Steinhardt, 2000).

It is important, however, to note a number of caveats that apply to the LSB rotation curve problem.

- Many of the early rotation curves where the disagreement was noted were unduly affected by beam smearing in the HI data (Swaters et al., 2000). For example, van den Bosch et al. (2000) argue that, once beam smearing is taken into account, essentially all HI LSB rotation curves are consistent with cuspy halo profiles. The observational situation has now improved substantially thanks to higher-resolution rotation curves obtained from long-slit Hα observations (see, e.g., McGaugh et al., 2001; de Blok et al., 2001a; Swaters et al., 2000, 2003a). We shall restrict our analysis to these rotation curves in what follows.

- Strictly speaking, the observational disagreement is with the fitting formulae, rather than with the actual structure of simulated CDM halos. As noted in the previous section, there are systematic differences between them, so it is important to confirm that the disagreement persists when LSB rotation curves are contrasted directly with simulations.

- Finally, it must be emphasized that the rotation curve problem arises when comparing rotation speeds of gaseous disks to the spherically-averaged circular velocity profiles of dark matter halos. Given that CDM halos are expected to be significantly non-spherical (Davis et al., 1985; Barnes and Efstathiou, 1987; Warren et al., 1992; Jing et al., 1995; Thomas et al., 1998; Jing and Suto, 2002), some differences between the two are to be expected. It is therefore important to use the full 3D structure of CDM halos to make predictions regarding the rotation curves of gaseous disks that may be compared directly to observation. We shall neglect this complex issue in this paper, but plan to explore in detail

the rotation curves of gaseous disks embedded in such asymmetric potentials in future papers of this series.

In what follows, we compare directly the circular velocity profiles of our simulated halos with the observational data. This procedure has the advantage of retaining the diversity in the shapes of halo profiles that is often lost when adopting simple analytic fitting formulae. In addition, we consider circular velocity profiles only down to the innermost converged radius, thereby eliminating uncertainties about the reliability of the profile at very small radii.

We begin the analysis by emphasizing the importance of taking into account the changes in the central halo mass profile induced by accretion events. Indeed, these may trigger and sustain departures from the "average" profile that may be detectable in the rotation curves of embedded gaseous disks. We shall then describe a simple characterization of rotation curve shapes that may be applied to both observational and simulation data. This enables a direct and quantitative assessment of the "cusp" versus "core" problem as it applies to the most recent LSB datasets.

2.5.1 Evolution of the Inner Mass Profile

Systematic—and at times substantial—changes in the inner circular velocity profile are induced by accretion events during the assembly of the halo, even when such events might contribute only a small fraction of mass to the inner regions. These transients may increase substantially the scatter in the shape of the V_c profiles and they ought to be taken into account when comparing with observation.

This is illustrated in Figure 2.8, which shows the evolution of the mass and circular velocity profiles of halo G1. The top panel of this figure shows the evolution of the mass enclosed within 2, 10, 20 kpc (physical), and r_{200}, as a function of redshift. Although the mass inside 20 h^{-1}kpc increases by less than $\sim 25\%$ since $z = 1$, there are significant ($\sim 50 - 60\%$) fluctuations during this time caused by the tidal effects

of orbiting substructure and accretion events. Most noticeable is a major merger at $z \simeq 0.7$, which affects the mass profile down to the innermost reliably resolved radius, $\simeq 2\ h^{-1}$kpc.

The effect of these fluctuations on the circular velocity profile is shown in the bottom panel of Figure 2.8. Here we show the inner 20 h^{-1}kpc of the circular velocity profile before ($z = 1.1$), during ($z = 0.48$), and after ($z = 0$) a major accretion event. Substantial changes in the shape of the V_c profile are evident as the halo responds to the infalling substructure. Note that the changes persist over timescales of order $\gtrsim 1$ Gyr, exceeding the circular orbital period at $r = 2$, 10, and 20 kpc (~ 0.13, 0.34, and 0.58 Gyr, respectively). These relatively long lasting changes thus would likely be reflected in the dynamics of a disk present at the centre of the halo.

2.5.2 LSB Rotation Curve Shapes

Could the evolutionary effects discussed above be responsible, at least in part, for the constant density cores inferred from the rotation curves of LSB and dwarf galaxies? Since it is nearly impossible to tailor a simulation to reproduce individual galaxies in detail, it is important to adopt a simple characterization of the rotation curves that allows for a statistical assessment of the disagreement between halo V_c profiles and observation. We have thus adopted a three-parameter fitting formula commonly used in observational work to describe optical rotation curves (Courteau, 1997):

$$V(r) = \frac{V_0}{(1 + x^\gamma)^{1/\gamma}}. \tag{2.8}$$

Here V_0 is the asymptotic velocity, $x = r_t/r$, where r_t is a scale radius, and the dimensionless parameter γ describes the overall shape of the curve. The larger the value of γ the sharper the turnover from the "rising" to the "flat" region of the velocity curve. Eq. 2.8 is flexible enough to accommodate the shape of essentially all rotation curves in the samples we consider here. We note that this formula has three

free parameters,[5] one more than the NFW profile. This fitting formula is plotted for several different combinations of parameters in Figure 2.9 alongside NFW and pseudo-isothermal V_c profiles.[6] The left panel shows that eq. 2.8 can accurately reproduce both NFW and pseudo-isothermal profiles, despite the fact that the logarithmic slopes of these profiles tend to different values at small radii, 0.5 and 1, respectively, as shown in the right panel of this figure. This figure also illustrates the difference between fits with different values of γ. Fits with $\gamma \gg 1$ rise linearly with radius out to $r \simeq r_t$ then quickly turn over, becoming flat at $r \gtrsim r_t$. Fits with lower γ have a much more gradual transition between the $V \propto r$ and $V \simeq$ constant parts of the velocity curve.

We have applied this fitting formula to the Hα rotation curve datasets of McGaugh et al. (2001),[7] de Blok and Bosma (2002),[8] and Swaters et al. (2003a),[9] hereafter M01, B02, and S03, respectively. The M01 sample consists of 26 LSB galaxies, the B02 sample consists of 26 LSB galaxies, and the S03 sample contains 10 dwarf galaxies and 5 LSB galaxies for a total of 67 galaxies in the total sample. Appendix A contains a table of properties of these galaxies as well as R-band images taken from the Second Generation Digitized Sky Survey (see `http://cadcwww.hia.nrc.ca/cadcbin/getdss`). Note that the raw Hα data was used, as opposed to the smoothed hybrid HI/Hα rotation curve data available for the M01 and B02 samples, in order to compile a dataset with error characteristics as uniform as possible. Following the practice of S03, a minimum error of 5 $\mathrm{km\,s^{-1}}$ was imposed on the raw data from all three samples. Note that five galaxies, F568-3, UGC 731, UGC 4325, UGC 5750, and UGC 11557, are common to two of the three

[5] An additional factor of $(1+x)^\beta$ was used by Courteau (1997) to improve fits to $\sim 10\%$ of the galaxies in his sample that exhibit a drop-off in the outer part of the rotation curve. For simplicity, we have not included this parameter in our fits.

[6] The density profile of this widely used approximation to the non-singular isothermal sphere is given by $\rho_{\rm iso}(r) = \rho_0/(1+(r/r_c)^2)$, where r_c is the radius of a constant density core and ρ_0 is the characteristic density of the core.

[7] `http://www.astro.umd.edu/~ssm/data`

[8] `ftp://cdsarc.u-strasbg.fr/cats/J/A+A/385/816`

[9] `http://www.robswork.net/data`

datasets. We treat both versions of the rotation curve data independently for these galaxies and note the good agreement between fits to them below.

The top, middle, and bottom rows of Figures 2.10 and 2.11 show a selection of rotation curves from the M01, B02, and S03 samples, respectively. For each rotation curve, a grid of χ^2 values is computed for fits obtained with eq. 2.8. The solid curves in Figures 2.10 and 2.11 show the best fit obtained for each rotation curve as determined by the minimum χ^2 value, subject to the following constraints:

$$\begin{aligned} r_t &> 0 \\ 0 < \gamma &\leq 5 \\ V_0 &\leq 2\, V_{\rm max} \end{aligned}$$

The allowed range in γ was chosen because fits with $\gamma \gtrsim 5$ correspond to a virtually right-angled transition between the rising and flat parts of the curve. The limit on V_0 was chosen in order to avoid fits with asymptotic velocities much greater than the maximum indicated by the data. The reduced chi-square, $\chi^2_{\rm red}$, and fit parameter values are shown in Figures 2.10 and 2.11 under the column labelled "min" for each rotation curve. All 67 rotation curves and fits are presented in Appendix B for completeness and the fit parameters for all rotation curves are given in Table 2.2, where the outermost radius with reliable data is listed as $r_{\rm outer}$. Raw Hα and smoothed hybrid HI/Hα rotation curves of the five galaxies common to two of M01, B02 and S03 are shown in Figure 2.12. We find broad consistency between the different versions of rotation curves: in most of these the values of r_t and V_0 are within $\sim$ 20% of one another. The value of γ is not as well-determined, and can vary by a factor of two or more. In §2.5.5, however, we show that most rotation curves are consistent with a wide range of γ values, therefore differences in the best fit parameter values of different versions of rotation curves do not significantly affect our main conclusions.

The top panel of Figure 2.13 shows the distribution of best fit γ values obtained for each sample. Each histogram in this figure is normalized to the total number of systems in each sample for ease of comparison. All three rotation curve datasets are broadly consistent with each other; most ($70\% \pm 5\%$) of the rotation curves in each sample are characterized by a value of $\gamma \lesssim 2$. These are typically gently-rising curves which turn over gradually as they approach the maximum asymptotic rotation speed, as shown by rotation curves in the left and middle columns of Figure 2.10. A significant ($\simeq 30\%$) number of galaxies with $\gamma > 2$ are also present, however. These are galaxies whose rotation curves feature a linear rise in velocity with radius and a much sharper transition from the rising to flat part, as shown by many of the rotation curves in Figure 2.11 and in the rightmost panels of Figure 2.10.

2.5.3 Halo Circular Velocity Profile Shapes

The bottom panel of Figure 2.13 shows the γ distribution obtained by fitting eq. 2.8 to the V_c profile of all dwarf and galaxy-sized halos. In order to consider various dynamical instances of a halo, we have included in the analysis about 20 different outputs for each system, spanning the redshift range $1 \lesssim z \leq 0$, giving a total of 266 halo profiles. At each redshift, we calculate the V_c profile at points separated by 1 h^{-1}kpc (physical) in radius for the galaxy halos and 0.2 h^{-1}kpc (physical) in radius for the dwarf halos, starting at the innermost reliably resolved radius $r_{\rm conv}$. Since no formal error bars exist for the halo profiles (Poisson errors are negligible for the numbers of particles in these halos), we assign a uniform error of ± 1 km s^{-1} to all points for the purpose of curve fitting. The V_c profiles were fit out to $r_{\rm outer} =$ 20 h^{-1}kpc (physical) for the galaxy halos and $r_{\rm outer} = 6$ h^{-1}kpc (physical) for the dwarf halos, corresponding to $4 - 5$ r_d, where r_d is the exponential scale length of the disks embedded in such halos, as predicted by the model of Mo et al. (1998) (see below).

We note that the best fit parameter values are somewhat sensitive to the region fitted; for example, fitting the $z = 0$ V_c profile of halo G5 out to $r_{\rm outer} = 10, 20, 40$, and $80\ h^{-1}$kpc results in best fit parameter values of $(r_t, \gamma, V_0) = (1.4\ h^{-1}\mathrm{kpc}, 0.4, 363\ \mathrm{km\,s^{-1}})$, $(1.6\ h^{-1}\mathrm{kpc}, 0.5, 312\ \mathrm{km\,s^{-1}})$, $(3.0\ h^{-1}\mathrm{kpc}, 0.9, 220\ \mathrm{km\,s^{-1}})$, and $(4.1\ h^{-1}\mathrm{kpc}, 1.4, 198\ \mathrm{km\,s^{-1}})$, respectively, whereas $(r_{\rm max}, V_{\rm max}) = (40.1\ h^{-1}\mathrm{kpc}, 197\ \mathrm{km\,s^{-1}})$ for this halo. The shape parameter γ therefore increases as a function of $r_{\rm outer}$, but in general is limited to values of $\gamma \lesssim 1$ provided that $r_{\rm outer} \lesssim r_{\rm max}$, i.e., provided that fits do not extend beyond the radius at which it starts to decline. In addition, because velocity increases monotonically with radius in eq. 2.8 (unlike halo V_c profiles which peak at a finite radius), the asymptotic velocity V_0 tends to overestimate $V_{\rm max}$.

The γ distribution of all galaxy and dwarf halos and that of the dwarf halos alone are shown as the green and red histograms, respectively, both of which are normalized to the total number of halos. The halo γ distribution peaks at $\gamma \simeq 0.6$, and has a dispersion of order ~ 0.4. For illustration, the three G1 V_c profiles shown in the bottom panel of Figure 2.8 have $\gamma = 0.73$, 0.65, and 0.48 at $z = 1.1$, 0.48, and 0, respectively. There is no significant difference between the galaxy and dwarf halo γ distributions.

We note that the contribution of a baryonic component has not been taken into account in our analysis of the simulated V_c profiles. In order to assess the effect of a baryonic disk on the shape of the V_c profile, we construct an analytic mass model comprised of an NFW halo and an exponential disk. We use the prescription of Mo et al. (1998) to determine the scale length of the disk, r_d, as a function of the concentration, $c = r_{200}/r_s$, and spin parameter, λ, of the NFW halo, and the mass, m_d, and angular momentum, j_d, of the disk (expressed as fractions of the halo mass and angular momentum, respectively). Figure 2.15 shows the inner V_c profiles of the disk and halo components along with best fits using eq. 2.8.

The V_c profile of a dwarf NFW halo with $r_{200} = 50\ h^{-1}$kpc and concentration $c = 13.7$, as predicted by the Bullock et al. (2001) concentration model, fit over the

range $r_{\rm min} = 0.2\ h^{-1}$kpc to $r_{\rm outer} = 6.0\ h^{-1}$kpc is best fit by a curve with $\gamma = 0.59$. The addition of a disk with $m_d = j_d = 0.05$ to a halo with $\lambda = 0.1$ (as expected for LSB galaxies), results in best fits with $\gamma = 0.64$ for the halo after adiabatic contraction ($V_{\rm NFW,adia}$), and $\gamma = 0.66$ for the total circular velocity, $V^2_{\rm tot} = V^2_{\rm disk} + V^2_{\rm NFW,adia}$. Note that this choice of parameters for the size and mass of the disk yields a central surface brightness of 22.5 mag/arcsec^2, assuming $\Upsilon_B = 2$ for the B-band stellar mass-to-light ratio, similar or slightly brighter than that of a typical LSB galaxy. We therefore conclude that, for reasonable LSB disk parameters, the increase in γ due to the presence of the disk is small. In Figure 2.14 we compare the distribution of γ values of the combined LSB galaxy sample with that of high surface brightness (HSB) galaxies from the samples of Mathewson et al. (1992) Courteau (1997). The γ distributions of LSB and HSB galaxies appear surprisingly similar, suggesting that even massive disks have a only minor effect on rotation curve shapes as measured by the best fit γ value.

Taken at face value, the halo γ distribution in Figure 2.13 appears to be inconsistent with that of LSB galaxies. Most halos have $\gamma < 1$ compared to only about one third of LSBs. However, the rotation curve data have error estimates associated with each of the velocities, whereas the halo V_c profiles have negligible statistical errors. One should take this into account in order to decide whether the shapes of LSB rotation curves are consistent with simulated halo V_c profiles. In §2.5.5 we address this issue in detail, identifying galaxies that are inconsistent with the structure of CDM halos even after taking the observational uncertainties into consideration.

2.5.4 The Concentration of LSB Halos

The discussion of the preceding section focused on the *shape* of the rotation curves and halo V_c profiles. We now turn our attention to the physical parameters of the fits, in order to address claims that LSB galaxies are surrounded by halos of much lower

concentration than expected in the ΛCDM scenario (McGaugh and de Blok, 1998; de Blok et al., 2001b). We emphasize again that it is important to characterize both the observational data and the simulations in a way that is as independent as possible from fitting formulae or extrapolation. Alam et al. (2002) recently proposed a simple and useful dimensionless measure of central density that satisfies these criteria,

$$\Delta_{V/2} \equiv \frac{\overline{\rho}(r_{V/2})}{\rho_{\rm crit}}. \tag{2.9}$$

The central density parameter, $\Delta_{V/2}$, measures the mean density contrast (relative to the critical density for closure) within the radius $r_{V/2}$ at which the rotation speed drops to one half of its maximum value, $V_{\rm max}$. In practice, we estimate $\tilde{\rho}(r)$ by $3\,V_c^2(r)/4\pi G r^2$, a quantity that is easily measured both in galaxies with rotation curve data (and well-defined $V_{\rm max}$) and in simulated halos. To be precise, we shall adopt $r_{V/2} = r_t/(2^\gamma - 1)^{1/\gamma}$ as the radius where the velocity equals one half of its asymptotic value V_0.

The top panel of Figure 2.16 shows $\Delta_{V/2}$ as a function of $V_{\rm max}$ for all simulated halos. The open and solid symbols show the "true" $\Delta_{V/2}$ values calculated directly from the V_c profiles of the dwarf- and galaxy-sized halos, respectively. The starred and skeletal symbols show the $\Delta_{V/2}$ values estimated from fits to the V_c profiles. This figure illustrates the uncertainty in the central densities and maximum velocities inferred from fits to rotation curve data. Recall that halo V_c profiles are fit out $r_{\rm outer} \lesssim 0.5\ r_{\rm max}$ in most cases, and, as a result, V_0 overestimates the true $V_{\rm max}$ of the halo by up to 60% in some cases. This implies that values of $\Delta_{V/2}$ estimated from fits to the halo profiles may underestimate the true central density parameter by up to a factor of five.

The solid curves in all panels of Figure 2.16 correspond to the predictions of the Eke et al. (2001) halo concentration model for NFW halos in the ΛCDM cosmology

assumed in our simulations.[1] The dotted curves show the predictions of the Bullock et al. (2001) concentration model, together with the 1 σ halo-to-halo scatter predicted by their model.[2]

The middle panel of Figure 2.16 shows that the "true" central densities of the simulated dwarf, galaxy, and cluster halos in our sample (skeletal symbols) are in rough agreement with both models; the Bullock et al. (2001) model reproduces the central densities of simulated halos slightly better on the scales of dwarf halos, whilst the ENS model does better on the scale of clusters. This figure also shows the estimated central densities of all galaxies in the M01, B02, and S03 samples (open symbols). We find that a large fraction of galaxies in the LSB sample lie below the ΛCDM predictions of the simulated halos and the concentration models. Based on this apparent excess of low-concentration galaxies, Zentner and Bullock (2002) have argued for substantial revision of the "concordance" ΛCDM scenario, such as tilted power spectra, running spectral index, or perhaps a lower σ_8. However, as previously noted, $V_{\rm max}$ and $\Delta_{V/2}$ are not well-defined for some LSBs, and may bias the halo central density parameter estimates inferred from rotation curve data. We explore this issue in detail in the following section.

2.5.5 Identifying Galaxies Inconsistent with ΛCDM Halos

We now attempt to identify rotation curves that are of sufficient quality to provide meaningful constraints on the structure of dark matter halos. A glance at the rotation curves shown in Figures 2.10 and 2.11 indicates that uncertainties in the data allow for a variety of acceptable fit parameters. In order to identify galaxies that are robustly

[1] A code which calculates this model is made available by the authors at `http://pinot.phys.uvic.ca/~jfn/cens/`

[2] A code which calculates this model is made available by the authors at `http://cfa-www.harvard.edu/~jbullock/WWW/CVIR/`. Note that this code implements the correct 1 σ halo-to-halo scatter for this model, $\Delta(\log c_{\rm vir}) = 0.14$, as opposed to the erroneous value $\Delta(\log c_{\rm vir}) = 0.18$ reported in the text (but not the figures) of Bullock et al. (2001) (for further details, see Wechsler et al., 2002).

discrepant with the predictions of ΛCDM cosmologies, we search the grid of $\chi^2_{\rm red}$ values for the best fit which satisfy the following constraints:

$$\begin{aligned} r_t &> 0 \\ 0 < \gamma &\leq 1 \\ V_0 &\leq 2\,V_{\rm max} \\ |\log \Delta_{V/2} - \log \Delta_{V/2,\rm CDM}| &\leq 0.7, \end{aligned}$$

i.e., with γ limited to the range found for simulated halos and central densities within a factor of 5 of the value predicted for ΛCDM halos. Here we take the median prediction of the Bullock et al. (2001) model for a halo with $V_{\rm max}$ equal to the fit V_0 as the fiducial value $\Delta_{V/2,\rm CDM}$. We note that this model predicts a 1 σ scatter of $\Delta \log \Delta_{V/2} \simeq 0.4$, however, we choose a more generous range of 0.7 to allow for uncertainties in the predictions of the model, as shown by the halos which fall outside the 1 σ limits on $\Delta_{V/2}$ in Figure 2.16.

In Figure 2.17 we plot $\chi^2_{\rm red,min}$, the reduced chi-square value found for the best fit, against $\chi^2_{\rm red,CDM}$, the minimum value found for fits subject to these additional constraints. Plotted in this way, the data fall into three broad categories:

A. rotation curves that are well fit by eq. 2.8 and for which a good fit with ΛCDM-compatible parameters can also be found, i.e., $\chi^2_{\rm red,min} \leq 1.5$ and $\chi^2_{\rm red,CDM} \leq 1.5$.

B. rotation curves that are well fit by eq. 2.8 but for which no good fit with ΛCDM-compatible parameters can be found, i.e., $\chi^2_{\rm red,min} \leq 1.5$ and $\chi^2_{\rm red,CDM} > 1.5$.

C. rotation curves that are poorly fit by eq. 2.8, i.e., $\chi^2_{\rm red,min} > 1.5$ and $\chi^2_{\rm red,CDM} > 1.5$. These are rotation curves that do not rise smoothly and monotonically with radius, and for which no simple fitting function provides a good fit.

The choice of $\chi^2_{\rm red} \leq 1.5$ as the criterion for a good fit is somewhat arbitrary, but leads to a natural grouping of the data points in Figure 2.17 shown by the regions

bounded by solid lines and labelled "A," "B," and "C." The number of galaxies in each of these regions is 48, 7, and 12 for groups A, B, and, C, respectively. The rotation curves shown in Figure 2.10 belong to group A, whereas those shown in Figure 2.11 are members of groups B and C, as identified by the labels below the name of each galaxy.

We use filled symbols in Figure 2.17 to denote rotation curves for which the asymptotic velocity of the best fit is no more than 20% greater than the maximum velocity observed in the data, i.e., $V_0 < 1.2\ V_{\rm max}$. These galaxies, which represent about half of the total sample, have maximum velocities that are reasonably well-defined by their rotation curves. Galaxies with $V_0 \geq 1.2\ V_{\rm max}$, represented by open symbols, typically have rotation curves that are still rising at their outermost radius and consequently have poorly constrained fit parameters and $\Delta_{V/2}$ values. In fact, most of these galaxies have best fits with $V_0 = 2\ V_{\rm max}$, the maximum asymptotic velocity permitted by our fitting criteria. In these cases, the rotation curve data resolve only the rising part of the circular velocity profile and are clearly insufficient to constrain the structure and maximum circular velocity of the dark matter halo of the corresponding galaxy. Examples of these include NGC 4455 in Figure 2.10, and ESO 0840411, UGC 4499, UGC 11861 in Figure 2.11.

In summary, galaxies in group A are consistent with ΛCDM in terms of their inferred central densities and the shape of their rotation curves; galaxies in group B are inconsistent with ΛCDM; and galaxies in group C have irregular rotation curves for which fitting functions like eq. 2.8 do not provide a good fit. Of the six rotation curves in group B which pose a problem for ΛCDM only four of these have best fits with asymptotic velocities within 20% of the maximum observed rotation velocity.

The bottom panel of Figure 2.13 shows the γ distribution of rotation curves in each of the three groups. The open histogram represents the distribution of the entire sample, the horizontal hatched portion shows the contribution of LSBs from groups A and B, and the solid portion shows the contribution of group B only. It is clear

from this panel that most of the rotation curves that are best fit by $\gamma > 1$ are actually members of group A, for which a reasonable $\gamma \leq 1$ fit (consistent with CDM) exists. In fact, the majority of rotation curves with $\gamma \simeq 5$ belong to group A. The rightmost column of Figure 2.10 shows three examples of these. The rotation curves of these galaxies do not vary smoothly as a function of radius and some contain points with rather large error bars. As a result, these data, although best fit by a curve with an abrupt change in slope (high γ), can also be well fit with a more gently flattening curve (lower γ) by compensating with a different value of V_0.

Most of the galaxies in group B have $\gamma \simeq 5$, however, the case for a high-γ fit is hardly unambiguous in the raw data. In most cases, the data cuts off before the flat part of the curve is well resolved, and the fits are driven to high values of γ because this allows for a positive velocity gradient in the outer regions, not because the data show a sharp transition between a rising part and a flat part. This is corroborated by the fact that $r_t \gtrsim r_{\rm outer}$ even for the four galaxies with $V_0 < 1.2\ V_{\rm max}$, illustrating that our criterion for rotation curves having well-defined maximum velocities is somewhat lenient. In summary, the group B galaxies with high γ have rotation curves which sample only the rising parts of these curves, therefore it is difficult to determine the overall shapes of these curves.

We also note that the rotation curve of galaxy F568-3 derived by S03 (see Figure 2.11) is a member of group B, however, the M01 rotation curve of the same galaxy (see Figure 2.10) belongs to group A. The M01 data does extend out 20% further than the S03 data, but the best fit parameter values for these two rotation curves are nearly identical and both have $\gamma \simeq 5$. The error estimates on the S03 velocities are significantly smaller, however, resulting in $\chi^2_{\rm red,CDM} > 1.5$ for the best ΛCDM-compatible fit to the S03 rotation curve. This illustrates the sensitivity of the χ^2 statistic to error estimates and also underlines the somewhat arbitrary nature of the $\chi^2_{\rm red} \leq 1.5$ criterion for a good fit.

We show the central densities of the LSB galaxies identified by membership in

A, B, and C groups in the bottom panel of Figure 2.16. Only points with well determined $V_{\rm max}$, i.e., $V_0 < V_{\rm max}$, are shown as solid symbols in this plot. Note that galaxies with poorly constrained maximum velocities may have best fit values of V_0 that underestimate or overestimate the true maximum velocity of the galaxy, since the fit is essentially an extrapolation of data which samples only the rising part of the rotation curve. As noted by Alam et al. (2002), errors in the determination of $V_{\rm max}$ and $r_{V/2}$ have cancelling effects if the rotation curve is linear near $r_{V/2}$. However, this may not to be the case for galaxies such as NGC 4455 shown in Figure 2.10. Estimates of $\Delta_{V/2}$ based on fits to halo V_c profiles out to radii smaller than $r_{\rm max}$ can underestimate the true central density by up to a factor of five. Therefore, it is perhaps not surprising that many of the LSB points which lie below the ΛCDM predictions in the middle panel of Figure 2.16 correspond to galaxies whose rotation curves do not extend out far enough to resolve their maximum velocities and are thus excluded from the bottom panel.

As in the bottom panel of Figure 2.13, the $\Delta_{V/2}$ values inferred from best fits to rotation curves in group A cannot be considered to be robustly inconsistent with ΛCDM since acceptable fits with values of $\Delta_{V/2}$ within a factor of five of the theoretical predictions can be obtained for these galaxies. The $\Delta_{V/2}$ values of group C galaxies with well-defined $V_{\rm max}$ cannot be dismissed out of hand, since some rotation curves with "noisy" data have reasonably well-determined $r_{V/2}$ radii despite having relatively large $\chi^2_{\rm red}$ values. In any event, these galaxies, represented by the solid squares in the bottom panel of Figure 2.16, appear to be evenly scattered above and below the predictions of the Bullock et al. model.

Of the group B galaxies, the maximum velocity, and therefore $\Delta_{V/2}$, is uncertain for most, if not all, of them. On the other hand, if we assume that our estimates of $\Delta_{V/2}$ are robust for galaxies with $V_0 < 1.2\ V_{\rm max}$, we are faced with galaxies that have roughly the same $V_{\rm max}$, but central densities that vary by almost two orders of magnitude.

As previously noted, Zentner and Bullock (2002) have argued for substantial revision of the ΛCDM scenario based on the low concentration galaxies in LSB samples. It appears unlikely, however, that any such modification to the "concordance" cosmology would result in the larger range of central densities suggested by the data. We also note that the central densities of HSB galaxies shown in the bottom panel of Figure 2.14 show an even larger scatter in $\Delta_{V/2}$ values, suggesting that baryonic physics may be responsible for the large variation in central densities. It is unclear at this point how to reduce the disagreement, but any resolution to the puzzle must explain why so many LSBs are actually consistent with ΛCDM halos and why any disagreement is confined to a minority of systems. The possibility remains that some complex astrophysical process not yet considered in the models might actually be behind the discrepancy and that no radical modification to the ΛCDM paradigm is called for.

In summary, we find that the shapes of the rotation curves and the inferred central densities of most galaxies that appear inconsistent with the predictions of ΛCDM are in fact insufficiently constrained by the data. Of the 67 galaxies in the entire dataset, a ΛCDM-compatible fit can be found for 48 of these, and an additional 12 have rotation curves that cannot be well fit by any smoothly varying function like eq. 2.8. The rotation curves of the remaining six galaxies are characterized by a linear rise in velocity with radius; however, many of these do not extend out far enough to accurately determine their shapes and central densities. We conclude that, within the limitations of the observational data, this sample of LSB rotation curves is not manifestly inconsistent with the predictions of ΛCDM cosmological models.

2.6 Conclusions

We present results from a set of high resolution cosmological simulations of dark matter halos formed in a ΛCDM cosmogony. Seven Milky Way-sized galaxy halos were

simulated at various mass, time, and spatial resolutions, enabling us to investigate the convergence properties of cosmological N-body simulations. We have examined the internal structure of the highest resolution realization of each halo, with particular emphasis on the logarithmic slope of the inner density profile. Finally, we have compared the circular velocity profiles of these halos and of additional dwarf galaxy halos with the observed rotation curves of a large sample of dwarf and LSB galaxies.

Our main conclusions may be summarized as follows.

- The convergence criteria proposed by Power et al. (2003) are robust, and provide a conservative estimate of the minimum radius at which the circular velocity profile of simulated halos can be reliably predicted (to within 10%). According to these criteria, the highest resolution galaxy halos we have simulated (which contain 2-4 million particles within the virial radius) are reliably resolved down to $r_{\rm conv} \simeq 1\ \ h^{-1}$kpc.

- The slope of ΛCDM halo density profiles becomes progressively shallower all the way down to the minimum reliably resolved radius, with little sign of convergence to a well-defined power law near the centre.

- In general, the slope changes with radius more gradually than predicted by the NFW formula, which leads some halos to be better described by profiles with steeper cusps, such as the modification to the NFW formula proposed by Moore et al (1999). There is, however, significant variation from halo to halo in the radial dependence of the slope. Some systems are better fit by the NFW profile, and others by the Moore et al formula. At $r_{\rm conv}$, however, all the density profiles are significantly shallower than $r^{-1.5}$, the asymptotic value advocated by Moore et al. (1999a).

- A comparison of the circular velocity profiles of CDM halos with rotation curves of LSB galaxies indicates that the shapes of the rotation curves and the inferred

central densities of most (about 70%) LSB galaxies are consistent with those of simulated halos within the limitations imposed by observational error. Of the remainder, 20% have irregular rotation curves which cannot be fit by simple fitting functions, and 10% are inconsistent with CDM halos.

We conclude that the inner structure of ΛCDM halos is not manifestly inconsistent with the majority of LSB rotation curves. Although some rotation curves feature a sharp transition from the rising to the flat part of the curve, most of these can also accommodate a fit that is compatible with the shapes of CDM halo V_c profiles. A small minority of rotation curves exhibit a linear rise in velocity over a substantial range in radius that appears inconsistent with the shapes of halo V_c profiles. The data also suggest that the central densities of galaxies inferred from their rotation curves may exhibit a larger variation than is predicted for ΛCDM halos.

We note however, that the analysis presented in this paper is based on the assumption that the gas rotation speed is directly proportional to the spherically-averaged halo circular velocity, an assumption which may not be valid for real galaxies. CDM halos, for example, are known to be triaxial, which may lead gaseous disks to deviate systematically and significantly from simple coplanar circular orbits. In Chapter 4 we discuss whether such asymmetries in the potential are able to account quantitatively for the observed variety of LSB rotation curves and concentrations.

Table 2.1: Numerical and physical properties of simulated halos

Label	R_{200} h^{-1}kpc	M_{200} $10^{10}\,h^{-1}M_{\odot}$	N_{200}	ϵ h^{-1}kpc	$N_{\Delta t}$	Code	$r_{\rm conv}$ h^{-1}kpc
G1/32^3	202.1	191.8	5758	10	800	PKDGRAV	22.9
G1/64^3	205.2	201.1	48318	2.5	1600	PKDGRAV	7.7
G1/128^3	205.1	200.6	383560	1.25	3200	PKDGRAV	3.2
G1/256^3	214.4	229.4	3447447	0.15625	RhoSgAcc	GADGET	1.4
G2/32^3	231.4	288.1	8583	10	800	PKDGRAV	24.2
G2/64^3	231.8	289.8	69088	3.5	1600	PKDGRAV	7.0
G2/128^3	234.1	298.6	566456	1.25	3200	PKDGRAV	2.9
G2/256^3	232.6	292.9	4523986	0.5	6400	PKDGRAV	1.3
G3/32^3	218.7	243.1	5484	10	800	PKDGRAV	22.5
G3/64^3	215.0	231.1	41719	3.5	1600	PKDGRAV	9.3
G3/128^3	214.5	229.7	331314	1.25	3200	PKDGRAV	3.9
G3/256^3	212.7	223.8	2661091	0.45	6400	PKDGRAV	1.7
G4/64^3	164.9	104.4	53331	2.5	3200	PKDGRAV	5.7
G4/128^3	165.4	105.3	432313	1	6400	PKDGRAV	2.4
G4/256^3	164.0	102.6	3456221	0.3	12800	PKDGRAV	1.0
G5/64^3	165.3	105.0	62066	3	800	PKDGRAV	5.7
G5/128^3	165.7	105.8	496720	1	3200	PKDGRAV	2.3
G5/256^3	165.0	104.5	3913956	0.35	6400	PKDGRAV	1.0
G6/64^3	160.7	96.5	57008	3	800	PKDGRAV	6.0
G6/128^3	163.2	101.1	474844	1	3200	PKDGRAV	2.5
G6/256^3	162.5	99.9	3739913	0.35	6400	PKDGRAV	1.0
G7/64^3	159.7	94.7	55947	3	800	PKDGRAV	5.8
G7/128^3	160.9	96.9	454936	1	3200	PKDGRAV	2.4
G7/256^3	160.3	95.8	3585676	0.35	6400	PKDGRAV	1.0
D1	32.3	0.8	784980	0.0625	EpsAcc	GADGET	0.3
D2	34.1	0.9	778097	0.0625	EpsAcc	GADGET	0.4
D3	32.3	0.8	946421	0.0625	EpsAcc	GADGET	0.3
D4	34.7	1.0	1002098	0.0625	EpsAcc	GADGET	0.3
C1	1502.1	78842.4	1565576	5.0	EpsAcc	GADGET	16.8
C2	1468.1	73618.2	1461017	5.0	EpsAcc	GADGET	16.9

continued on next page

continued from previous page

Label	R_{200} h^{-1}kpc	M_{200} $10^{10}\,h^{-1}M_{\odot}$	N_{200}	ϵ h^{-1}kpc	$N_{\Delta t}$	Code	$r_{\rm conv}$ h^{-1}kpc
C3	1300.6	51179.5	1011918	5.0	EpsAcc	GADGET	16.1
C4	1316.7	53101.9	1050402	5.0	EpsAcc	GADGET	15.9
C5	1375.5	60541.8	1199299	5.0	EpsAcc	GADGET	16.2
C6	1521.1	81870.6	1626161	5.0	EpsAcc	GADGET	15.5
C7	1245.8	44979.4	887837	5.0	EpsAcc	GADGET	16.4
C8	1365.4	59220.3	1172850	5.0	EpsAcc	GADGET	16.8

Table 2.2: Properties of rotation curves and fit parameters

Galaxy ID	$r_{\max}$ (kpc)	$V_{\max}$ (km/s)	r_{outer} (kpc)	r_t (kpc)	γ	V_0 (km/s)	$\log \Delta_{V/2}$	$\chi^2_{\text{red,min}}$	$\chi^2_{\text{red,CDM}}$
McGaugh et al. (2001, M01):									
ESO0140040	11.5	300.2	29.2	0.9	0.4	509	5.0	3.0	3.0
ESO0840411	8.8	57.4	8.8	11.3	1.2	114	4.2	0.7	3.5
ESO1200211	3.2	30.1	3.5	1.1	5.0	23	5.2	0.4	0.7
ESO1870510	2.1	41.2	3.0	1.4	0.8	71	5.1	0.3	0.3
ESO2060140	6.0	119.8	11.6	1.8	1.6	123	6.1	1.0	1.1
ESO3020120	10.9	91.5	10.9	3.1	1.8	91	5.4	0.3	0.3
ESO3050090	2.8	76.9	4.7	2.8	5.0	57	5.2	2.2	2.8
ESO4250180	8.8	175.2	14.2	5.5	0.6	314	4.6	1.2	1.2
ESO4880049	6.0	101.0	6.0	3.5	0.8	181	5.1	0.7	0.7
F563-1	13.9	134.2	17.0	3.2	2.0	129	5.7	0.2	0.3
F568-3	11.1	100.4	11.1	5.0	5.0	100	5.2	0.5	1.2
F571-8	10.0	140.1	10.0	2.8	0.6	261	5.0	0.8	0.8
F579-V1	9.9	167.0	11.5	1.1	1.2	127	6.3	1.9	1.9
F583-1	6.3	82.1	7.2	3.7	2.0	88	5.2	0.5	0.7
F583-4	6.7	70.6	6.7	1.8	0.6	128	4.8	1.2	1.3
F730-V1	13.3	156.3	14.8	2.3	1.4	151	5.9	0.5	0.6
UGC4115	0.9	40.4	1.0	1.1	1.2	74	5.9	0.5	0.6
UGC5750	9.0	78.8	9.0	7.8	5.0	81	4.6	0.4	4.5
UGC6614	25.1	217.1	35.3	8.7	2.2	212	5.3	5.7	6.8
UGC11454	10.5	153.1	12.2	2.7	1.2	173	5.8	1.1	1.1
UGC11557	6.2	83.4	6.2	8.2	1.4	149	4.8	1.9	3.3
UGC11583	1.5	38.7	1.5	0.9	5.0	35	5.8	0.3	0.4
UGC11616	9.3	151.4	9.6	2.3	1.6	143	6.0	0.6	0.7
UGC11648	12.7	142.7	12.7	0.8	0.4	277	4.6	2.1	2.2
UGC11748	6.0	264.6	21.0	2.3	5.0	242	6.6	7.2	40.4
UGC11819	8.4	157.4	11.6	4.4	1.8	178	5.7	0.7	0.9
de Blok and Bosma (2002, B02):									
DDO47	1.4	65.6	1.5	1.6	0.7	119	5.2	0.3	0.3
DDO52	0.7	40.6	0.8	2.1	5.0	78	5.7	1.0	1.3
DDO64	2.1	50.9	2.1	2.2	1.0	100	5.3	0.4	0.4
DDO185	2.2	57.4	2.2	5.9	5.0	114	5.2	0.5	0.9
DDO189	3.8	84.2	3.8	5.3	0.8	168	4.7	1.2	1.2
IC2233	6.5	95.7	7.4	3.9	0.6	191	4.4	2.0	2.3

continued on next page

continued from previous page

Galaxy ID	r_{max} (kpc)	V_{max} (km/s)	r_{outer} (kpc)	r_t (kpc)	γ	V_0 (km/s)	$\log \Delta_{V/2}$	$\chi^2_{red,min}$	$\chi^2_{red,CDM}$
F563-1	9.3	108.5	9.7	1.3	0.6	147	5.2	0.3	0.3
NGC100	7.7	107.3	8.3	2.1	1.2	110	5.6	0.7	0.7
NGC1560	4.4	82.7	4.7	2.3	0.6	156	4.7	1.7	1.7
NGC2366	2.8	68.7	3.1	0.9	5.0	36	5.8	2.5	2.8
NGC3274	2.4	86.3	2.5	0.4	0.6	134	6.1	0.7	0.7
NGC4395	5.0	95.9	5.2	1.2	0.6	143	5.2	0.8	0.8
NGC4455	2.5	50.0	2.6	1.7	0.8	97	5.2	0.3	0.3
NGC5023	3.6	90.6	4.1	1.6	0.8	144	5.6	1.2	1.2
UGC628	13.8	141.4	13.8	1.8	1.2	130	5.9	0.7	0.8
UGC711	15.4	110.0	15.4	7.3	1.2	128	4.7	1.8	3.6
UGC731	4.9	73.7	5.0	1.3	3.8	71	6.1	0.5	0.7
UGC1230	13.6	118.7	13.6	3.9	5.0	105	5.5	0.3	0.6
UGC1281	2.4	52.9	2.9	2.5	5.0	48	5.2	0.7	1.8
UGC3137	5.0	154.7	5.4	2.3	5.0	102	5.9	0.4	0.6
UGC3371	5.1	73.8	6.1	3.5	2.6	69	5.1	0.5	0.6
UGC4173	0.8	20.5	2.5	0.1	3.2	12	6.7	0.1	0.1
UGC4325	4.6	128.8	4.6	3.0	3.6	114	5.7	0.9	0.9
UGC5005	8.1	66.2	10.4	2.5	5.0	56	5.3	0.3	0.3
UGC5750	8.0	80.0	9.4	9.4	5.0	90	4.6	0.7	5.4
UGC10310	3.9	78.1	5.2	5.5	2.0	104	5.0	0.4	0.5
Swaters et al. (2003a, S03):									
F563-V2	7.5	113.1	7.5	2.5	4.8	113	5.9	0.04	1.2
F568-1	8.6	130.1	8.6	2.6	1.0	169	5.6	0.3	0.3
F568-3	5.6	111.2	7.1	5.0	4.8	106	5.3	1.2	1.9
F568-V1	8.9	124.9	8.9	2.2	1.2	135	5.8	0.6	0.7
F574-1	11.5	104.2	11.5	2.3	1.2	114	5.6	0.4	0.4
UGC731	2.1	66.1	2.2	1.5	4.6	66	5.9	0.6	0.7
UGC2259	1.7	93.7	2.8	0.8	2.0	83	6.5	1.7	1.8
UGC4325	2.8	104.6	2.8	2.8	1.0	191	5.7	0.5	0.5
UGC4499	2.6	63.7	2.7	6.1	4.8	127	5.2	1.0	1.6
UGC5721	2.2	80.4	2.4	0.4	0.6	126	6.0	0.4	0.4
UGC8490	1.3	74.0	1.3	1.6	1.0	141	5.9	0.8	0.8
UGC11557	6.8	80.1	6.8	5.6	0.8	160	4.6	0.5	1.1
UGC11707	2.9	62.3	3.0	1.3	0.8	102	5.5	0.3	0.3
UGC11861	8.1	164.0	8.1	4.3	0.6	327	4.8	3.8	3.8
UGC12732	2.7	67.2	3.0	1.4	2.4	57	5.8	0.7	0.8

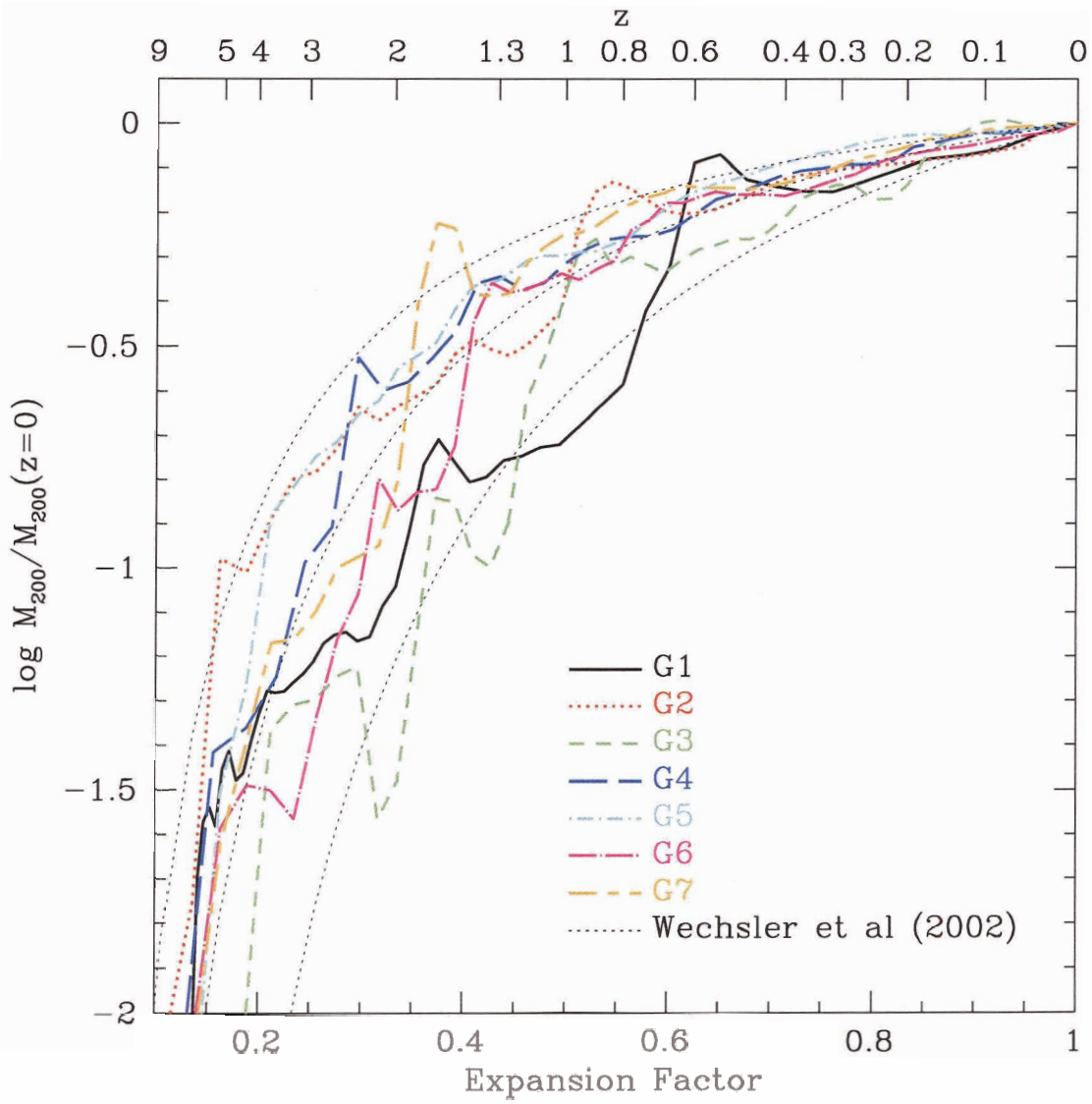

Figure 2.1: Evolution of the mass within the virial radius M_{200} normalized to the mass at $z = 0$ for the $N_{\rm sbox} = 256^3$ versions of our seven galaxy-sized halos. Most halos undergo a substantial merger at $z \sim 2$ which increases their mass at that time by a factor of two or more. Halo mass accretion histories are reasonably well-described by the fitting formula, eq. 2.3, proposed by Wechsler et al. (2002), shown for three different values of the free parameter α_c (from left to right, $\alpha_c = 0.5, 0.8, 1.4$).

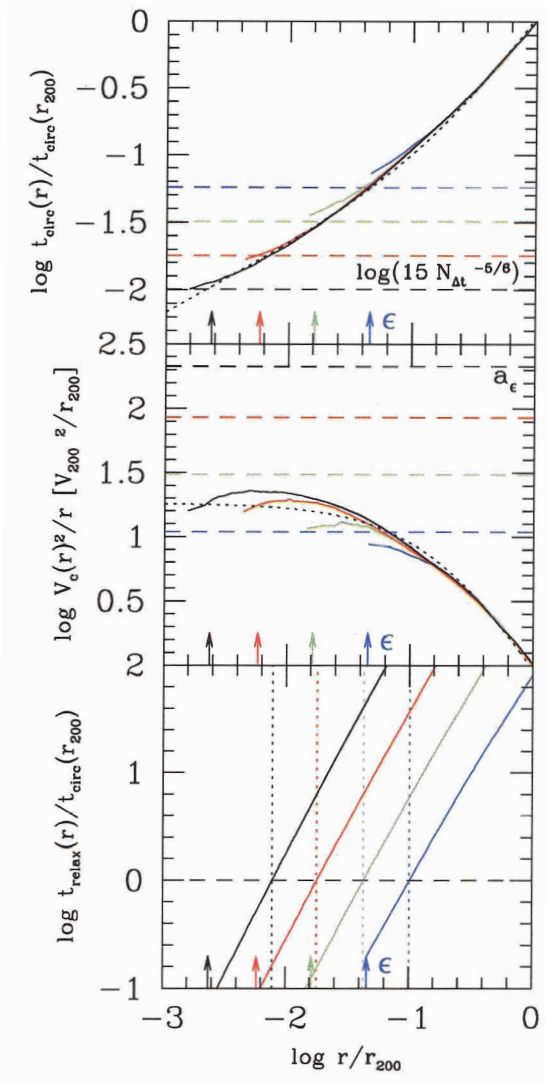

Figure 2.2: The structure of halo G3 at different mass, time, and spatial resolutions. The value of the softening parameter ϵ is indicated by arrows in the three panels. The number of timesteps and particles are listed in Table 2.1. Runs with 256^3, 128^3, 64^3, and 32^3 high-resolution particles are shown from left to right, respectively. Dotted curves show an NFW profile with concentration $c = 5.3$ and $r_{200} = 143.4\ h^{-1}$kpc. *Upper panel:* Local circular orbit period $t_{\rm circ}$ versus radius; radii at which the circular orbital timescale is less than $15\ N_{\Delta t}^{-5/6}$, indicated by the dashed lines for each simulation, are unresolved due to insufficient time resolution. *Middle panel:* Mean radial acceleration profile $V_c(r)^2/r$; untrustworthy radii are those corresponding to accelerations greater than the limiting acceleration imposed by the softening $a_\epsilon \simeq 0.5\ V_{200}^2/\epsilon$, shown by the dashed lines. *Lower panel:* Collisional relaxation time $t_{\rm relax}$ versus radius; convergence requires $t_{\rm relax} \gtrsim t_{\rm circ}(r_{200})$. Vertical dotted lines indicate the radius, $r_{\rm conv}$, beyond which this condition (the strictest of the three) is satisfied.

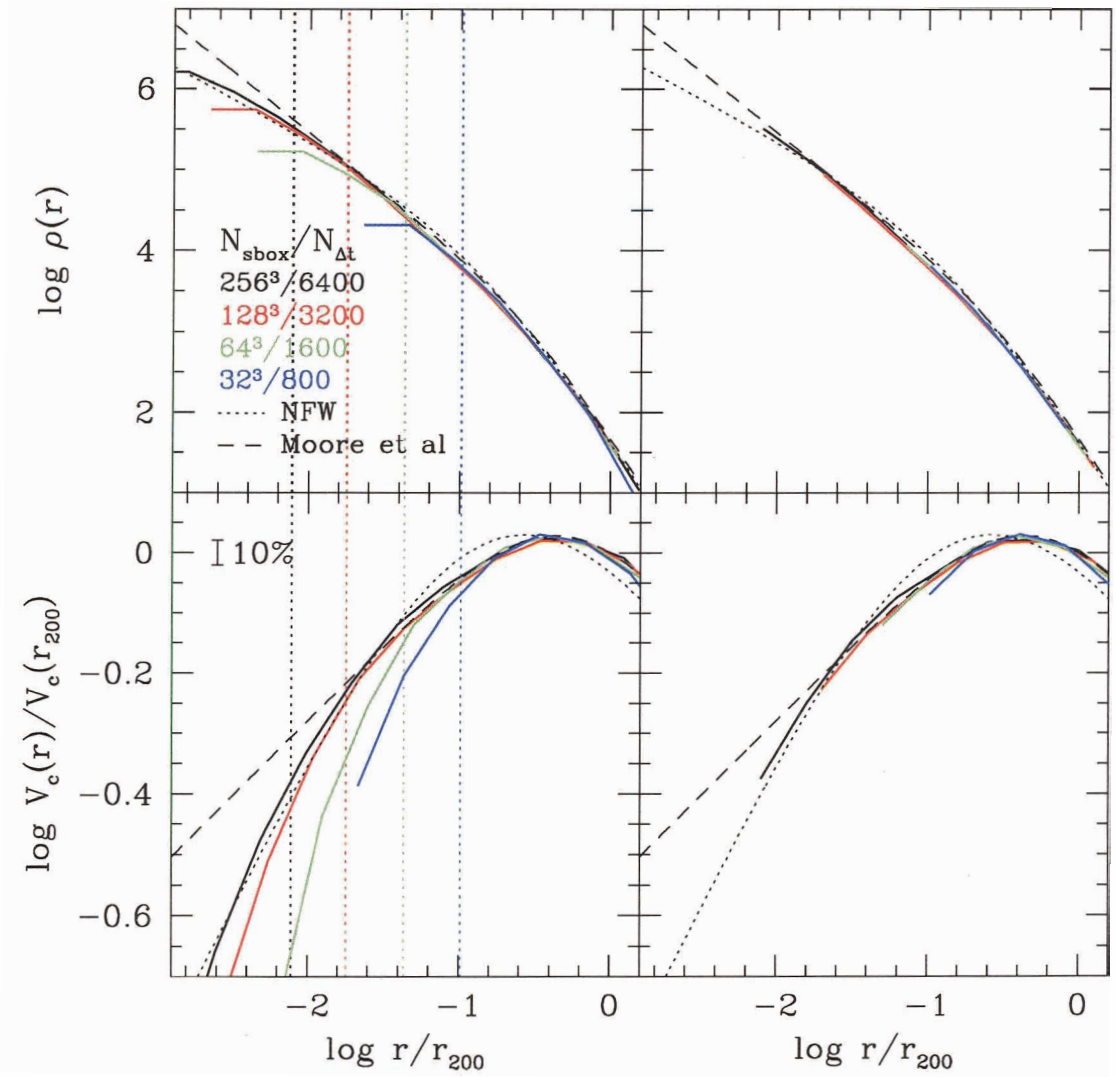

Figure 2.3: *Upper left panel:* Density profiles of halo G3 at four different levels of mass resolution, plotted down to radii containing 50 particles. Dashed and dotted curves show best fit Moore et al. and NFW profiles, respectively (see text for fitting details). Vertical dotted lines indicate the minimum converged radius, $r_{\rm conv}$, for each run. *Upper right panel:* Same density profiles plotted only for converged radii. The discrepancy between lower resolution runs and the highest resolution simulation at small radii is no longer apparent when only reliably resolved radii are considered. Lower panels are as the upper ones, but for the circular velocity profiles.

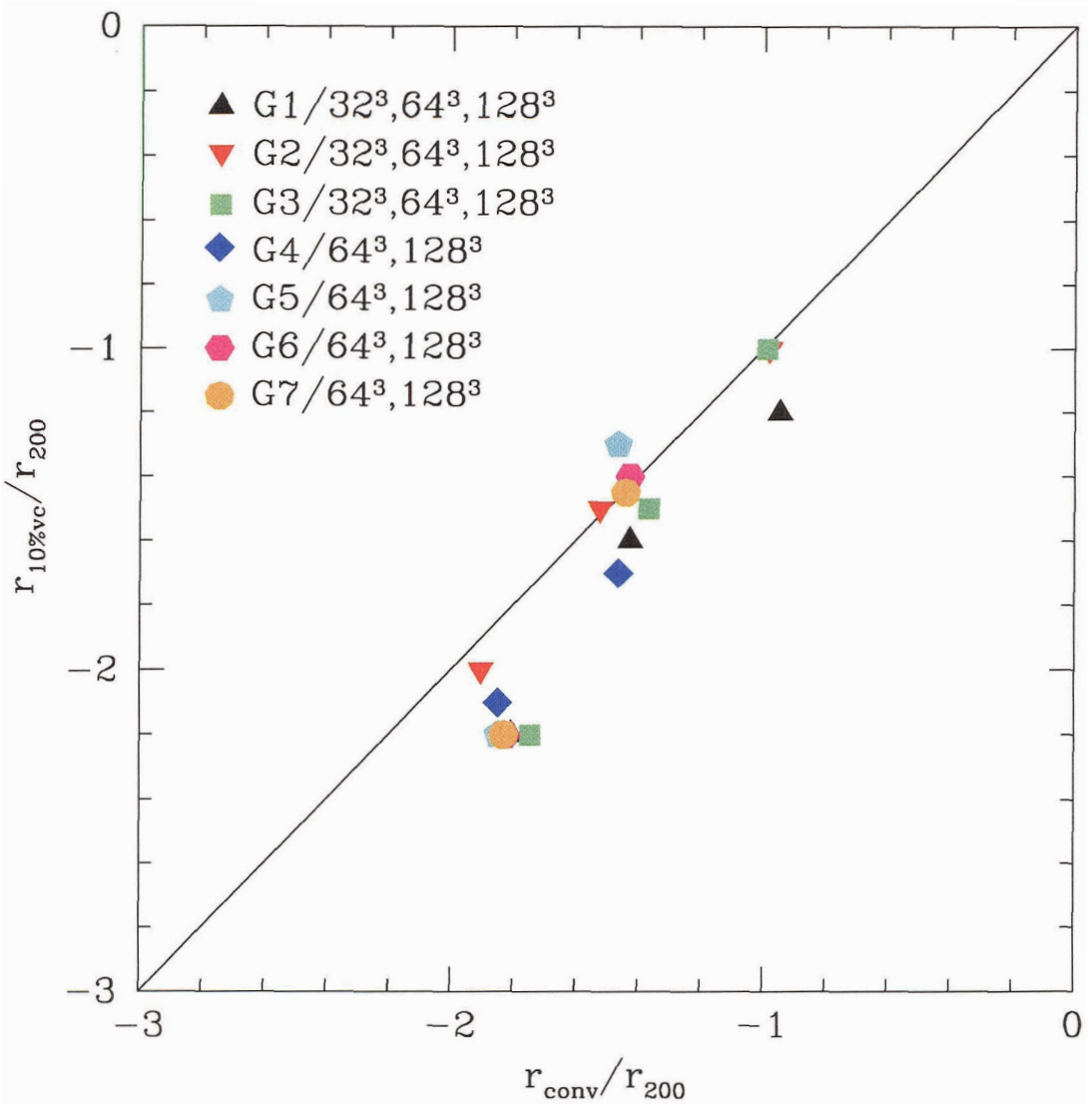

Figure 2.4: Radius where the circular velocity profile of lower resolutions runs starts to deviate from that of the highest resolution run by more than 10%, $r_{10\%vc}$, plotted against the minimum converged radius predicted by the P03 convergence criteria, $r_{\rm conv}$. In all cases $r_{\rm conv} \leq r_{10\%vc}$, validating the P03 criteria as conservative estimators of the converged region.

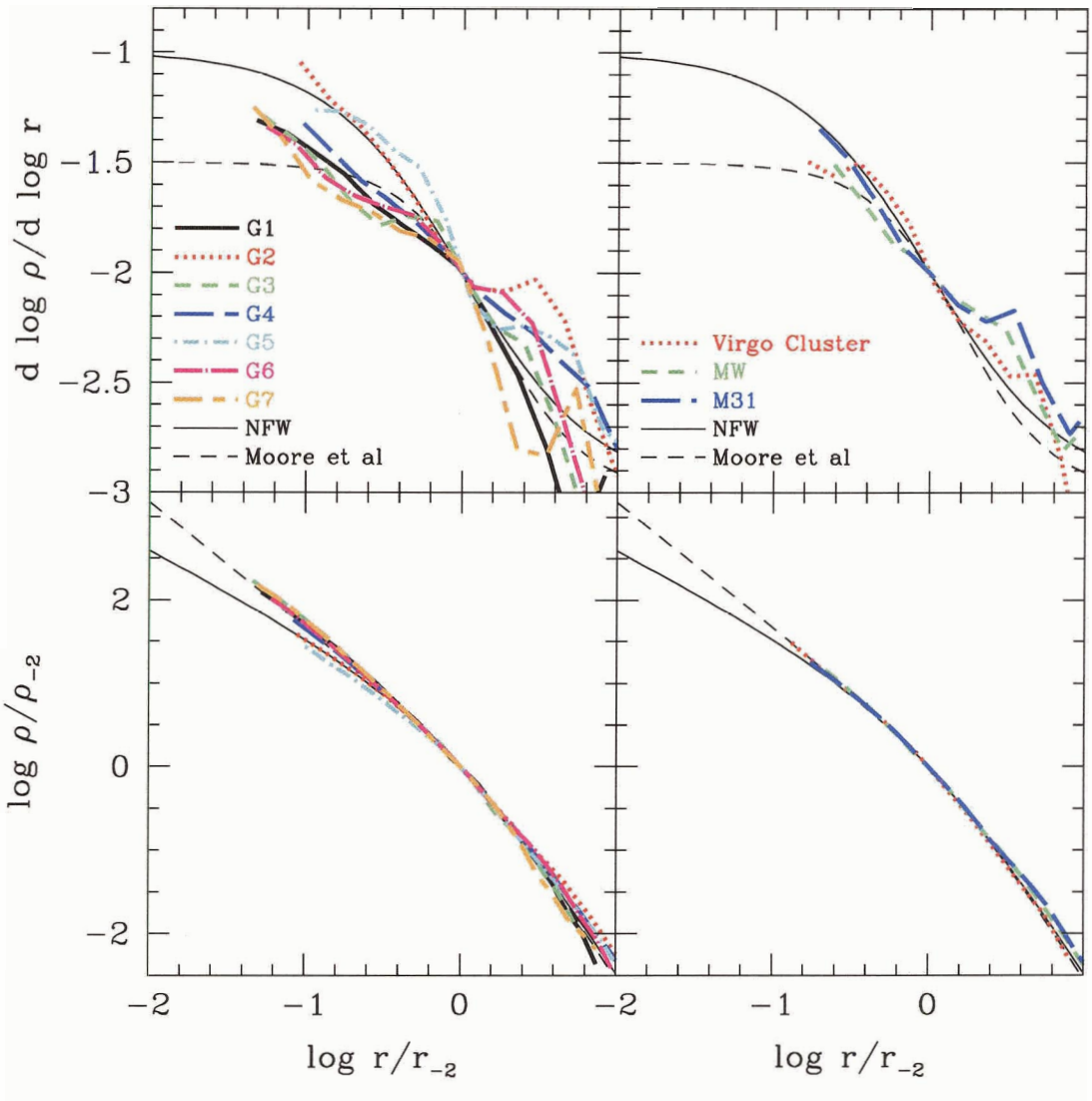

Figure 2.5: *Upper left panel:* Logarithmic slope of the density profile of halos simulated at our highest resolution $N_{\rm sbox} = 256^3$, plotted for $r \geq r_{\rm conv}$. Curves are scaled horizontally to the radius r_{-2}, where the slope takes the isothermal value, $d\log\rho/d\log r(r_{-2}) = -2$. NFW and Moore et al. profiles are shown as solid and dashed curves, respectively. The logarithmic slope increases monotonically with decreasing radius and there is no obvious convergence to a particular asymptotic value of the central slope. *Upper right panel:* Same as upper-left but for the SCDM Virgo cluster of Ghigna et al. (2000) and SCDM Milky Way (MW) and M31 galaxy halos of Moore et al. (1999a). The profiles of the two galaxy-sized halos appear to be consistent with those of our halos, whereas the cluster halo appears to be slightly steeper at the innermost resolved point. *Lower left panel:* Halo density profiles scaled to radius r_{-2}. *Lower right panel:* Same as lower-left but for the Ghigna et al. (2000) and Moore et al. (1999a) halos.

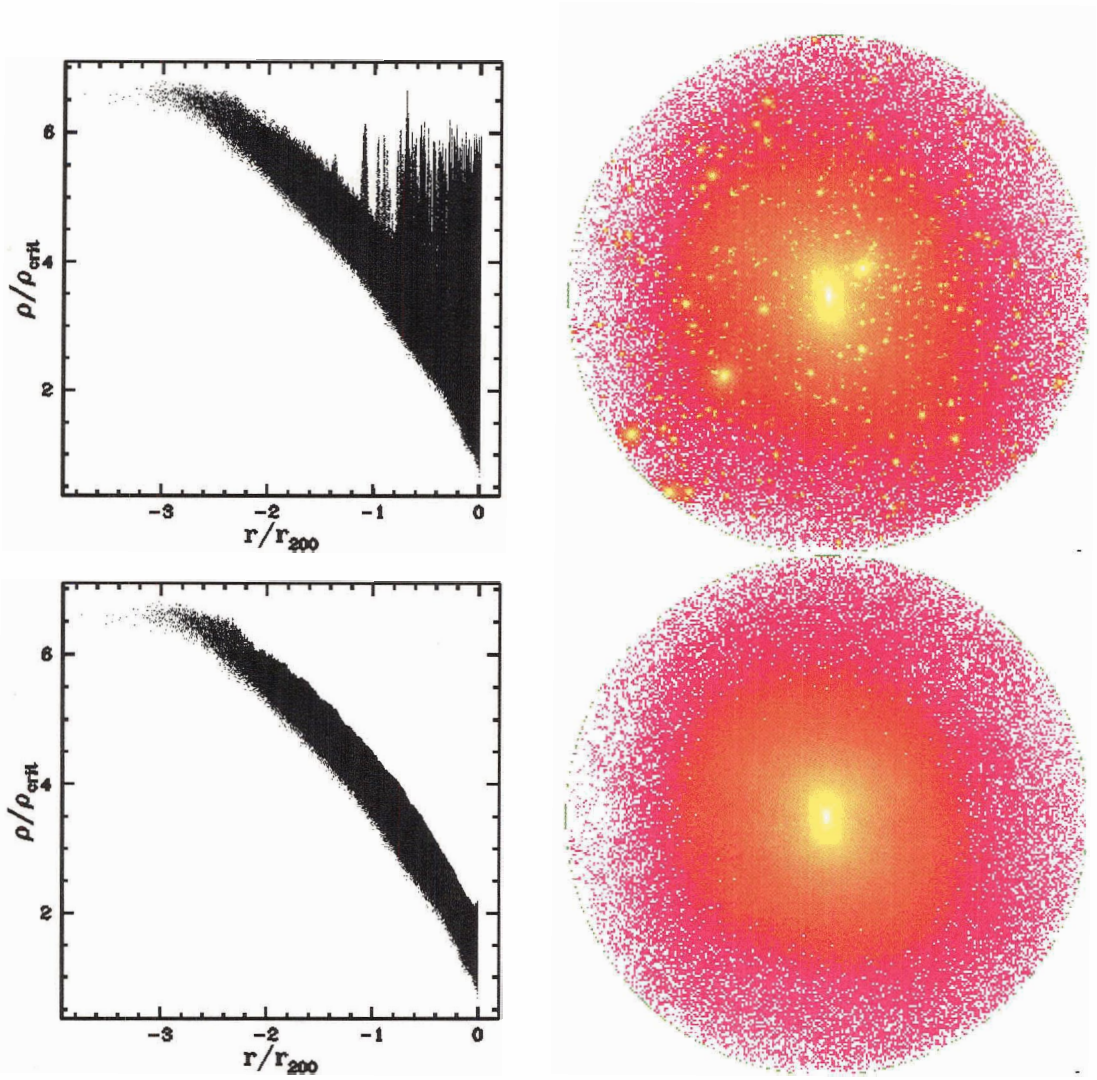

Figure 2.6: *Upper left panel:* Local density of all halo particles from Halo1/256^3 as a function of radius. *Upper right panel:* Snapshot of halo out to $r_{200} = 214.4\ h^{-1}$kpc, with particles colour-coded by local density. *Lower left panel:* Halo particles with local densities less than two standard deviations above the mean local density at that radius. These particles form a smoothly distributed system that appears devoid of substructure on all scales. *Lower right panel:* Snapshot of halo after removal of substructure.

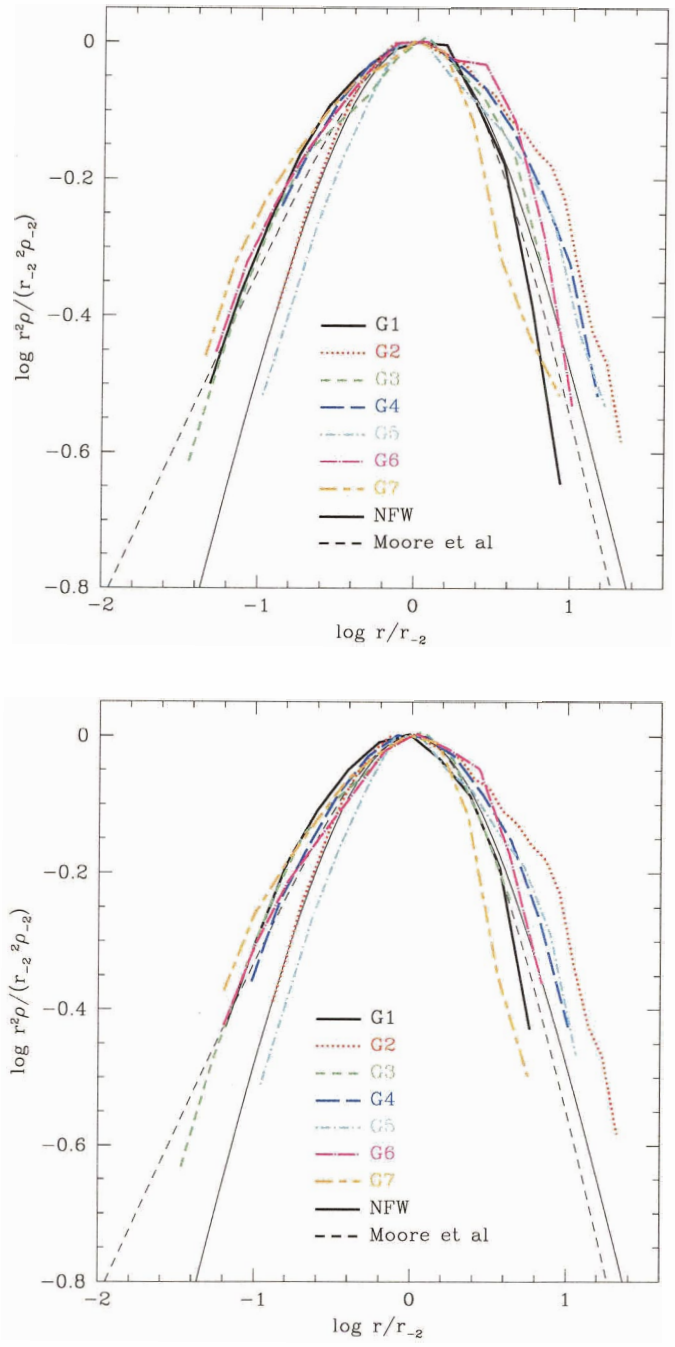

Figure 2.7: *Top panel:* Halo density profiles plotted as $r^2\rho(r)$ in order to expand dynamic range. Profiles are scaled to the same radius r_{-2} as in Figure 2.5. NFW and Moore et al. profiles are shown as thin solid and dashed lines, respectively. *Bottom panel:* Density profiles of halos after removal of substructure. Some irregular features in the profiles are diminished, but most of the overall variation in profile shapes remains.

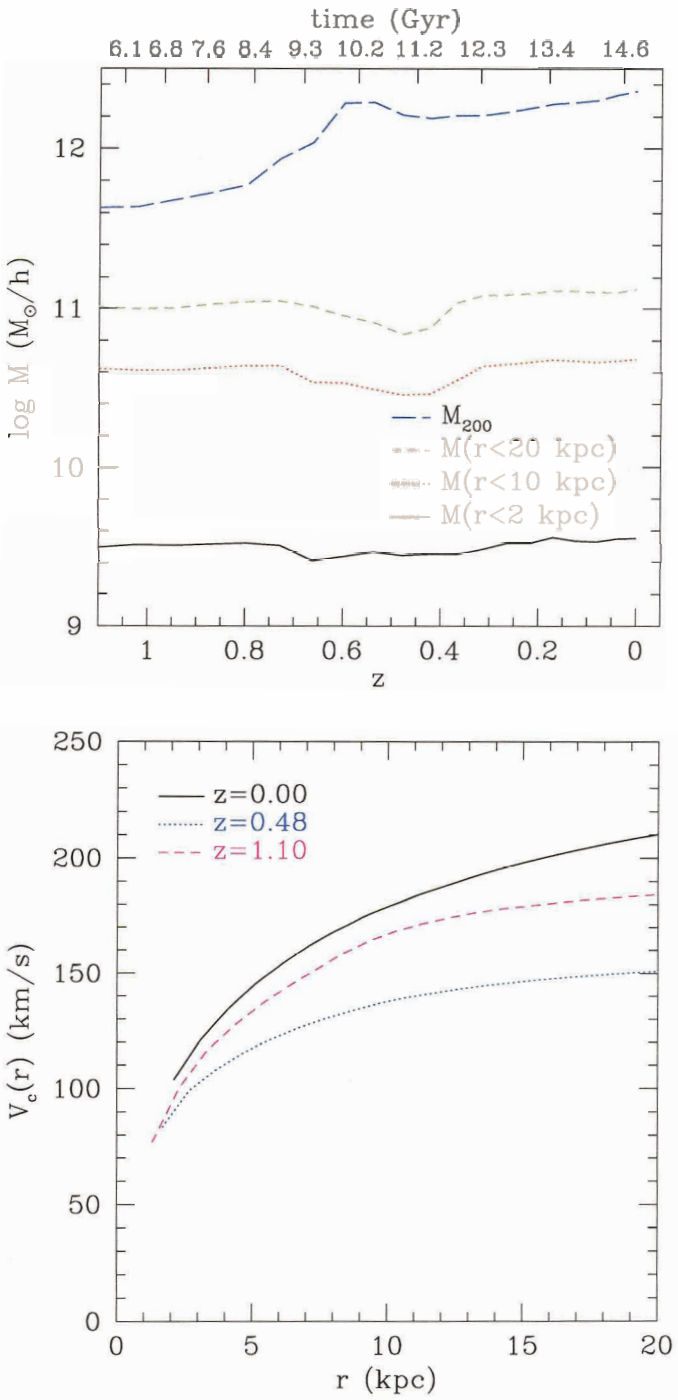

Figure 2.8: *Top panel:* Mass within $r = 2$, 10, and 20 kpc (physical) and r_{200} for halo G1/256^3 as a function of redshift (age of Universe in Gyr) on bottom (top) axis. The mass within 20 h^{-1}kpc undergoes significant fluctuations in response to a merger at $z \simeq 0.7$. *Bottom panel:* The inner circular velocity profile before ($z = 1.10$), during ($z = 0.48$), and after ($z = 0$) the merger. The shape of the V_c profile is noticeably altered by the effects of the infalling substructure.

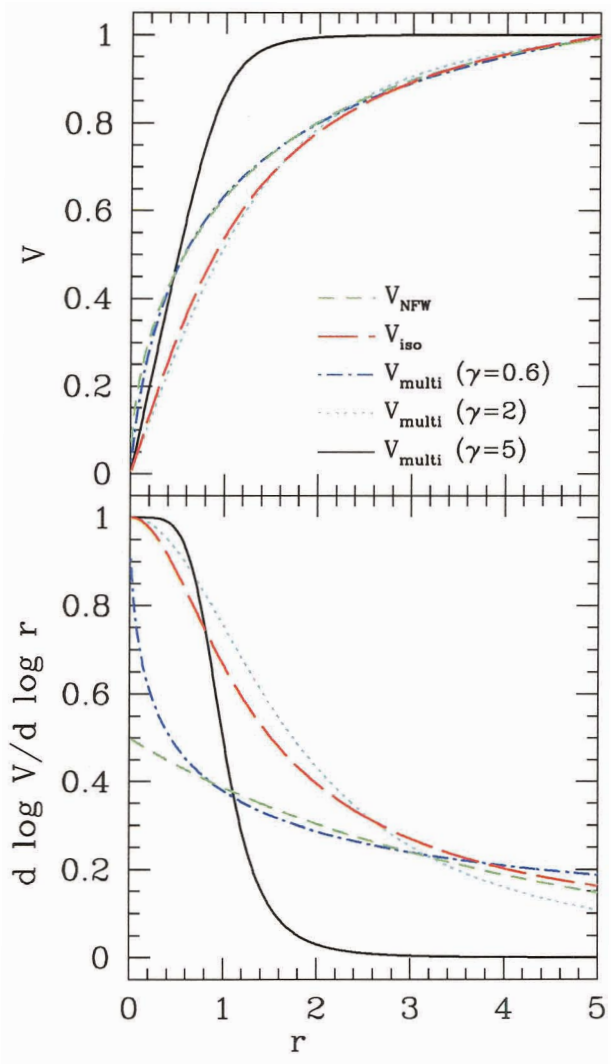

Figure 2.9: *Top panel:* Circular velocity profiles of NFW and pseudo-isothermal halo models along with the Courteau (1997) multi-parameter fitting formula given by eq. 2.8, plotted in arbitrary units of radius and velocity. The NFW profile has $(r_s, V_{\rm max}) = (5.0, 1.0)$, the pseudo-isothermal profile has $(r_c, V_\infty) = (1.0, 1.2)$, and the multi-parameter formula is shown for three different sets of parameters, $(r_t, \gamma, V_0) = (0.44, 0.6, 1.4)$, $(1.8, 2.0, 1.0)$, $(1.0, 5.0, 1.0)$. *Bottom panel:* Logarithmic slope of the velocity profiles. Eq. 2.8 provides a good fit to both halo models despite the fact that at small radii, it rises linearly with radius like the pseudo-isothermal velocity profile. Also, curves with $\gamma \lesssim 1$ turn over gently as a function of radius whereas those with $\gamma \gg 1$ rise linearly out to $r \simeq r_t$ then flatten sharply.

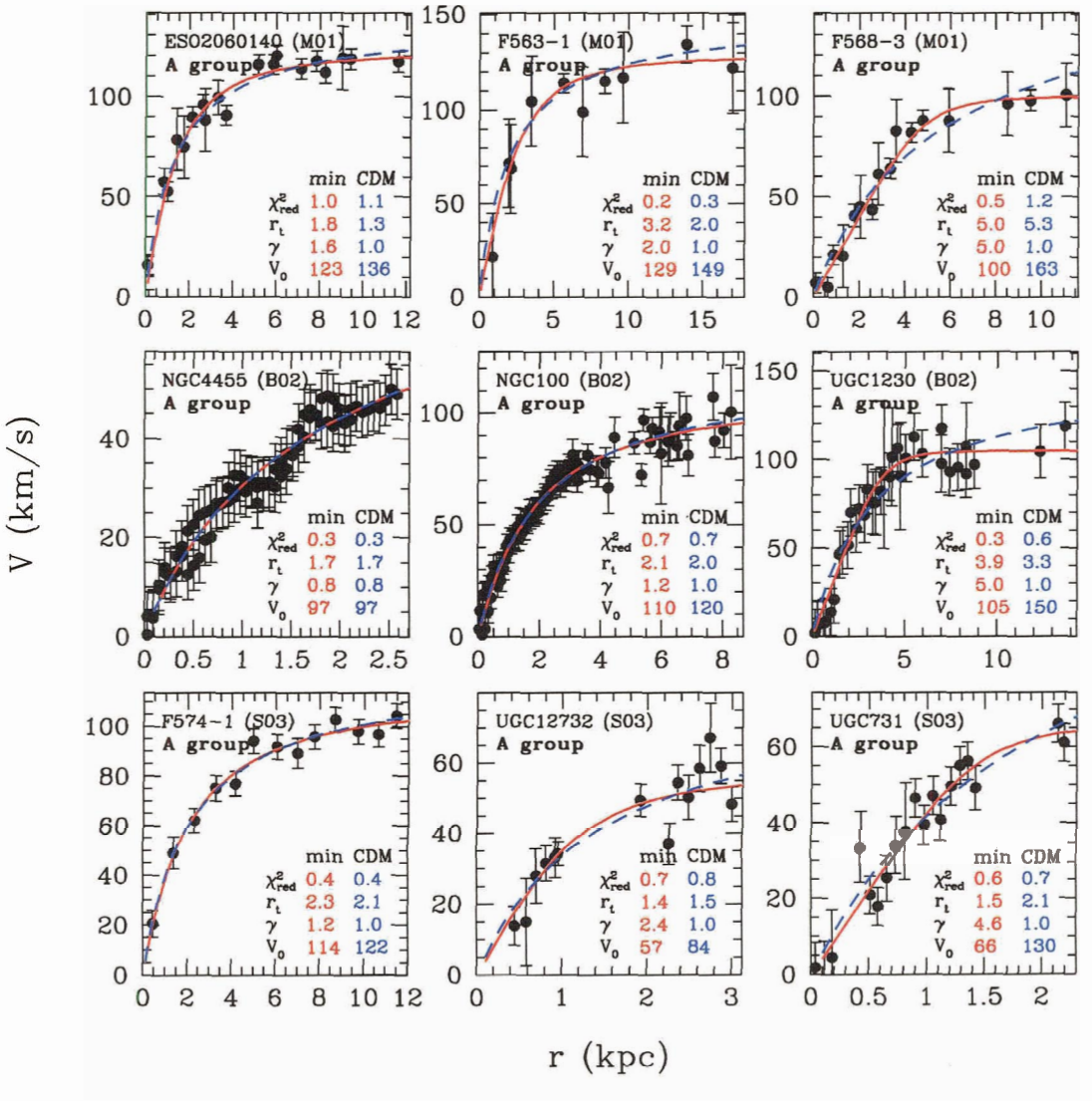

Figure 2.10: Hα rotation curves of LSB galaxies from the datasets of McGaugh et al. (2001) (M01, top row), de Blok and Bosma (2002) (B02, middle row) and Swaters et al. (2003a) (S03, bottom row). Solid curves show best fits using the multi-parameter fitting formula given by eq. 2.8 with fit parameters and $\chi^2_{\rm red}$ values listed under "min" column in each panel. Dashed curves show the best fits which can be obtained with ΛCDM-compatible parameters, listed under "CDM" column. In each row, rotation curves are ordered from left to right in order of increasing best fit γ values. All rotation curves in this figure belong to group A, defined as having ΛCDM-compatible fits with reasonable $\chi^2_{\rm red}$ values ($\chi^2_{\rm red} \leq 1.5$). See text for full discussion.

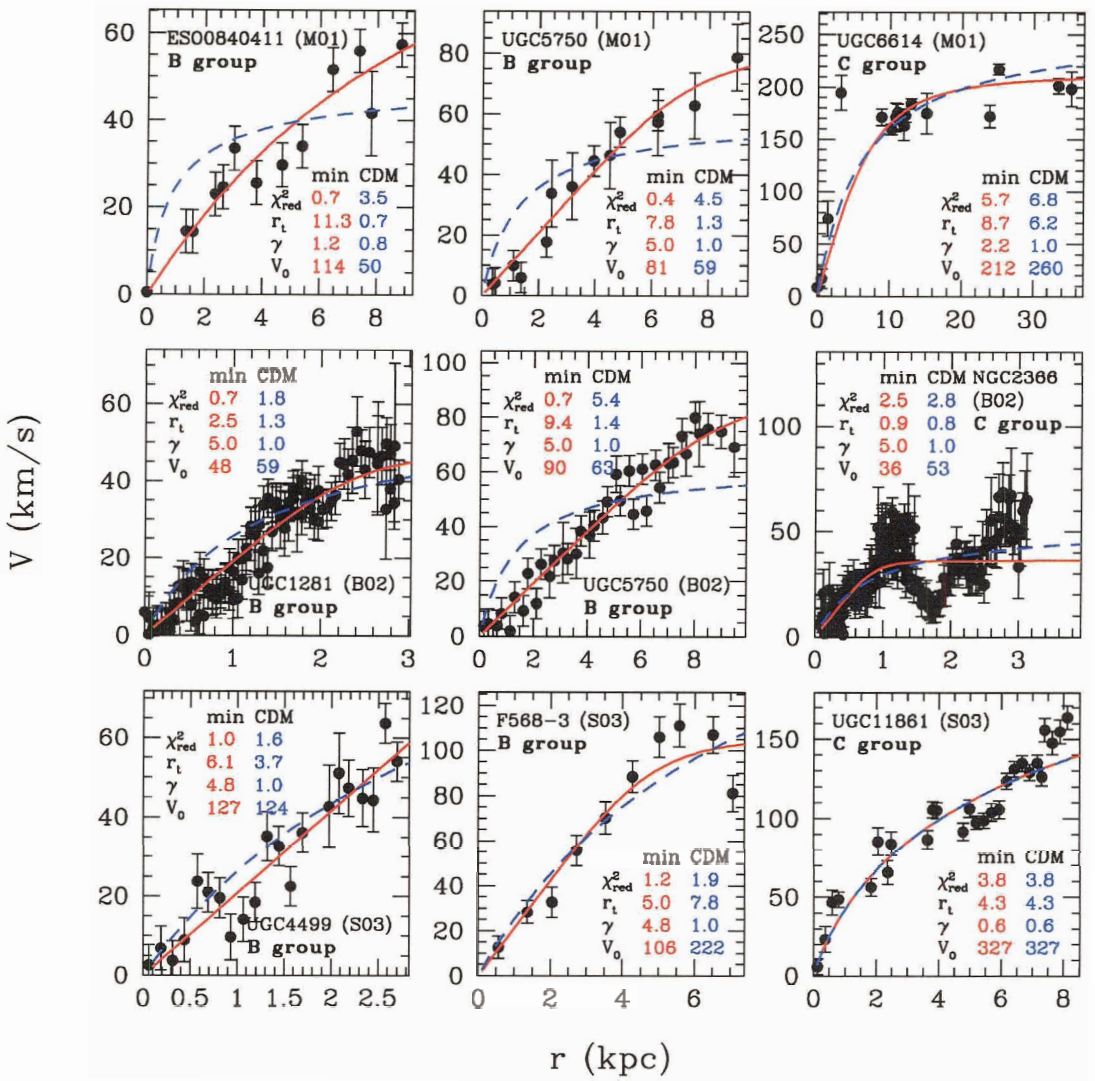

Figure 2.11: Same as Figure 2.11 but featuring all six rotation curves from group B and three from group C. Rotation curves from group B are those for which a good fit with ΛCDM-compatible parameters cannot be found. The best fits for these rotation curves typically have high values of γ, corresponding to a linear rise in velocity with radius and in some cases a sharp transition from the rising to the flat part of the curve. Galaxies in group C have irregular rotation curves for which simple fitting functions like eq. 2.8 cannot provide a good fit. See text for full discussion.

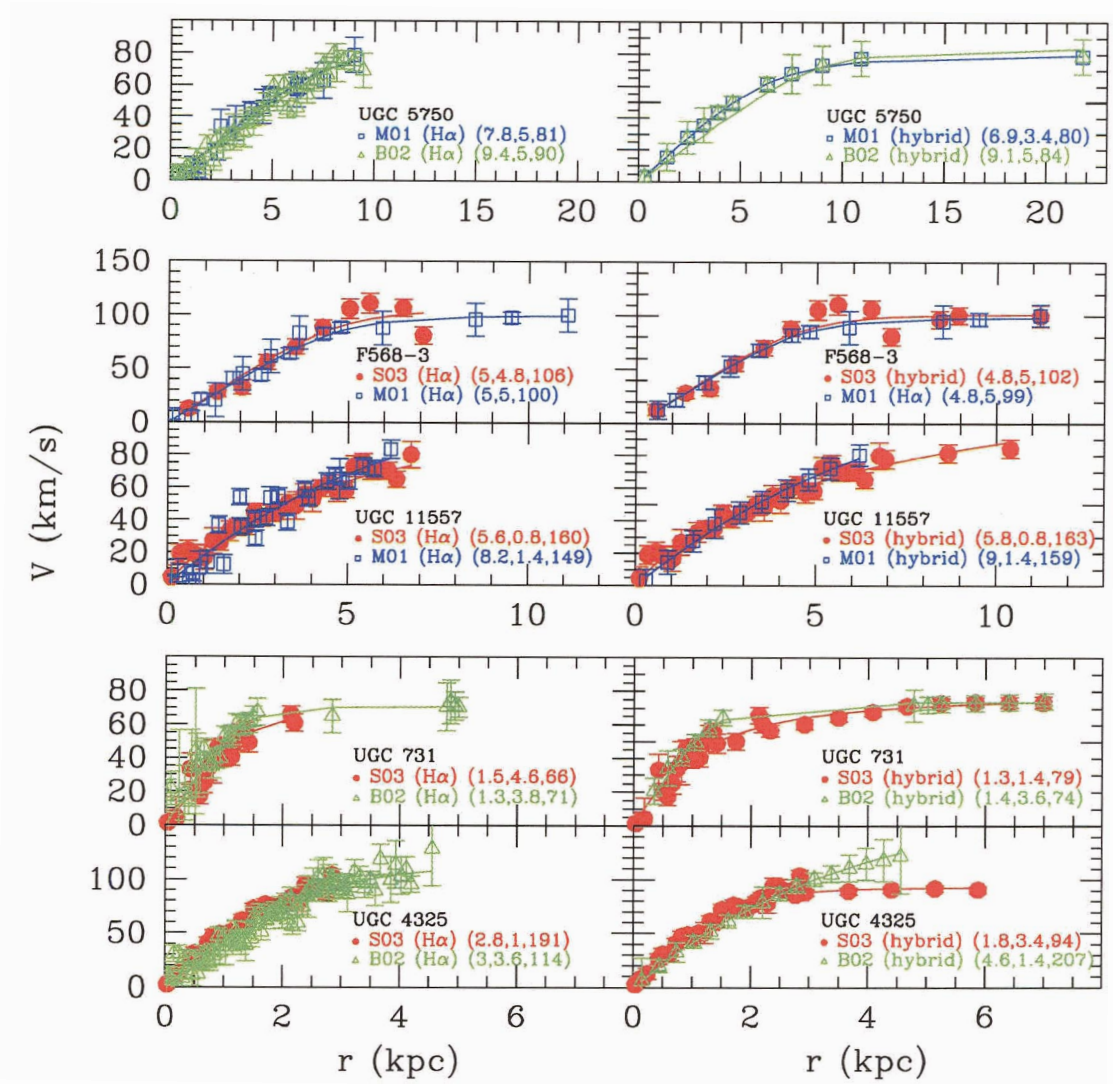

Figure 2.12: Comparison of Hα (left panels) and smoothed hybrid rotation curves (right panels) derived by M01 (open squares), B02 (open triangles), and S03 (filled circles). Solid lines show best fits with eq. 2.8 with parameters listed as (r_t (h^{-1}kpc), γ, V_0 (km s^{-1})). Different versions of the rotation curve data are broadly consistent with one another: in most cases the best fit parameter values are within $\sim 20\%$ of one another.

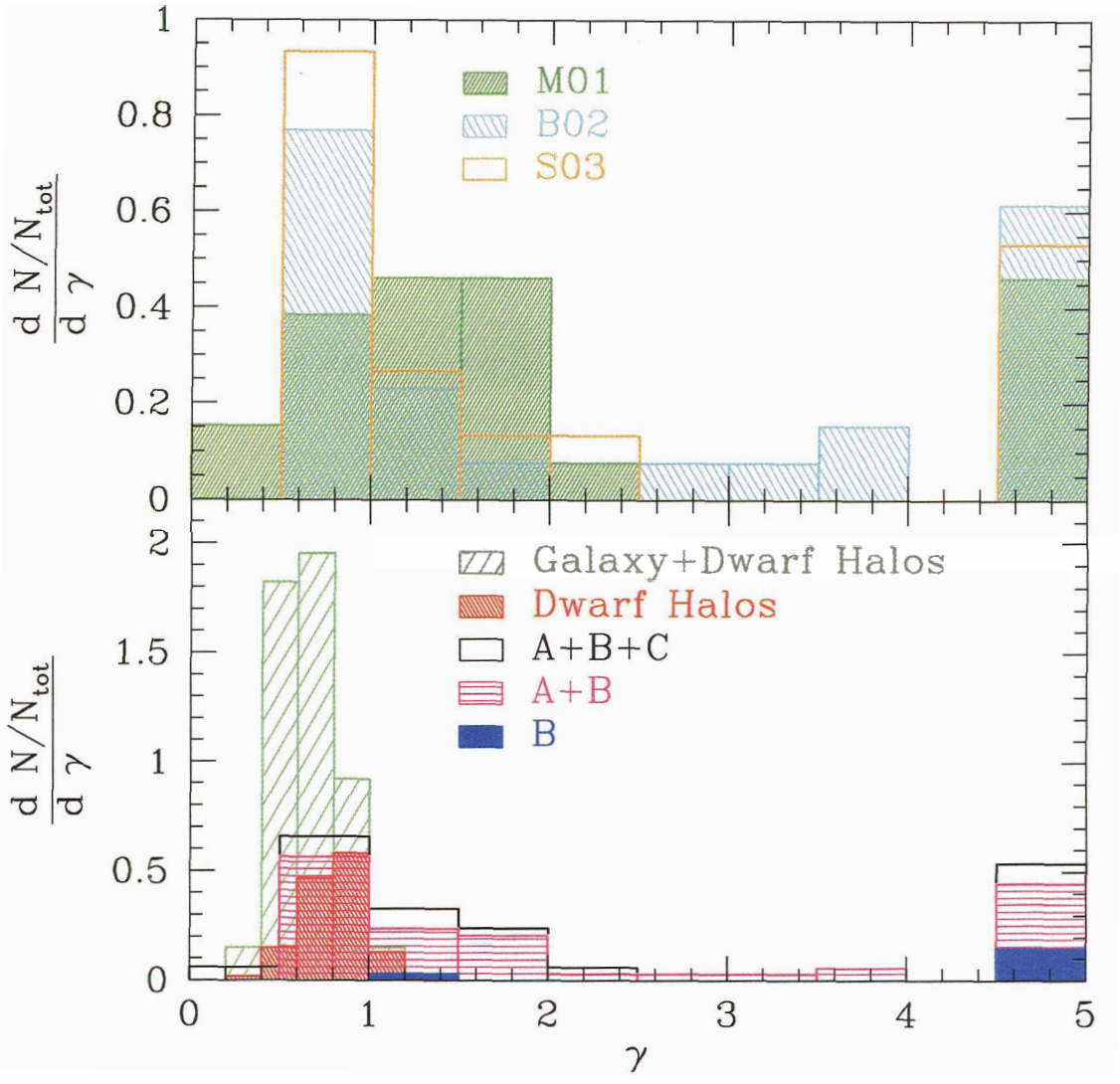

Figure 2.13: *Top panel:* Distribution of best fit γ values obtained for galaxies in the samples of McGaugh et al. (2001) (M01), de Blok and Bosma (2002) (B02), and Swaters et al. (2003a) (S03). All three datasets are roughly consistent with one another and about 70% of the rotation curves in each sample have $\gamma \lesssim 2$. *Bottom panel:* Halo and LSB γ distributions. LSB data are sorted by χ^2 groups, as defined in Figure 2.17. All simulated halos have $\gamma \lesssim 1$, whereas many LSBs have $\gamma > 1$. However, most LSBs are members of group A, shown by the horizontally hatched region of the histogram, and have acceptable fits with $\gamma \leq 1$. Group B members, shown by the solid region of the histogram, have γ values and/or central densities that are inconsistent with those of ΛCDM halos. Group C members, shown by the open region of the histogram, are not well fit by simple functions like eq. 2.8.

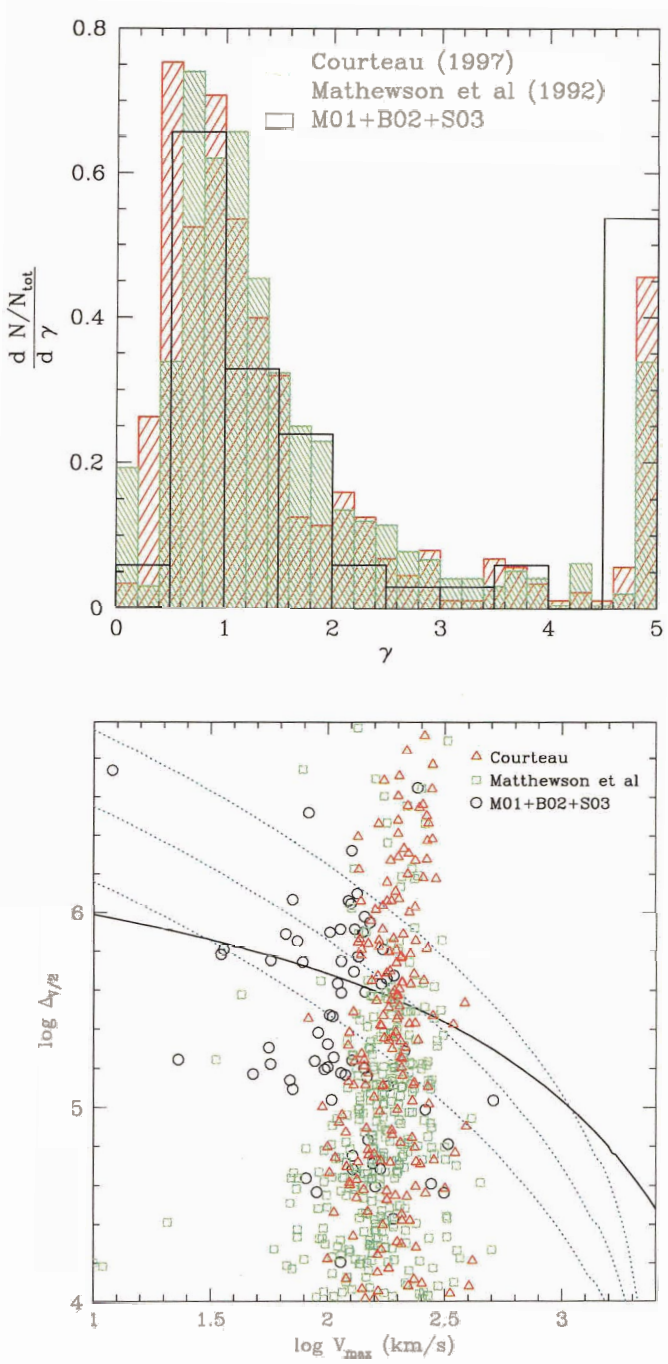

Figure 2.14: *Upper panel:* Distribution of best fit γ values of high surface brightness (HSB) galaxies from the samples of Courteau (1997) and Mathewson et al. (1992) compared with combined LSB sample (M01+B02+S03). The distribution of HSB and LSB galaxies are remarkably similar to one another. *Bottom panel:* Central densities of HSB and LSB galaxies. HSB galaxies exhibit an even larger spread of central densities than LSB galaxies.

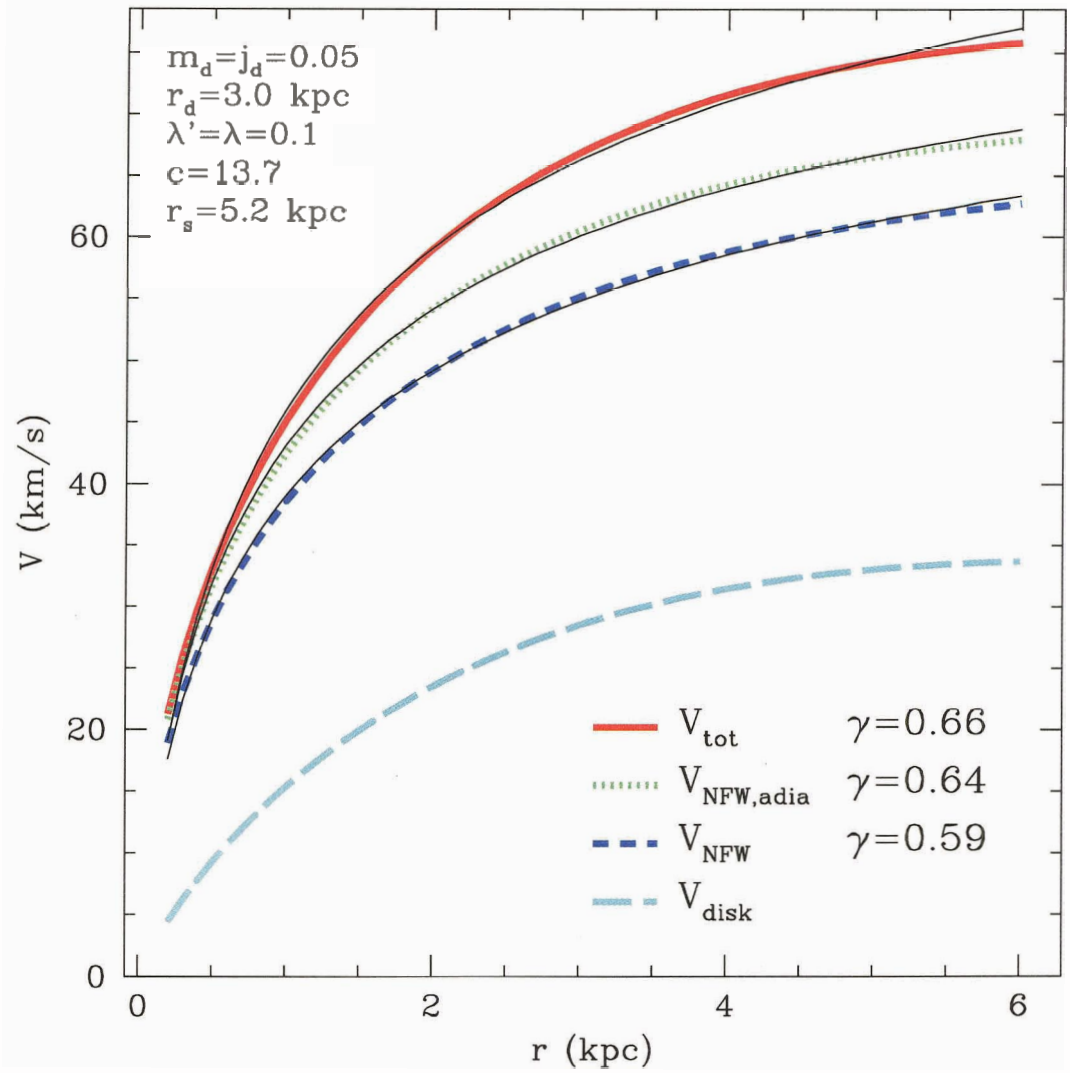

Figure 2.15: Circular velocity profiles of a disk galaxy modelled according to the prescription of Mo et al. (1998). Parameters of the galaxy model are shown at top left, where m_d and j_d are the mass and angular momentum of the disk (in units of the corresponding quantities for the halo), r_d is the exponential scale length of the disk, λ and λ' are the spin parameters of the disk and halo, respectively, r_s is the scale length of the NFW halo, and $c = r_{200}/r_s$ is the halo concentration parameter. Thick lines show the V_c profiles of the disk ($V_{\rm disk}$), the NFW halo ($V_{\rm NFW}$), the halo after adiabatic contraction ($V_{\rm NFW,adia}$), and the total velocity $V_{\rm tot}^2 = V_{\rm disk}^2 + V_{\rm NFW,adia}^2$. Best fits to the V_c profiles with eq. 2.8 are shown as thin solid lines. The addition of an LSB disk results in only a small change in the best fit value of γ, from $\gamma = 0.59$ for the NFW halo to $\gamma = 0.66$ for $V_{\rm tot}$.

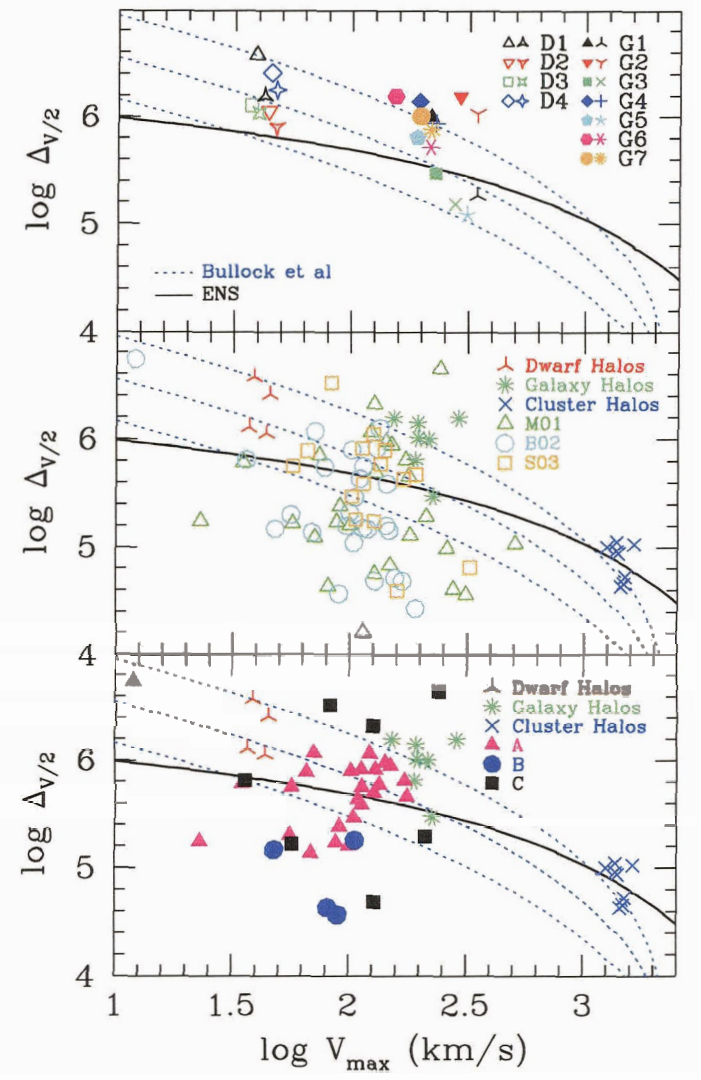

Figure 2.16: *Top panel:* Alam et al. (2002) halo central density parameter, $\Delta_{V/2}$, for simulated dwarf- and galaxy-sized halos versus maximum velocity $V_{\rm max}$. Solid and open symbols show $\Delta_{V/2}$ and $V_{\rm max}$ values measured directly from V_c profiles, skeletal and starred symbols show $\Delta_{V/2}$ and $V_{\rm max}$ values estimated from fits to V_c profiles with eq. 2.8, taking the asymptotic velocity of the fit, V_0, as the estimate of $V_{\rm max}$. Solid line shows the prediction of the Eke et al. (2001) concentration model for NFW halos in a ΛCDM cosmogony. Dotted lines show the prediction (and 1 σ scatter) of the Bullock et al. (2001) concentration model. *Middle panel:* Central densities of simulated dwarf, galaxy, and cluster-sized halos calculated directly from their V_c profiles (skeletal symbols) compared with $\Delta_{V/2}$ and $V_{\rm max}(= V_0)$ values calculated from fits to LSB rotation curves from M01, B02, and S03 datasets (open symbols). *Lower panel:* Same as middle panel, but with LSB $\Delta_{V/2}$ values sorted by χ^2 groups shown in Figure 2.17. Only galaxies with well-defined maximum velocities are shown.

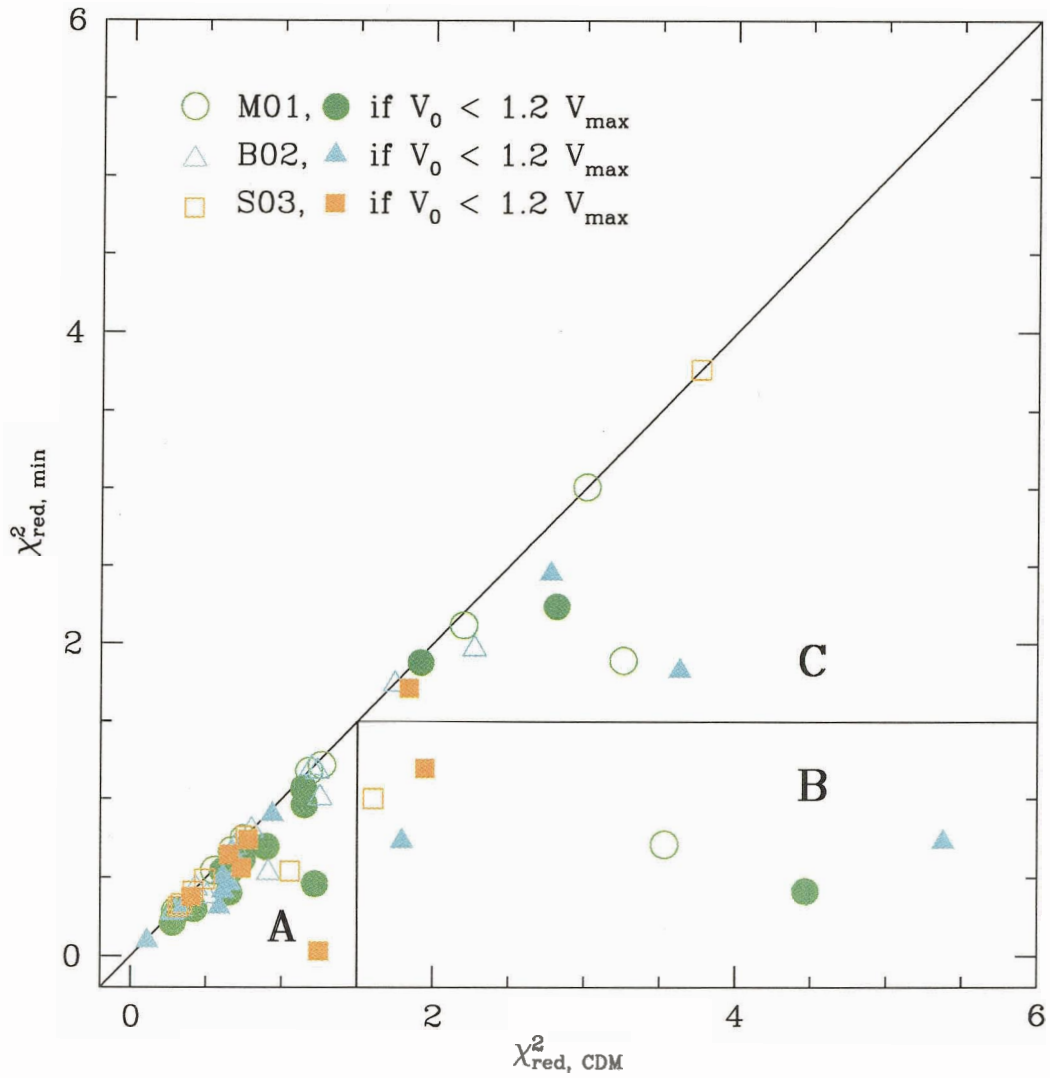

Figure 2.17: Reduced χ^2 values of best fits to rotation curves from M01, B02, and S03 datasets versus χ^2 values of best fits with ΛCDM-compatible parameters. Solid (open) symbols represent rotation curves with best fit values of V_0 within 20% of (more than 20% greater than) their maximum velocities, V_{max}. Data falls into three groups: A) galaxies that are consistent ($\chi^2 < 1.5$) with ΛCDM in terms of the shapes of their rotation curves and their inferred central densities; B) galaxies that are inconsistent with ΛCDM; and C) galaxies with irregular rotation curves for which simple fitting functions like eq. 2.8 do not provide a good fit.

Chapter 3

Universality and Asymptotic Slopes of Halo Density Profiles

Abstract

We investigate the mass profile of ΛCDM halos using a suite of numerical simulations spanning five decades in halo mass, from dwarf galaxies to rich galaxy clusters. These halos typically have a few million particles within the virial radius (r_{200}), allowing robust mass profile estimates down to radii below 1% of r_{200}. Our analysis confirms the proposal of Navarro, Frenk & White (NFW) that the shape of ΛCDM halo mass profiles differs strongly from a power law and depends little on mass. The logarithmic slope of the spherically-averaged density profile, as measured by $\beta = -d\ln\rho/d\ln r$, decreases monotonically towards the center and becomes shallower than isothermal ($\beta < 2$) inside a characteristic radius, r_{-2}. The fitting formula proposed by NFW provides a reasonably good approximation to the density and circular velocity profiles of individual halos; circular velocities typically deviate from best NFW fits by less than 10% over the radial range which is well resolved numerically. On the other hand, systematic deviations from the best NFW fits are also noticeable. Inside r_{-2}, the profile of simulated halos gets shallower with radius more gradually than predicted and, as a result, NFW fits tend to underestimate the dark matter density in these regions. This discrepancy has been interpreted as indicating a steeply divergent cusp with asymptotic inner slope, $\beta_0 \equiv \beta(r = 0) \sim 1.5$. Our results suggest a different interpretation. We use the density and enclosed mass at our innermost resolved radii to place strong constraints on β_0: density cusps as steep as $r^{-1.5}$ are inconsistent with most of our simulations, although $\beta_0 = 1$ is still consistent with our data. Our density profiles show no sign of converging to a well-defined asymptotic inner power law. We propose a simple formula that reproduces the radial dependence of the slope

better than the NFW profile, and so may minimize errors when extrapolating our results inward to radii not yet reliably probed by numerical simulations.

3.1 Introduction

Disk galaxy rotation curves; strong gravitational lensing by galaxies and clusters; the dynamics of stars in elliptical galaxies and of gas and galaxies in clusters; these are just examples of the various luminous tracers that probe the inner structure of dark matter halos. Such observations place strong constraints on the distribution of dark matter in these highly non-linear regions that may be contrasted directly with theoretical predictions for halo structure. Given the sensitivity of such predictions to the nature of the dark matter, these observational constraints constitute tests that may question or even rule out particular models of dark matter.

Robust prediction of the inner structure of cold dark matter (CDM) halos is a quintessential N-body problem, albeit one of considerable complexity due to the large overdensities and, consequently, the short crossing times involved. Indeed, only recently have computational capabilities improved to the point of allowing realistic simulation of the regions which house the luminous components of individual galaxies.

This work builds upon the pioneering efforts of Frenk et al. (1988), Dubinski and Carlberg (1991), and Crone et al. (1994), among others, which led to the identification of a number of key features of the structure of dark matter halos assembled by hierarchical clustering. One important result of this early work concerns the absence of a well defined central "core" of constant density in virialized CDM halos. In this sense, dark matter halos are "cuspy": the dark matter density grows apparently without bounds toward the center of the halo.

A second result concerns the remarkable similarity ("universality") in the structure of dark matter halos of widely different mass. This was first proposed by Navarro,

Frenk & White (1996, 1997; hereafter NFW), who suggested a simple fitting formula to describe the spherically-averaged density profiles of dark matter halos,

$$\rho(r) = \frac{\rho_s}{(r/r_s)(1+(r/r_s))^2}, \tag{3.1}$$

where ρ_s and r_s are a characteristic density and radius, respectively. The larger the mass of a halo, the lower its characteristic density, reflecting the lower density of the universe at the (later) assembly time of more massive systems.

Further simulation work of similar numerical resolution (see, e.g., Cole and Lacey, 1996; Huss et al., 1999) provided support for the NFW conclusions, although small but systematic differences began to emerge as the numerical resolution of the simulations improved (see, e.g., Moore et al 1999, hereafter M99, Ghigna et al 2000, Fukushige & Makino 1997, 2001, 2003). These authors reported deviations from eq. 3.1 that increase systematically inward, and thus are particularly noticeable in high-resolution simulations. In particular, Fukushige and Makino (2001) reported that NFW fits tend to underestimate the dark matter density within the scale radius r_s. M99 reached a similar conclusion and interpreted this result as indicating a density cusp steeper than that of the NFW profile.

These authors preferred a modified fitting function which diverges as $r^{-1.5}$ near the center,

$$\rho(r) = \frac{\rho_M}{(r/r_M)^{1.5}(1+(r/r_M)^{1.5})}. \tag{3.2}$$

One should note, however, that there is no consensus amongst N-body practitioners for such modified profile (see, e.g., Klypin et al 2001 and Power et al 2003, hereafter P03), and that there is some work in the literature suggesting that the central density cusp might actually be *shallower* than r^{-1} (Subramanian et al., 2000a; Taylor and Navarro, 2001; Ricotti, 2003).

This unsettled state of affairs illustrates the difficulties associated with simulating

the innermost structure of CDM halos in a robust and reproducible manner. The high density of dark matter in such regions demands large numbers of particles and fine time resolution, challenging to the limit even the largest supercomputers available at present. As a result, many of the studies mentioned above are either of inadequate resolution to be conclusive or are based on results from a handful of simulations where computational cost precludes a systematic assessment of numerical convergence.

Establishing the detailed properties of the central density cusp, as well as deriving the value of its asymptotic central slope, are important for a number of reasons. For example, steeper cusps place larger amounts of dark matter at the center, exacerbating the disagreement with observations that suggest the presence of a constant density core in low surface brightness galaxies or in strongly barred galaxies (Moore, 1994; Flores and Primack, 1994; McGaugh and de Blok, 1998; Debattista and Sellwood, 1998; van den Bosch et al., 2000). Steep cusps would also be important for direct detection experiments for dark matter, as the gamma-ray annihilation signal of WIMPS at the Galactic center is expected to be particularly strong for $r^{-1.5}$ cusps (Calcáneo-Roldán and Moore, 2000; Taylor and Silk, 2003; Stoehr et al., 2003).

Finally, the detailed structure of the central cusp is not the only focus of contrasting claims in the literature. For example, the "universality" of CDM halo structure has also been criticized by Jing and Suto (2000), who find that the slope of the density profile at a fixed fraction of the virial radius steepens towards lower halo masses. Klypin et al. (2001), on the other hand, point out that such a systematic trend is entirely consistent with universality as originally claimed by NFW, and just reflects the mass dependence of halo characteristic density.

We address these conflicting issues here using a suite of nineteen high-resolution simulations of the formation of halos in the "concordance" ΛCDM cosmogony. Halo masses are chosen in three main groups; "dwarf" halos with $M_{200} \sim 5 \times 10^9\, h^{-1}\, M_\odot$, "galaxy" halos with $M_{200} \sim 10^{12}\, h^{-1}\, M_\odot$ and "cluster" halos of mass $M_{200} \sim 10^{15}\, h^{-1}\, M_\odot$. This allows us to gain insight into the effects of cosmic variance at each mass scale,

as well as to explore the mass dependence of the structure of ΛCDM halos. We define the mass of a halo to be that contained within its virial radius, that is, within a sphere of mean density contrast 200[1].

This paper is organized as follows. Section 3.2 describes briefly the numerical simulations; § 3.3 discusses our main results; and we summarize our conclusions in § 3.4.

3.2 Numerical Experiments

The numerical set up of our simulations follows closely the procedure described by P03, where the interested reader may find a thorough discussion of our initial conditions generating scheme; the choice of N-body codes and integrators; as well as the criteria adopted to optimize the choice of the numerical parameters of the simulations. For completeness, we include here a brief discussion of the main numerical issues, but refer the reader to P03 for a more detailed discussion.

3.2.1 N-body codes

The simulations reported in this paper have been performed using two parallel N-body codes: `GADGET`, written by Volker Springel (Springel et al., 2001), and `PKDGRAV`, written by Joachim Stadel and Thomas Quinn (Stadel, 2001). As discussed in P03, both codes give approximately the same results for appropriate choices of numerical parameters, and neither code seems obviously to outperform the other when similar numerical convergence criteria are met.

[1]We use the term 'density contrast' to denote densities expressed in units of the critical density for closure, $\rho_{\rm crit} = 3H^2/8\pi G$. We express the present value of Hubble's constant as $H(z = 0) = H_0 = 100\,h$ km s^{-1} Mpc^{-1}

3.2.2 Cosmological Model

We adopt a flat, $\Omega_0 = 0.3$ ΛCDM cosmological model whose dynamics is dominated at present by a cosmological constant, $\Omega_\Lambda = 0.7$. The matter power spectrum is normalized so that the present linear rms amplitude of mass fluctuations in spheres of radius $8\,h^{-1}$ Mpc is $\sigma_8 = 0.9$. We assume a linear fluctuation power spectrum given by the product of the square of the appropriate CDM transfer function, $T^2(k)$, and a Harrison-Zel'dovich primordial power spectrum (i.e. $P(k) \propto k$).

3.2.3 Parent Simulations

The halo samples were drawn from three different ΛCDM cosmological "parent" simulations. Table 3.1 lists the main numerical parameters of each of these simulations. The dwarf, cluster, and most of the galaxy halos were extracted from the simulations ΛCDM-512 (Yoshida et al., 2001) and SGIF-128. These two parent simulations, both carried out within the Virgo Consortium, used the CDM transfer function given by CMBFAST (Seljak and Zaldarriaga, 1996), assuming $h = 0.7$ and $\Omega_b = 0.04$. This transfer function is well fit by the Bardeen et al. (1986) fitting formula with a value of 0.17 for the shape parameter Γ. Three of the galaxy halos (G1-G3, see Table 3.2) were extracted from the parent simulation described by (Eke et al., 2001, labeled ENS01 in Table 3.1). That run used the Bardeen et al. (1986) fitting formula for the CDM transfer function, with $h = 0.65$ and $\Gamma = 0.2$.

3.2.4 Initial Conditions

Since completing the numerical convergence tests reported in P03, we have developed a more flexible and powerful set of codes for setting up the resimulation initial conditions. This resimulation software enables us to iterate the procedure in order to "resimulate a resimulation," an important step for setting up appropriate initial conditions for dwarf halos. The basic methodology employed is very similar to the

methods described in P03, with just a few minor differences. Galaxy halos G1-G3 were selected from the ENS01 simulation and their initial conditions were created using the software described in P03. All of the other halos were set up with the new codes, following the procedure we describe below.

The first stage is to run, up to the redshift of interest (typically $z = 0$), a "parent" simulation of a large, representative volume of a ΛCDM universe. These parent simulations are used to select halos targeted for resimulation at higher resolution. Once a halo has been selected for resimulation at $z = 0$, we trace all particles within a sphere of radius $\sim 3\,r_{200}$ to the $z = \infty$ "unperturbed" configuration. We then create a set of initial conditions with much higher mass resolution in the volume occupied by the halo particles, and resample the remainder of the periodic box at lower resolution, taking care to retain sufficient resolution in the surrounding regions so that external tidal forces acting on the high-resolution region are adequately represented.

The procedure involves two main steps. Firstly, we set up a uniform multi-mass distribution of particles to approximate the particle positions in the high-resolution region at $z = \infty$. This is accomplished by arranging particles either in a cubic grid or as a "glass" distribution, within a cube just big enough to contain the region of interest. Either choice approximates a uniform mass distribution very accurately. Outside the cube we lay down particles on a set of concentric cubic shells, centered on the cube, which extend outwards until they fill the entire periodic volume of the parent simulation. These concentric shells are filled with more massive particles whose interparticle separation increases approximately linearly with distance from the high resolution region. Unlike the grid or glass distributions, this distribution does not reproduce a perfectly uniform mass distribution. However, by populating each shell with regularly spaced particles one obtains a configuration which is uniform enough for our purposes.

In the interest of efficiency, we replace those particles in the high-resolution cube that do not end up in the selected halo with more massive particles made by combining

several high-resolution ones. This procedure, particularly for the dwarf halo resimulations, significantly reduces the number of particles in the initial conditions and the run time of the subsequent simulation. Thus, each halo forms from an "amoeba-shaped" region consisting only of the highest resolution particles in the hierarchy. We have explicitly checked that the resampling procedure adds no extra power; in tests the multi-mass particle distribution remains very close to uniform over an expansion factor of up to ~ 50.

Once a multi-mass but uniform mass distribution has been created, the next step is to to add the appropriate Gaussian density fluctuations. This is done by assigning a displacement and a peculiar velocity to each particle using Fourier methods. By using the same amplitude and phase for every Fourier mode present in the parent simulation, a perturbed density field essentially identical to that of the parent simulation can be reproduced. In the high-resolution cube, because the particle mass is smaller than the parent simulation, it is necessary to add additional short wavelength modes (with amplitudes fixed by the adopted power spectrum) down to the Nyquist wavelength of the new particle grid. To ensure that the Fourier transforms needed to add this extra power are of a manageable size, we make the additional power periodic on the scale of the central cube rather than the scale of the parent simulation. The longest wavelength added is typically smaller than one tenth of the side length of the cube. As described in P03, the individual components of the displacement field are generated in turn, and the displacements calculated at the particle positions by trilinear interpolation. To set up growing modes, we use the Zel'dovich approximation and make the peculiar velocities proportional to the displacements.

The initial redshift (z_i) of each resimulation is chosen so that density fluctuations in the high-resolution region are in the linear regime. P03 find that convergent results are obtained when z_i is high enough so that the (theoretical) rms mass fluctuation on the smallest resolved mass scale, $\sigma(m_p, z_i)$ does not exceed ~ 0.3 (m_p is the mass of one high-resolution particle). All of our simulations satisfy this criterion.

3.2.5 Halo selection

The resimulated halos analyzed in this paper were all identified in the parent simulations by using the friends-of-friends (FoF) group finding algorithm Davis et al. (1985) with a linking length $l = 0.164$. Cluster-sized halos were drawn from a $479\,h^{-1}$ Mpc simulation volume. The FoF(0.164) groups were first ordered by mass and then ten consecutive entries on the list centered around a mass of $10^{15}\,h^{-1}\,M_{\odot}$ were selected. Galaxy halos were likewise drawn from a $35.325\,h^{-1}$ Mpc volume, with the exception of three of the halos (G1-G3) which were selected from a $32.5\,h^{-1}$ Mpc volume.

Target dwarf halos were also found in the SGIF-128 simulation. However, because of their extremely low mass (corresponding to 5-6 particles in SGIF-128), it was necessary to create a second "parent" simulation for them by resimulating a region of the SGIF-128 simulation at significantly higher resolution. To this end, a spherical region of radius $4.4\,h^{-1}$ Mpc, with mean density close to the universal average, was selected at random within the $35.325\,h^{-1}$ Mpc box. This spherical region was then resimulated with roughly one hundred times more particles than in SGIF-128. The target dwarf halos were identified within this spherical volume again from an FoF(0.2) group list. A total of eighteen halos with 450-550 particles (masses $9\text{-}11 \times 10^{9}\,h^{-1}\,M_{\odot}$ were chosen. We report results on the four halos in this list that have been resimulated to date. High resolution initial conditions for these dwarf halos were created in an identical way to the more massive galaxy and cluster halos.

Numerical parameters were chosen to ensure that all halos, regardless of mass, were resimulated at comparable mass resolution (typically over 10^{6} particles within the virial radius at $z = 0$, see Table 3.2). Snapshots of all dwarf, galaxy, and cluster halos at $z = 0$ are shown in Figures 3.1, 3.2, and 3.3, respectively.

3.2.6 The Analysis

We focus our analysis on the spherically-averaged mass profile of simulated halos at $z = 0$. This is measured by sorting particles in distance from the center of each halo and arranging them in bins of equal logarithmic width in radius. Density profiles, $\rho(r)$, are computed simply by dividing the mass in each bin by its volume. The cumulative mass within each bin, $M(r)$, is then used to compute the circular velocity profile of each halo, $V_c(r) = \sqrt{GM(r)/r}$, as well as the cumulative density profile, $\bar{\rho}(r) = 3\,M(r)/4\pi r^3$, which we shall use in our analysis.

The center of each halo is determined using an iterative technique in which the center of mass of particles within a shrinking sphere is computed recursively until a few thousand particles are left (see P03 for details). In a multi-component system, such as a dark halo with substructure, this centering procedure isolates the densest region within the largest subcomponent. In more regular systems, the center so obtained is in good agreement with centers obtained by weighing the center of mass by the local density or by the gravitational potential of each particle.

We note that, unlike NFW, no attempt has been made to select halos at a particularly quiet stage in their dynamical evolution; our sample thus contains halos in equilibrium as well as a few with prominent substructure as a result of recent accretion events.

3.2.7 Parameter selection criteria

The analysis presented in P03 demonstrated that the mass profile of a simulated halo is numerically robust down to a "convergence radius," $r_{\rm conv}$, that depends primarily on the number of particles and time steps, as well as on the choice of gravitational softening of the simulation. Each of these choices imposes a minimum radius for convergence, although for an "optimal" choice of parameters—i.e., one that, for given $r_{\rm conv}$, minimizes the number of required force computations and time steps—the

most stringent criterion is that imposed by the number of particles within r_{200}. In this optimal case, the minimum resolved radius is well approximated by the location at which the two-body relaxation time, $t_{\rm relax}$, equals the age of the universe (see Hayashi et al., 2003, for further validation of these criteria).

To be precise, we shall identify $r_{\rm conv}$ with the radius where $t_{\rm relax}$ equals the circular orbital timescale at the virial radius, $t_{\rm circ}(r_{200}) = 2\pi\, r_{200}/V_{200}$. Thus $r_{\rm conv}$ is defined by the following equation,

$$\frac{t_{\rm relax}(r)}{t_{\rm circ}(r_{200})} = \frac{N}{8\,\ln N}\frac{r/V_c}{r_{200}/V_{200}} = 1. \tag{3.3}$$

Here $N = N(r)$ is the number of particles enclosed within r, and $V_{200} = V_c(r_{200})$. With this definition, the convergence radius in our best-resolved halos, outside which $V_c(r)$ converges to better than 10%, is of order $\sim 0.005\, r_{200}$.

3.3 Results

3.3.1 Density Profiles

The top panels of Figure 3.4 show the density profiles, $\rho(r)$, of the nineteen simulated halos in our sample. In physical units, the profiles split naturally into three groups: from left to right, "dwarf" (dotted), "galaxy" (dashed), and "cluster" (dot-dashed) halos, respectively. Each profile is shown from the virial radius, r_{200}, down to the innermost converged radius, $r_{\rm conv}$; a convention that we shall adopt in all figures throughout this paper.

The thick solid lines in the top-left panel show the NFW profiles (eq. 3.1) expected for halos in each group, with parameters chosen according to the prescription of Eke et al. (2001). Note that these NFW curves are *not* best fits to any of the simulations, but that they still capture reasonably well the shape and normalization of the density

profiles of the simulated halos.

The top right panel of Figure 3.4 is similar to the top left one, but the comparison is made here with the modified form of the NFW profile proposed by M99 (eq. 3.2). There is no published prescription specifying how to compute the numerical parameters of this formula for halos of given mass, so the three profiles shown in this panel are just "eyeball" fits to the most massive halo in each group. Like the NFW profile, the M99 formula also appears to describe reasonably well the gently-curving density profiles of ΛCDM halos.

Figure 3.4 thus confirms a number of important trends that were already evident in prior simulation work.

- ΛCDM halo density profiles deviate significantly from simple power laws, and steepen systematically from the center outwards; they are shallower than isothermal near the center and steeper than isothermal near the virial radius.

- There is no indication of a well defined central "core" of constant density; the dark matter density keeps increasing all the way in, down to the innermost resolved radius.

- Simple formulae such as the NFW profile (eq. 3.1) or the M99 formula (eq. 3.2) appear to describe the mass profile of all halos reasonably well, irrespective of mass, signaling a "universal" profile shape. Properly scaled, a dwarf galaxy halo is almost indistinguishable from a galaxy cluster halo.

We elaborate further on each of these conclusions in what follows.

NFW vs M99 fits

Are the density profiles of ΛCDM halos described better by the NFW formula (eq. 3.1) or by the modification proposed by M99 (eq. 3.2)? The answer may be seen in the bottom panels of Figure 3.4. These panels show the deviations (simulation

minus fit) from the *best* fits to the density profiles of each halo using the NFW profile or the M99 profile. These fits are obtained by straightforward χ^2 minimization, assigning equal weight to each radial bin. This is done because the statistical (Poisson) uncertainty in the determination of the density within each bin is negligible (each bin contains from several thousand to several hundred thousand particles) so uncertainties are completely dominated by systematic errors whose radial dependence is difficult to assess quantitatively.

As shown in the bottom panels of Figure 3.4, there is significant variation in the shape of the density profile from one halo to another. Some systems are fit better by eq. 3.1 than by eq. 3.2, and the reverse is true in other cases. Over the radial range resolved by the simulations, $\rho(r)$ deviates from the best fits typically by less than 50%. NFW fits tend to *underestimate* the density in the inner regions of most halos; by up to 40% at the innermost resolved point. M99 fits, on the other hand, seem to do better for low mass halos, but tend to *overestimate* the density in the inner regions of cluster halos by up to 60%.

This level of accuracy may suffice for a number of observational applications, with the proviso that comparisons are restricted to radii where numerical simulations are reliable; i.e., $r_{\rm conv} < r < r_{200}$. Deviations from the best fits increase systematically towards the center, so it is likely that extrapolations of either fitting formula to radii inside $r_{\rm conv}$ will incur substantial error. We discuss below (§ 3.3.6) possible modifications to the fitting formulae that may minimize the error introduced by these extrapolations.

3.3.2 Circular Velocity Profiles

Many observations, such as disk galaxy rotation curves or strong gravitational lensing, are better probes of the *cumulative* mass distribution than of the differential density profile shown in Figure 3.4. Since cumulative profiles are subject to different

uncertainties than differential ones, it is important to verify that our conclusions regarding the suitability of the NFW or M99 fitting formulae are also applicable to the cumulative mass distribution of ΛCDM halos.

The radial dependence of the spherically-averaged circular velocity profile of all halos in our series is shown in Figure 3.5. As in Figure 3.4, the thick solid curves in the top left (right) panel are meant to illustrate a typical NFW (M99) profile corresponding to dwarf, galaxy, and cluster halos, respectively. The bottom left and right panels show deviations from the *best* fit to each halo using the NFW or M99 profile, respectively. Both profiles do reasonably well at reproducing the cumulative mass profile of the simulated halos. The largest deviations seen are for M99 fits, but they do not exceed 25% over the radial range resolved in the simulations. NFW fits fare better, with deviations that do not exceed 10%.

As with the density profiles, the deviations between simulation and fits, although small, increase toward the center, suggesting that caution should be exercised when extrapolating these fitting formulae beyond the spatial region where they have been validated. This is important because observational data, such as disk galaxy rotation curves, often extend to regions inside the minimum convergence radius in these simulations.

3.3.3 Radial dependence of logarithmic slopes

We have noted in the previous subsections that systematic deviations are noticeable in both NFW and M99 fits to the mass profiles of simulated ΛCDM halos. NFW fits tend to underestimate the dark matter density near the center, whilst M99 fits tend to overestimate the circular velocity in the inner regions. The reason for this is that *neither* fitting formula fully captures the radial dependence of the density profile. We explore this in Figure 3.6, which shows the logarithmic slope, $d\ln\rho/d\ln r \equiv -\beta(r)$, of all simulated halos, as a function of radius. Although there

is substantial scatter from halo to halo, a number of trends are robustly defined.

The first trend to note is that halo density profiles become shallower inward down to the innermost resolved radius, $r_{\rm conv}$ (the smallest radius plotted in Figure 3.6). *We see no indication for convergence to a well defined asymptotic value of the inner slope in our simulated halos*, neither to the $\beta_0 = \beta(r = 0) = 1$ expected for the NFW profile (solid curves in Figure 3.6) nor to the $\beta_0 = 1.5$ expected in the case of M99 (dotted curves in same figure).

The second trend is that the radial dependence of the logarithmic slope deviates from what is expected from either the NFW or the M99 fitting formula. Near $r_{\rm conv}$ slopes are significantly shallower than $\beta_0 = 1.5$ (and thus in disagreement with the M99 formula) but they are also significantly steeper than expected from NFW fits. In quantitative terms, let us consider the slope well inside the characteristic radius, r_{-2} (where the slope takes the "isothermal" value [2] of $\beta(r_{-2}) = 2$). For cluster halos, for example, at $r = 0.1\,r_{-2} \sim 50\,h^{-1}$ kpc the average slope is approximately -1.3, whereas the NFW formula predicts ~ -1.18 and M99 predicts ~ -1.5. This is in agreement with the latest results of Fukushige et al. (2003), who also report profiles shallower than $r^{-1.5}$ at the innermost converged radius of their simulations. A best-fit slope of $r^{-1.3}$ was also reported by Moore et al. (2001) for a dwarf galaxy halo (of mass similar to the Draco dwarf spheroidal), although that simulation was stopped at $z = 4$, and might therefore not be directly comparable to the results we present here.

This discrepancy in the radial dependence of the logarithmic slope between simulations and fitting formulae is at the root of the different interpretations of the structure of the central density cusp proposed in the literature. For example, because profiles become shallower inward more gradually than in the NFW formula,

[2] The characteristic radius, r_{-2}, as well as the density at that radius, $\rho_{-2} \equiv \rho(r_{-2}$, can be measured directly from the simulations, without reference to or need for any particular fitting formula. For the NFW profile, r_{-2} is equivalent to the scale radius r_s (see eq. 3.1). The density at r_{-2} is related to the NFW characteristic density, ρ_s, by $\rho_{-2} \equiv \rho(r_{-2}) = \rho_s/4$.

modifications with more steeply divergent cusps (such as eq. 3.2) tend to fit density profiles (but not circular velocity profiles) better in the region interior to r_{-2}. This is *not*, however, a sure indication of a steeper cusp. Indeed, *any* modification to the NFW profile that results in a more gradual change in the slope inside r_{-2} will lead to improved fits, *regardless* of the value of the asymptotic central slope. We show this explicitly below in § 3.3.6.

3.3.4 Maximum asymptotic slope

Conclusive proof that the central density cannot diverge as steeply as $\beta_0 = 1.5$ is provided by the total mass inside the innermost resolved radius, $r_{\rm conv}$. This is because, at any radius r, the mean density, $\bar{\rho}(r)$, together with the local density, $\rho(r)$, provide a robust upper limit to the asymptotic inner slope. This is given by $\beta_{\rm max}(r) = 3(1 - \rho(r)/\bar{\rho}(r)) > \beta_0$, under the plausible assumption that β is monotonic with radius.

Figure 3.7 shows $\beta_{\rm max}$ as a function of radius; clearly, except for possibly one dwarf system, no simulated halo has enough dark mass within $r_{\rm conv}$ to support cusps as steep as $r^{-1.5}$. The NFW asymptotic slope, corresponding to $\beta_0 = 1$, is still consistent with the simulation data, but the actual central value of the slope may very well be shallower. We emphasize again that there is no indication for convergence to a well defined value of β_0: density profiles become shallower inward down to the smallest resolved radius in the simulations.

3.3.5 A "universal" density profile

Figure 3.6 shows also that there is a well-defined trend with mass in the slope of the density profile measured at $r_{\rm conv} \sim 0.005$ to $0.01 r_{200}$ (the innermost point plotted for each profile): $\beta(r_{\rm conv}) \sim 1.1$ for clusters, ~ 1.2 for galaxies, and ~ 1.35 for dwarfs. A similar trend was noted by Jing and Suto (2000), who used it to argue against

a "universal" density profile shape. However, as discussed by Klypin et al. (2001), this is just a reflection of the trend between the concentration of a halo and its mass. It does *not* indicate any departure from similarity in the profile shape. Indeed, one does *not* expect the profiles of halos of widely different mass, such as those in our series, to have similar slopes at a constant fraction of the virial radius. Rather, if the density profiles are truly self-similar, slopes ought to coincide at fixed fractions of a *mass-independent* radial scale, such as r_{-2}.

Figure 3.8a shows the striking similarity between the structure of halos of different mass when all density profiles are scaled to r_{-2} and $\rho_{-2} \equiv \rho(r_{-2})$. The density profile of a dwarf galaxy halo then differs very little from that of a galaxy cluster 10^5 times more massive. This demonstrates that spherically-averaged density profiles are approximately "universal" in shape; rarely do individual density profiles deviate from the scaled average by more than $\sim 50\%$.

In the scaled units of Figure 3.8, the NFW and M99 profiles are fixed, and are shown as solid and dotted curves, respectively. With this scaling differences between density profiles are more evident than when best fits are compared, since the latter — by definition — minimize the deviations. In Figure 3.8a, for example, it is easier to recognize the "excess" of dark mass inside r_{-2} relative to the NFW profile that authors such as M99 and Fukushige & Makino (1997, 2001, 2003) have (erroneously) interpreted as implying a steeply divergent density cusp.

The similarity in mass profile shapes is also clear in Figure 3.8b, which shows the circular velocity curves of all halos in our series, scaled to the maximum, $V_{\rm max}$ and to the radius where it is reached, $r_{\rm max}$. NFW and M99 are again fixed curves in these scaled units. This comparison is more relevant to observational interpretation, since rotation curve, stellar dynamical, and lensing tracers are all more directly related to $V_c(r)$ than to $\rho(r)$. Because of the reduced dynamic range of the y-axis, the scatter in mass profiles from halo to halo is more clearly apparent in the V_c profiles; the NFW and M99 profiles appear to approximately bracket the extremes in the mass profile

shapes of simulated halos. We discuss below a simple fitting formula that, with the aid of an extra parameter, is able to account for the variety of mass profile shapes better that either the NFW or M99 formula.

3.3.6 An improved fitting formula

Although the discussion in the previous subsections has concentrated on global deviations from simple fitting formulae such as NFW or M99, it is important to emphasize again that such deviations, although significant, are actually rather small. As shown in Figure 3.5, best NFW fits reproduce the circular velocity profiles to an accuracy of better than $\sim$ 10% down to roughly 0.5% of r_{200}. Although this level of accuracy may suffice for some observational applications, the fact that deviations increase inward and are maximal at the innermost converged point suggests the need for a new fitting formula better suited for extrapolation to regions beyond those probed reliably by simulations.

Such improved fitting formula ought to reproduce: (i) the more gradual shallowing of the density profile towards the center; (ii) the apparent lack of evidence for convergence to a well-defined power-law behavior; and (iii) the significant scatter in profile shape from halo to halo. After some experimentation, we have found that a density profile where $\beta(r)$ is a power-law of radius is a reasonable compromise that satisfies these constraints whilst retaining simplicity;

$$\beta_\alpha(r) = -d\ln\rho/d\ln r = 2\,(r/r_{-2})^\alpha\,, \tag{3.4}$$

which corresponds to a density profile of the form,

$$\ln(\rho_\alpha/\rho_{-2}) = (-2/\alpha)[(r/r_{-2})^\alpha - 1]. \tag{3.5}$$

This profile has finite total mass (the density cuts off exponentially at large radius)

and has a logarithmic slope that decreases inward more gradually than the NFW or M99 profile. The thick dot-dashed curves in Figures 3.6 and 3.7 show that eq. 3.5 (with $\alpha \sim 0.17$) does indeed reproduce fairly well the radial dependence of $\beta(r)$ and $\beta_{\rm max}(r)$ in simulated halos.

Furthermore, adjusting the parameter α allows the profile to be tailored to each individual halo, resulting in improved fits. Indeed, as shown in Figure 3.9, eq. 3.5 reproduces the density profile of individual halos to better than $\sim$ 10% and the circular velocity profile to better than $\sim$ 5% over the reliably resolved radial range, and that there is no discernible radial trend in the residuals. This is a significant improvement over NFW or M99 fits, where the maximum deviations were found at the innermost resolved radius. The best-fit values of α (in the range 0.1 - 0.2) show no obvious dependence on halo mass, and are listed in Table 3.3. The average α is 0.172 and the dispersion about the mean is 0.032.

We note that the ρ_α profile is not formally divergent, and converges to a finite density at the center, $\rho_0 = e^{2/\alpha}\,\rho_{-2} \sim 6 \times 10^5 \rho_{-2}$ (for $\alpha = 0.15$). It is unclear at this point whether such asymptotic behavior is a true property of ΛCDM halos or simply an artifact of the fitting formula that results from imposing $\beta_0 = 0$ in eq. 3.4. The simulations show no evidence for convergence to a well defined central value for the density, but even in the best-resolved runs they only probe regions where densities do not exceed $\sim 10^2\,\rho_{-2}$. This is, for α in the range 0.1 - 0.2, several orders of magnitude below the maximum theoretical limit imposed by the $\rho_0 = e^{2/\alpha}\,\rho_{-2}$ constraint. We note as well that the convergence to $\beta_0 = 0$ is quite slow for the values of α favored by our fits. Indeed, for $\alpha = 0.1$, the logarithmic slope reaches a value significantly shallower than the NFW asymptotic slope well inside the convergence radius of our simulations; for example, $\beta_\alpha(r)$ reaches 0.5 only as far in as $r = 9.5 \times 10^{-7}\,r_{-2}$, corresponding to $r \sim 0.01$ pc for galaxy-sized halos. This implies that the ρ_α profile is in practice "cuspy" for most astrophysical applications. Establishing conclusively whether ΛCDM halos actually have divergent inner density cusps is a task that awaits

simulations with much improved resolution compared to those presented here.

3.3.7 Comparison between fitting formulae

Figure 3.10 compares the density and circular velocity profiles corresponding to the ρ_α formula (eq. 3.5) with the NFW and M99 profiles (left panels), as well as with the fitting formula proposed by (Stoehr et al., 2002, hereafter SWTS) to describe the structure of *substructure* halos.

The top left panel of Figure 3.10 shows that, despite its finite central density, the ρ_α profile can approximate fairly well either an NFW profile (for $\alpha \sim 0.2$) or an M99 profile (for $\alpha \sim 0.1$) for over three decades in radius. The circular velocity profile for $\alpha = 0.2$ is quite similar to NFW's (bottom left panel of Figure 3.10); the agreement in shape with the M99 V_c profile is somewhat poorer for all values of α.

Interestingly, the V_c profiles corresponding to ρ_α resemble parabolae in a log-log plot, and thus may be used to approximate as well the mass profiles of substructure halos, as discussed by SWTS. This is demonstrated in the bottom right panel of Figure 3.10, where we show that the V_c profiles corresponding to $\alpha = 0.1$, 0.2, and 0.7, are very well approximated by the SWTS formula,

$$\log(V_c/V_{\rm max}) = -a[\log(r/r_{\rm max})]^2, \tag{3.6}$$

for $a = 0.09$, 0.17, and 0.45, respectively. The latter value ($a = 0.45$, or $\alpha = 0.7$) corresponds to that reported by SWTS as the median of their best fits to the mass profile of substructure halos. Note that this is quite different from the $\alpha \sim 0.1$ - 0.2 required to fit isolated ΛCDM halos (see Table 3.3).

It might actually be preferable to adopt the ρ_α profile rather than the SWTS formula for describing substructure halos, since $\rho_\alpha(r)$ is monotonic with radius and extends over all space. This is not the case for SWTS, as shown in the top-right

panel of Figure 3.10. The SWTS density profiles are "hollow" (i.e., the density has a minimum at the center), and extend out to a maximum radius, given by $e^{1/4a}\, r_{\rm max}$. This is because the circular velocity in the outer regions of the SWTS formula fall off faster than Keplerian, and therefore the corresponding density becomes formally negative at a finite radius.

The ρ_α profile thus appears versatile enough to reproduce, with a single fitting parameter, the structure of ΛCDM halos and of their substructure. Since ρ_α captures the inner slopes better than either the NFW or M99 profile, it is also likely a safer choice should extrapolation of the mass profile beyond the converged radius prove necessary. We end by emphasizing, however, that all simple fitting formulae have shortcomings, and that *direct comparison with simulations rather than with fitting formulae should be attempted whenever possible.*

3.3.8 Scaling parameters

The application of fitting formulae such as the one described above requires a procedure for calculating the characteristic scaling parameters for given halo mass, once the power spectrum and cosmological parameters are specified. NFW developed a simple procedure for calculating the parameters corresponding to halos of given mass. Because of the close relationship between the scale radius, r_s, and characteristic density, ρ_s, of the NFW profile and the r_{-2} and ρ_{-2} parameters of eq. 3.5, we can use the formalism developed by NFW to compute the expected values of these parameters in a given cosmological model.

NFW interpreted the characteristic density of a halo as reflecting the density of the universe at a suitably defined time of collapse. Their formalism assigns to each halo of mass M (identified at $z = 0$) a collapse redshift, $z_{\rm coll}(M, f)$ defined as the time at which half the mass of the halo was first contained in progenitors more massive than a certain fraction f of the final mass. With this definition, and once f has been

chosen, $z_{\rm coll}$ can be computed by using the Press-Schechter theory (e.g., Lacey and Cole, 1993). The NFW model then assumes that the characteristic density of a halo (i.e., ρ_s in eq. 3.1) is proportional to the mean density of the universe at $z_{\rm coll}$.

The redshift dependence of the characteristic density was first probed in detail by (Bullock et al., 2001, hereafter B01), who proposed a modification to NFW's model where, for given halo mass, the scale radius, r_s, remains approximately constant with redshift. (Eke et al., 2001, hereafter ENS), on the other hand, argue that the characteristic density of a halo is determined by the *amplitude and shape* of the power spectrum, as well as by the universal expansion history. Their formalism reproduces nicely the original results of NFW as well as the redshift dependence pointed out by B01, and is applicable to more general forms of the power spectrum, including the "truncated" power spectra expected in scenarios such as warm dark matter (see ENS for more details).

We have used the ENS and B01 formalisms to predict the halo mass dependence of the scaling parameters, ρ_{-2} and r_{-2}, and we compare the results with our simulations in Figure 3.11. The ENS prediction is shown by the solid line whereas the dotted line shows that of B01. Both formalisms reproduce reasonably well the trend seen in the simulations, so that one can use either, in conjunction with eq. 3.5, to predict the structure of a ΛCDM halo.

However, we note that neither formalism captures perfectly the mass dependence of the characteristic density; small but significant deviations, as well as a sizable scatter, are evident in Figure 3.11. Dwarf galaxy halos appear to be less concentrated than expected from the formalism proposed by B01; a similar observation applies to cluster halos when compared to ENS' predictions. This appears to contradict the results presented in Chapter 2 for the concentration of simulated halos as measured by the halo central density parameter, $\Delta_{V/2}$, propsed by Alam et al. (2002) (see eq. 2.9). Figure 2.16 shows that the B01 model accurately predicts the mean central densities of simulated dwarf halos, whereas ENS underpredicts $\Delta_{V/2}$ for these halos.

Similarly, ENS accurately predicts $\Delta_{V/2}$ for cluster-sized halos, but overpredicts ρ_{-2} for these halos. The reason for this apparent discrepancy is illustrated in Figure 3.12. Here we plot the velocity profile corresponding to eq. 3.5 for values of α spanning the range found for simulated halos ($0.1 \leq \alpha \leq 0.2$) along with the NFW V_c profile. All profiles are scaled horizontally to the radius, r_{-2}, of the corresponding density profile. For $\alpha = 0.1$, the radius $r_{V/2}$ at which the V_α profile reaches 0.5 $V_{\rm max}$ is smaller by a factor of 2.5 relative to the NFW profile. As a result, the central density $\Delta_{V/2} \propto (V_{\rm max}/r_{V/2})^2$ of the NFW profile can underestimate that of simulated halos by up to a factor of ~ 6. This further illustrates the uncertainties inherent when approximating simulation results with fitting formulae. Such shortcomings should be considered when deriving cosmological constraints from fits to observational data (see, e.g., Zentner and Bullock, 2002; McGaugh et al., 2003) and suggest again that direct comparison between observation and simulations is preferable to the use of fitting formulae.

3.4 Summary

We have analyzed the mass profile of ΛCDM halos in a series of simulations with high mass, spatial, and temporal resolution. Our series targets halos spanning five decades in mass: "dwarf" galaxy halos with virial circular velocities of order $V_{200} \sim 30$ km s^{-1}; "galaxy"-sized halos with $V_{200} \sim 200$ km s^{-1}; and "cluster" halos with $V_{200} \sim 1200$ km s^{-1}. Each of the nineteen halos in our series was simulated with comparable numerical resolution: they have between 8×10^5 and 4×10^6 million particles within the virial radius, and have been simulated following the "optimal" prescription for time-stepping and gravitational softening laid down in the numerical convergence study of P03.

The high resolution of our simulations allows us to probe the inner properties of the mass profiles of ΛCDM halos, down to $\sim 0.5\%$ of r_{200} in our best resolved runs.

These results have important implications for the structure of the inner cusp in the density profile and resolve some of the disagreements arising from earlier simulation work. Our main conclusions may be summarized as follows.

- ΛCDM halo density profiles are "universal" in shape: i.e., a simple fitting formula reproduces the structure of all simulated halos in our series, regardless of mass. Both the NFW profile and the profile proposed by M99 describe the density and circular velocity profiles of simulated halos reasonably well. Best NFW fits to the circular velocity profiles deviate by less than 10% over the region which is well resolved numerically. Best M99 fits reproduce circular velocity profiles to better than 25% over the same region. It should be noted, however, that the deviations increase inward and are typically maximal at the innermost resolved radius, a result that warns against extrapolating to smaller radii with these fitting formulae.

- ΛCDM halos appear to be "cuspy": i.e., the dark matter density increases monotonically toward the center with no evidence for a well-defined "core" of constant density. We find no evidence, however, for a central asymptotic power-law in the density profiles. These become progressively shallow inward and are significantly shallower than isothermal at the innermost resolved radius, $r_{\rm conv}$. At $r \sim 0.01\, r_{200}$, the average slope of "cluster," "galaxy," and "dwarf" halos is $\beta(r_{\rm conv}) \sim 1.1$, ~ 1.2, and ~ 1.35, respectively. This is steeper than predicted by the NFW profile but shallower than the asymptotic slope of the M99 profile.

- The density and enclosed mass at $r_{\rm conv}$ may be used to derive an upper limit on any asymptotic value of the inner slope. Cusps as steep as $\beta_0 = 1.5$ are confidently ruled out in essentially all cases, although the asymptotic slope of the NFW profile ($\beta_0 = 1$) is still consistent with our data. The radial dependence of $\beta(r)$ differs from that of the NFW profile, however, decreasing more slowly

with decreasing radius than is predicted. For some scalings of the NFW fitting formula to the numerical data, this shape difference appears as a dark matter "excess" near the center which has (erroneously) been interpreted indicating a steeply divergent density cusp.

- A simple formula where $\beta(r)$ is a power law of radius reproduces the gradual radial variation of the logarithmic slope and its apparent failure to converge to any specinfic asymptotic value (eq. 3.5). This formula leads to much improved fits to the density profiles of simulated halos, and may prove a safer choice when comparison with observation demands extrapolation below the innermost converged radii of the simulations.

Our study demonstrates that, although simple fitting formulae such as NFW are quite accurate in describing the global structure of ΛCDM halos, one should be aware of the limitations of these formulae when interpreting observational constraints. Extrapolation beyond the radial range where these formulae have been validated is likely to produce substantial errors. Proper accounting for the substantial scatter in halo properties at given halo mass also appears necessary when assessing the consistency of observations with a particular cosmological model. Direct comparison between observations and simulations (rather than with fitting formulae) is clearly preferable whenever possible. Given the computational challenge involved in providing consistent, robust, and reproducible theoretical predictions for the inner structure of CDM halos it is likely that observational constraints will exercise to the limit our hardware and software capabilities for some time to come.

Table 3.1: Parameters of the parent cosmological simulations

Label	$L_{\rm box}$ $[h^{-1}$ Mpc]	z_i	m_p $[h^{-1}\,M_\odot]$	ϵ $[h^{-1}$ kpc]	CODE
ENS01	32.5	49.0	1.36×10^9	10	AP3M
SGIF-128	35.325	49.0	1.75×10^9	10	GADGET
ΛCDM-512	479.0	36.0	6.82×10^{10}	30	GADGET

Table 3.2: Main parameters of resimulated halos

Label	z_i	ϵ $[h^{-1}$ kpc]	N_{200}	M_{200} $[h^{-1}\,M_\odot]$	r_{200} $[h^{-1}$ kpc]	V_{200} [km s^{-1}]	$r_{\rm conv}$ $[h^{-1}$ kpc]	CODE
D1	74	0.0625	784980	7.81×10^9	32.3	32.3	0.34	GADGET
D2	49	0.0625	778097	9.21×10^9	34.1	34.1	0.37	GADGET
D3	49	0.0625	946421	7.86×10^9	32.3	32.3	0.33	GADGET
D4	49	0.0625	1002098	9.72×10^9	34.7	34.7	0.32	GADGET
G1	49	0.15625	3447447	2.29×10^{12}	214.4	214.4	1.42	GADGET
G2	49	0.5	4523986	2.93×10^{12}	232.6	232.6	1.25	PKDGRAV
G3	49	0.45	2661091	2.24×10^{12}	212.7	212.7	1.65	PKDGRAV
G4	49	0.3	3456221	1.03×10^{12}	164.0	164.0	1.01	PKDGRAV
G5	49	0.35	3913956	1.05×10^{12}	165.0	165.0	1.02	PKDGRAV
G6	49	0.35	3739913	9.99×10^{11}	162.5	162.5	1.03	PKDGRAV
G7	49	0.35	3585676	9.58×10^{11}	160.3	160.3	1.02	PKDGRAV
C1	36	5.0	1565576	7.88×10^{14}	1502.1	1502.1	16.8	GADGET
C2	36	5.0	1461017	7.36×10^{14}	1468.1	1468.1	16.9	GADGET
C3	36	5.0	1011918	5.12×10^{14}	1300.6	1300.6	16.1	GADGET
C4	36	5.0	1050402	5.31×10^{14}	1316.7	1316.7	15.9	GADGET
C5	36	5.0	1199299	6.05×10^{14}	1375.5	1375.5	16.2	GADGET
C6	36	5.0	1626161	8.19×10^{14}	1521.1	1521.1	15.5	GADGET
C7	36	5.0	887837	4.50×10^{14}	1245.8	1245.8	16.4	GADGET
C8	36	5.0	1172850	5.92×10^{14}	1365.4	1365.4	16.8	GADGET

Table 3.3: Fit and structural parameters of resimulated halos†

Label	r_{-2} $[h^{-1}$ kpc]	ρ_{-2} $[\rho_{\rm crit}]$	$r_{\rm max}$ $[h^{-1}$ kpc]	$V_{\rm max}$ [km s^{-1}]	r_s $[h^{-1}$ kpc]	ρ_s $[\rho_{\rm crit}]$	r_M $[h^{-1}$ kpc]	ρ_M $[\rho_{\rm crit}]$	r_α $[h^{-1}$ kpc]	ρ_α $[\rho_{\rm crit}]$	α
D1	3.23	1.12×10^4	7.11	39.2	2.59	7.03×10^4	5.38	7.58×10^3	2.67	1.53×10^4	0.16
D2	3.04	1.58×10^4	8.87	42.5	2.43	9.61×10^4	2.27	1.17×10^5	2.78	1.82×10^4	0.21
D3	2.57	1.58×10^4	5.42	37.0	2.94	5.01×10^4	4.05	2.51×10^4	2.83	1.18×10^4	0.12
D4	2.57	2.24×10^4	4.73	45.9	2.06	1.49×10^5	2.18	1.36×10^5	2.09	3.39×10^4	0.17
G1	18.5	6.76×10^3	59.1	248	21.3	4.06×10^4	19.4	8.43×10^4	23.9	7.47×10^3	0.18
G2	28.0	2.40×10^3	61.5	291	15.5	1.13×10^5	19.4	8.43×10^4	17.2	2.09×10^4	0.17
G3	20.2	6.31×10^3	77.7	227	25.8	1.52×10^4	47.3	8.24×10^3	33.6	1.99×10^3	0.14
G4	29.6	4.37×10^3	29.9	194	13.3	6.78×10^4	16.8	3.44×10^4	14.8	1.19×10^4	0.14
G5	20.7	1.58×10^4	47.1	147	15.0	5.20×10^4	15.3	4.23×10^4	17.2	9.37×10^3	0.19
G6	39.6	2.00×10^3	71.3	182	16.6	3.79×10^4	20.7	2.03×10^4	19.7	5.89×10^3	0.14
G7	16.4	1.26×10^4	43.0	196	13.4	6.22×10^4	14.9	5.15×10^4	14.8	1.18×10^4	0.18
C1	584	4.68×10^2	1375	1521	440	3.36×10^3	661	1.58×10^3	861	2.16×10^2	0.13
C2	395	1.15×10^3	1005	1516	362	5.17×10^3	396	4.46×10^3	403	1.02×10^3	0.22
C3	327	1.12×10^3	637	1384	249	9.07×10^3	278	7.44×10^3	288	1.60×10^3	0.19
C4	416	7.94×10^2	759	1387	315	5.47×10^3	339	4.91×10^3	402	7.70×10^2	0.16
C5	287	1.91×10^3	591	1417	271	8.45×10^3	326	5.88×10^3	304	1.64×10^3	0.21
C6	382	1.32×10^3	745	1640	297	8.70×10^3	302	8.75×10^3	333	1.66×10^3	0.20
C7	569	3.55×10^2	1082	1255	283	3.92×10^3	475	2.11×10^3	390	4.62×10^2	0.13
C8	368	1.00×10^3	824	1446	361	4.41×10^3	345	5.04×10^3	390	9.18×10^2	0.22

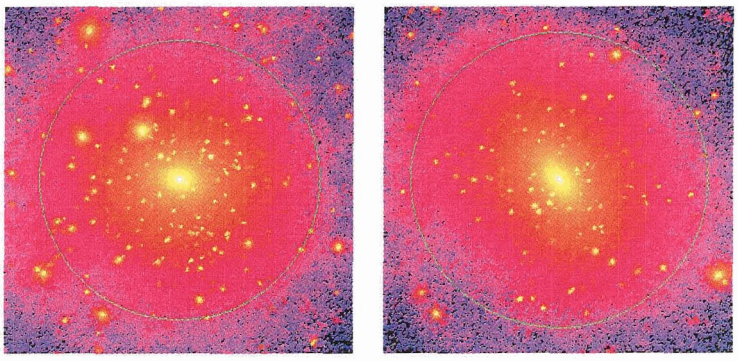

(a) D1 (b) D2

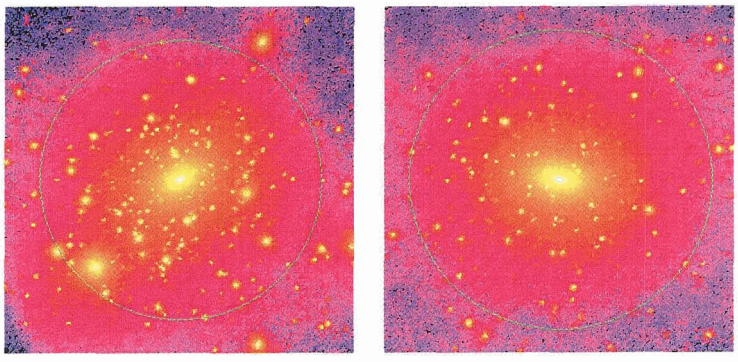

(c) D3 (d) D4

Figure 3.1: Snapshots of four dwarf galaxy-sized halos at $z = 0$ within a box 80 h^{-1}kpc on a side. Particles are colour-coded by density and virial radius, r_{200}, is shown by green circle.

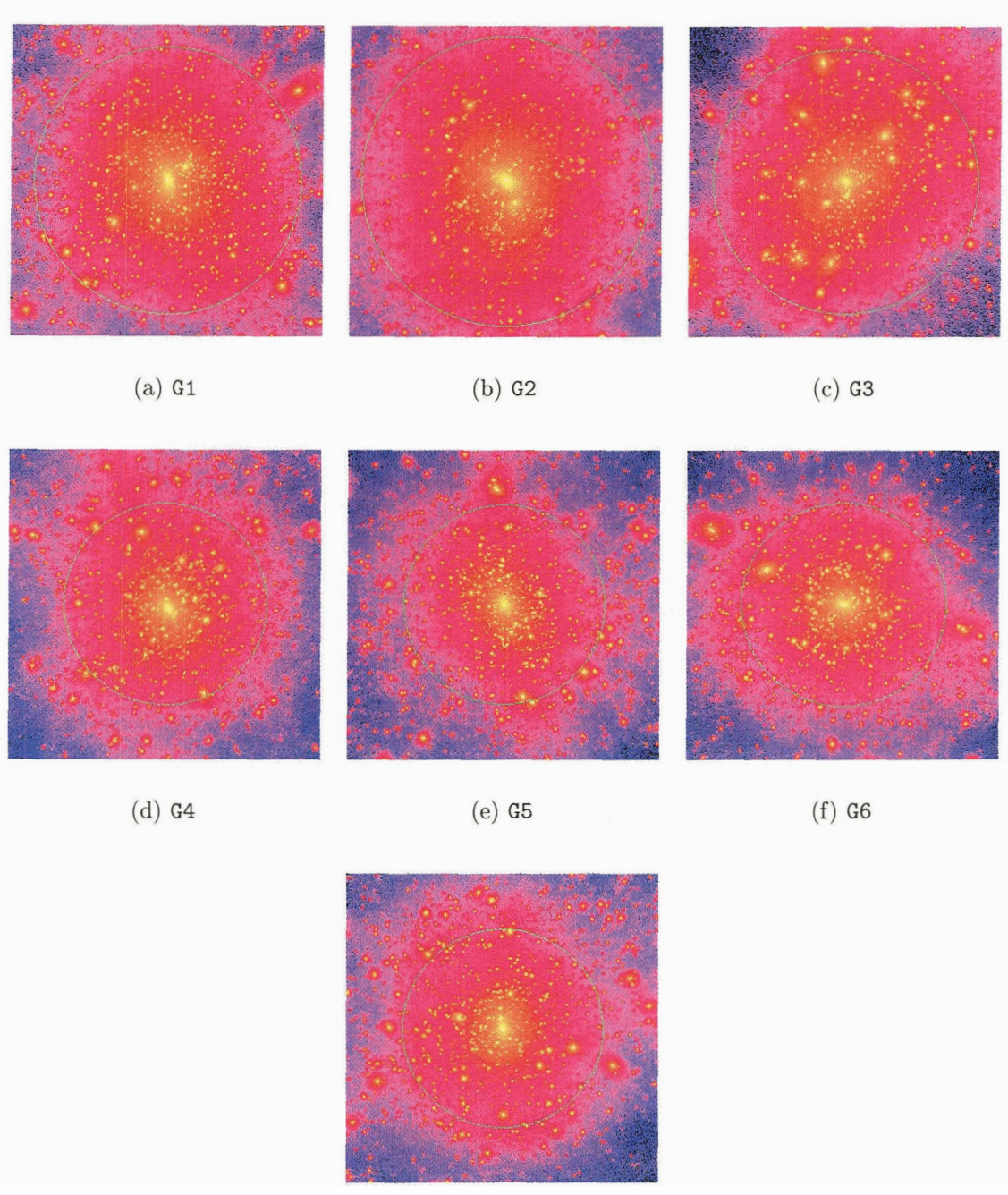

(a) G1 (b) G2 (c) G3

(d) G4 (e) G5 (f) G6

(g) G7

Figure 3.2: Snapshots of seven galaxy-sized halos at $z = 0$ within a box 500 h^{-1}kpc on a side. Particles are colour-coded by density and virial radius, r_{200}, is shown by green circle.

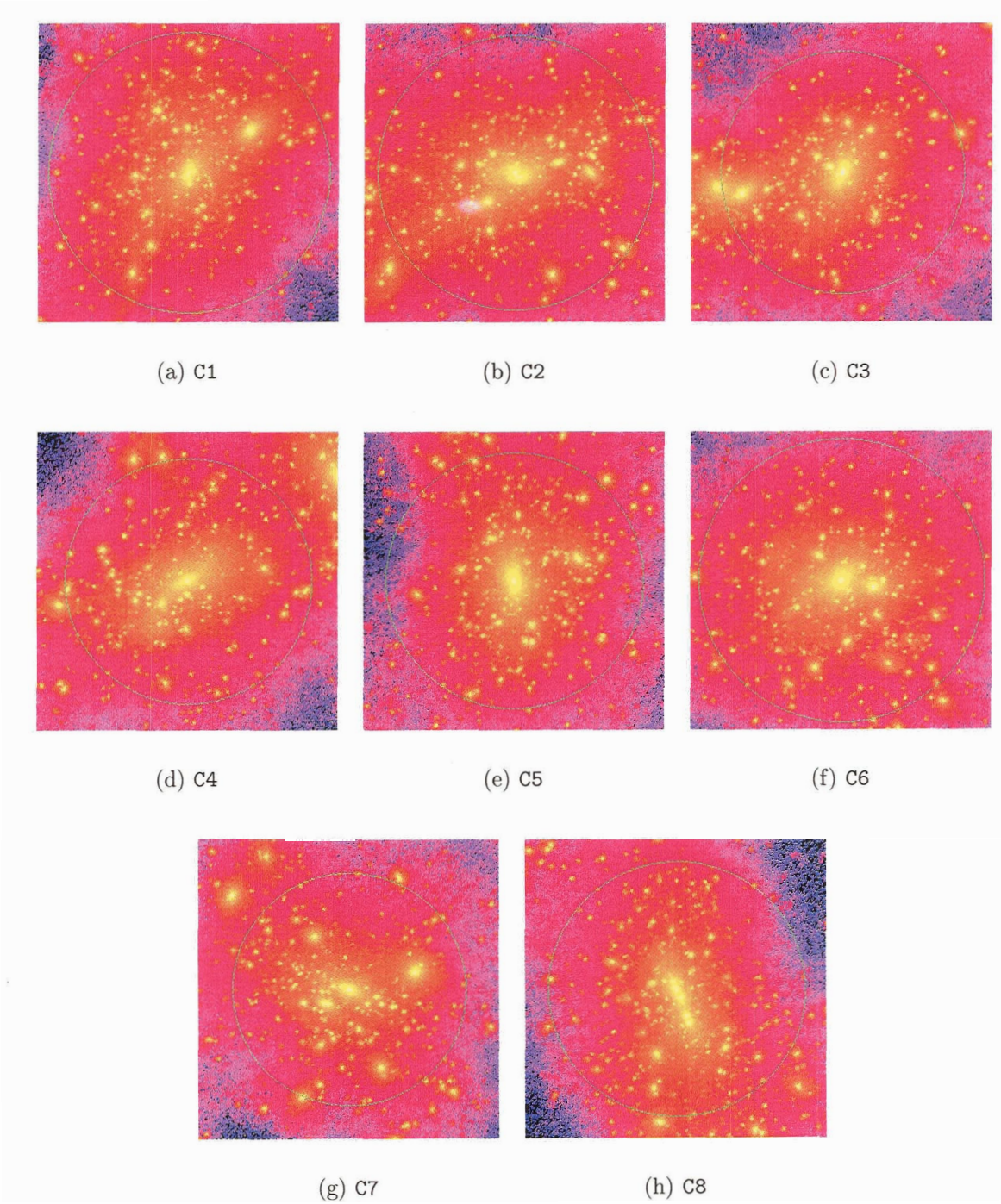

(a) C1 (b) C2 (c) C3

(d) C4 (e) C5 (f) C6

(g) C7 (h) C8

Figure 3.3: Snapshots of eight cluster-sized halos at $z = 0$ within a box 3.2 h^{-1}Mpc on a side. Particles are colour-coded by density and virial radius, r_{200}, is shown by green circle.

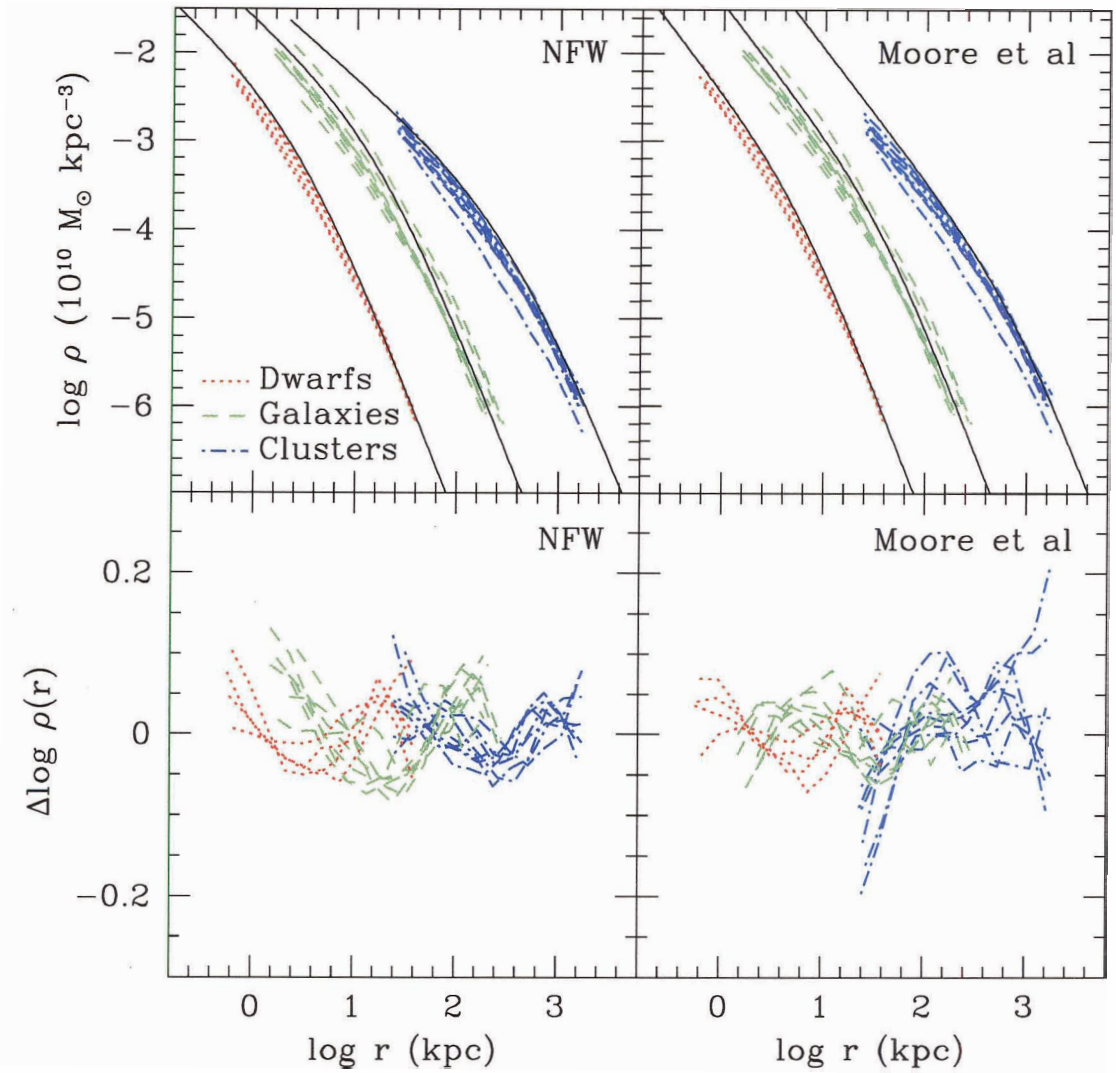

Figure 3.4: Spherically-averaged density profiles of all simulated halos in our series. Densities are computed in radial bins of equal logarithmic width and are shown from the innermost converged radius ($r_{\rm conv}$) out to about the virial radius of each halo (r_{200}). Our simulations target halos in three distinct mass groups: "dwarf," "galaxy," and "cluster" halos. These groups span more than five decades in mass. Thick solid lines in the top panels illustrate the expected halo profile for each mass range according to the fitting formula proposed by NFW (top-left) or M99 (top-right). Bottom panels indicate the deviation from the *best* fit achieved for each individual halo with the NFW profile (eq. 3.1) or with its modified form, as proposed by M99 (eq. 3.2).

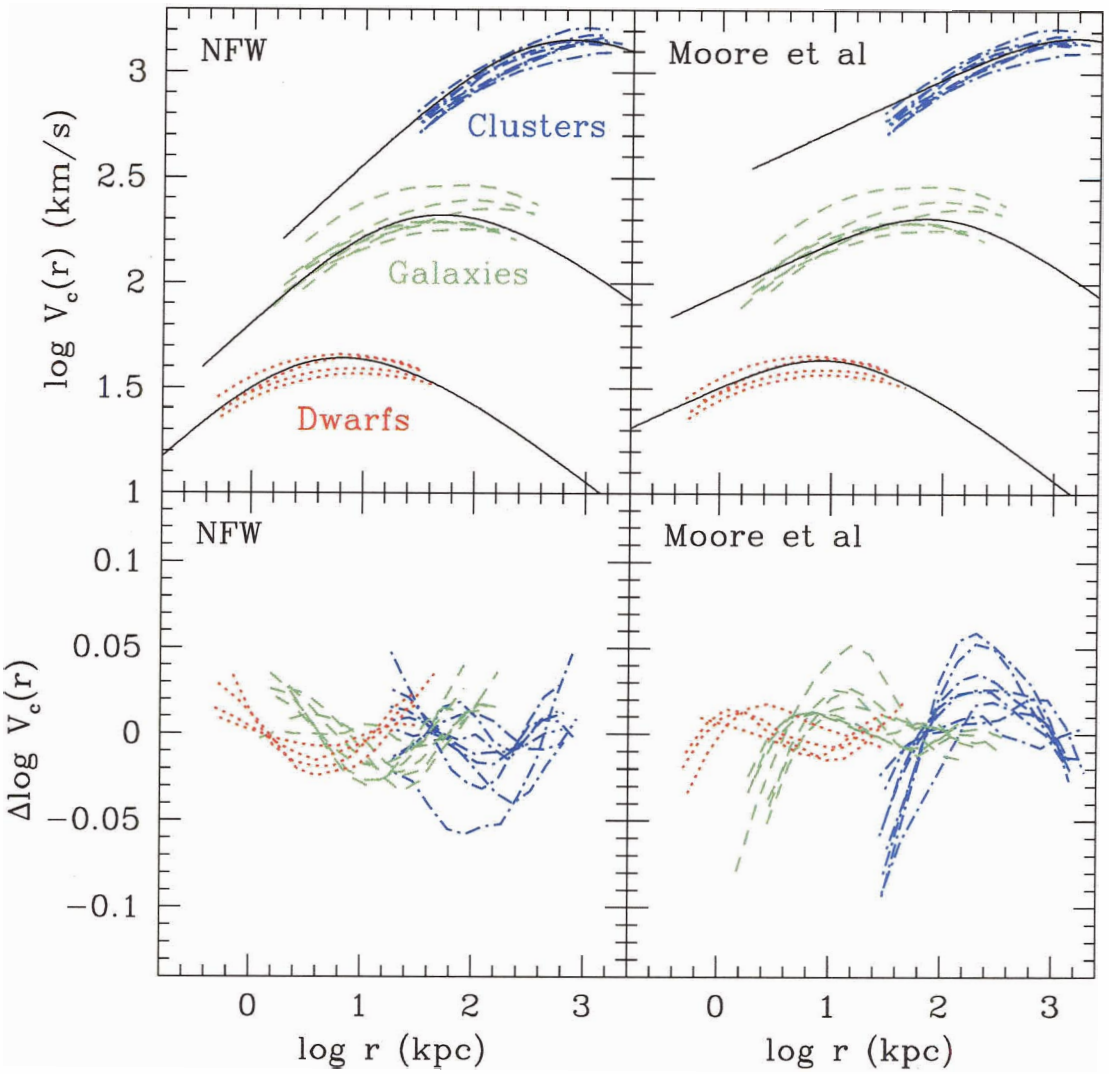

Figure 3.5: Spherically-averaged circular velocity ($V_c(r) = \sqrt{GM(r)/r}$) profiles of all simulated halos in our series. As in Figure 3.4, circular velocities are computed in radial bins of equal logarithmic width and are shown from the innermost converged radius ($r_{\rm conv}$) out to about the virial radius (r_{200}) of each halo. Our simulations target halos in three distinct mass groups: "dwarf," "galaxy," and "cluster" halos, spanning more than a factor of ~ 50 in velocity. Thick solid lines in the top panels illustrate the expected profile for each mass range according to the fitting formula proposed by NFW (top-left) or M99 (top-right). Bottom panels indicate the deviation from the *best* fit achieved for each individual halo with the NFW profile (eq. 3.1) or with its modified form, as proposed by M99 (eq. 3.2).

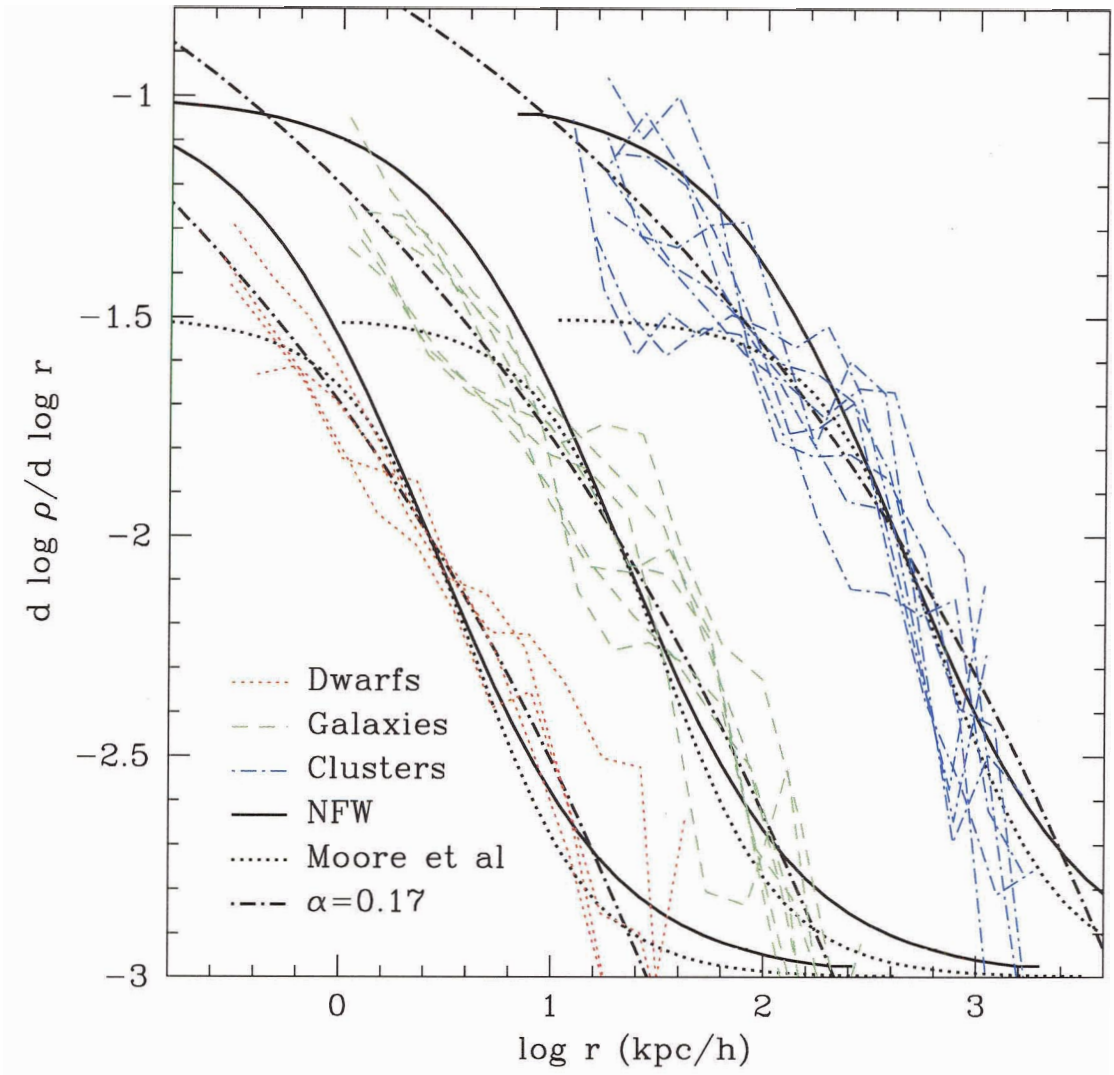

Figure 3.6: Logarithmic slope of the density profile of all halos in our sample, plotted versus radius. Thick solid and dotted curves illustrate the radial dependence of the slope expected from the NFW profile (eq. 3.1) and the modification proposed by M99 (eq. 3.2), respectively. Note that although both fitting formulae have well-defined asymptotic inner slopes (-1 and -1.5, respectively) there is no sign of convergence to a well defined value of the central slope in the simulated halos. At the innermost converged radius the simulated halo profiles are shallower than -1.5, in disagreement with the Moore et al profile. Also, inside r_{-2} the profiles appear to get shallower more gradually than in the NFW formula. A power-law radial dependence of the slope seems to fit the results of our simulations better; the dot-dashed lines indicate the predictions of the ρ_α profile introduced in eqs. 3.4 and 3.5 for $\alpha = 0.17$. Best fits to individual halos yield α in the range 0.1-0.2 (see Table 3.3).

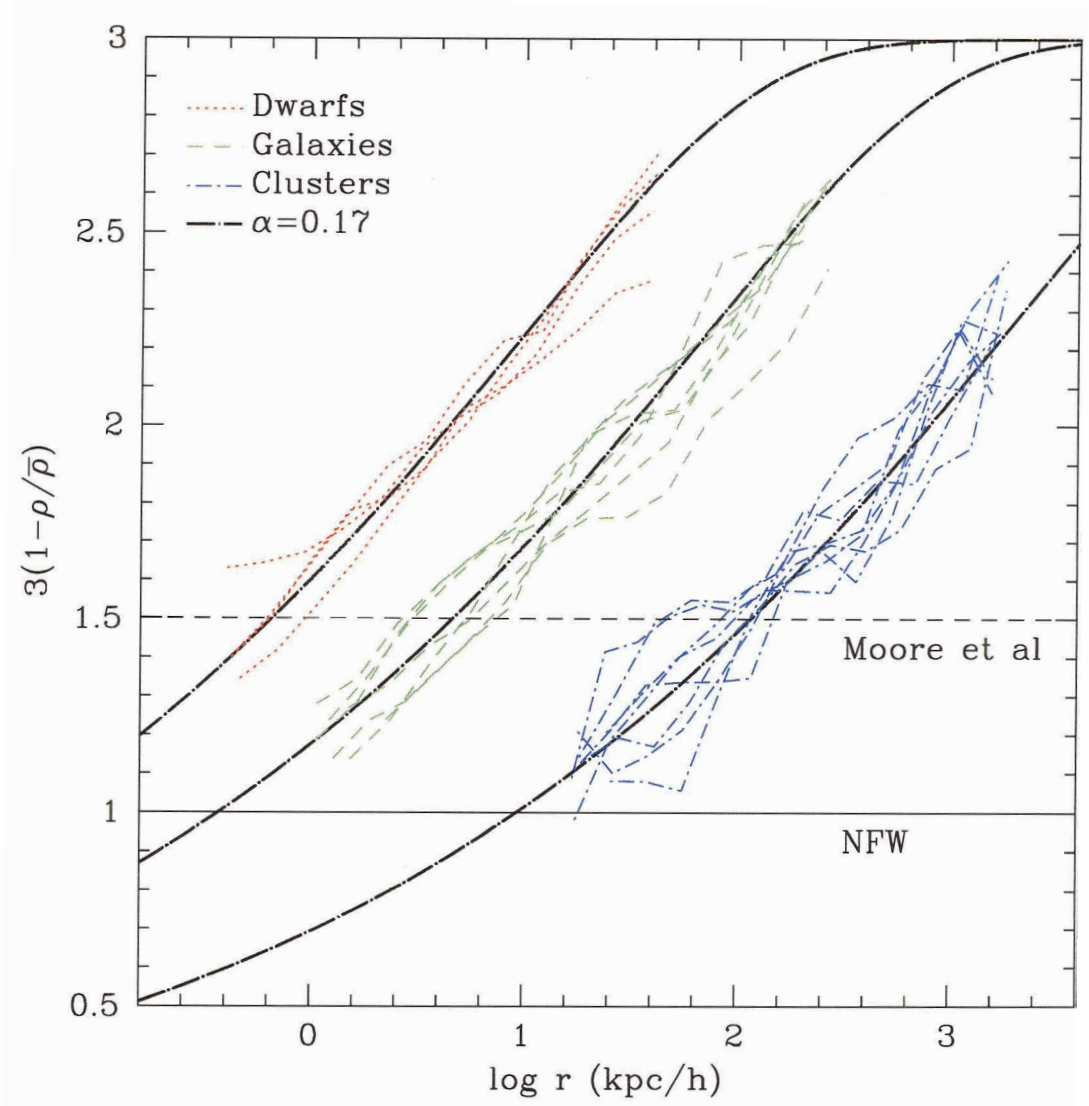

Figure 3.7: Maximum asymptotic inner slope compatible with the mean density interior to radius r, $\bar{\rho}(r)$, and with the local density at that radius, $\rho(r)$. This provides a robust limit to the central slope, $\beta_0 < \beta_{\rm max}(r) = -3(1 - \rho(r)/\bar{\rho}(r))$, under the plausible assumption that β is monotonic with radius. Note that there is not enough mass within the innermost converged radius in our simulations to support density cusps as steep as $r^{-1.5}$. The asymptotic slope of the NFW profile, $\beta_0 = 1$, is still compatible with the simulated halos, although there is no convincing evidence for convergence to a well defined power law behavior in any of our simulated halos. The thick dot-dashed curves illustrate the expected radial dependence of $\beta_{\rm max}$ for the ρ_α profile introduced in § 3.3.6, for $\alpha = 0.17$.

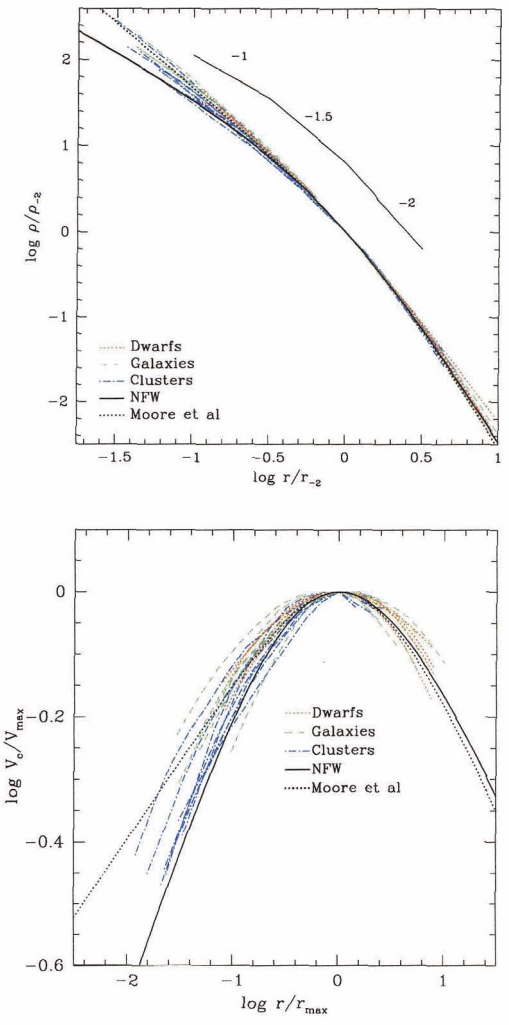

Figure 3.8: (a-upper) Density profiles of all halos in our series, scaled to the radius, r_{-2}, where the local logarithmic slope of the density profile takes the isothermal value of $\beta = -d\log\rho/d\log r = 2$. Densities are scaled to $\rho_{-2} = \rho(r_{-2})$. This figure shows that, with proper scaling, there is little difference in the shape of the density profile of halos of different mass, confirming the "universal" nature of the mass profile of ΛCDM halos. The NFW profile (eq. 3.1) is a fixed curve in these scaled units, and is shown with a thick solid line. The M99 formula (eq. 3.2) is shown with a dashed line. (b-lower) Circular velocity profiles all halos in our series, scaled to the maximum velocity, $V_{\rm max}$, and to the radius at which it is reached, $r_{\rm max}$. Note the significant scatter from halo to halo, and also that the NFW and M99 profiles appear to bracket the extremes of the mass profile shapes of halos in our simulation series.

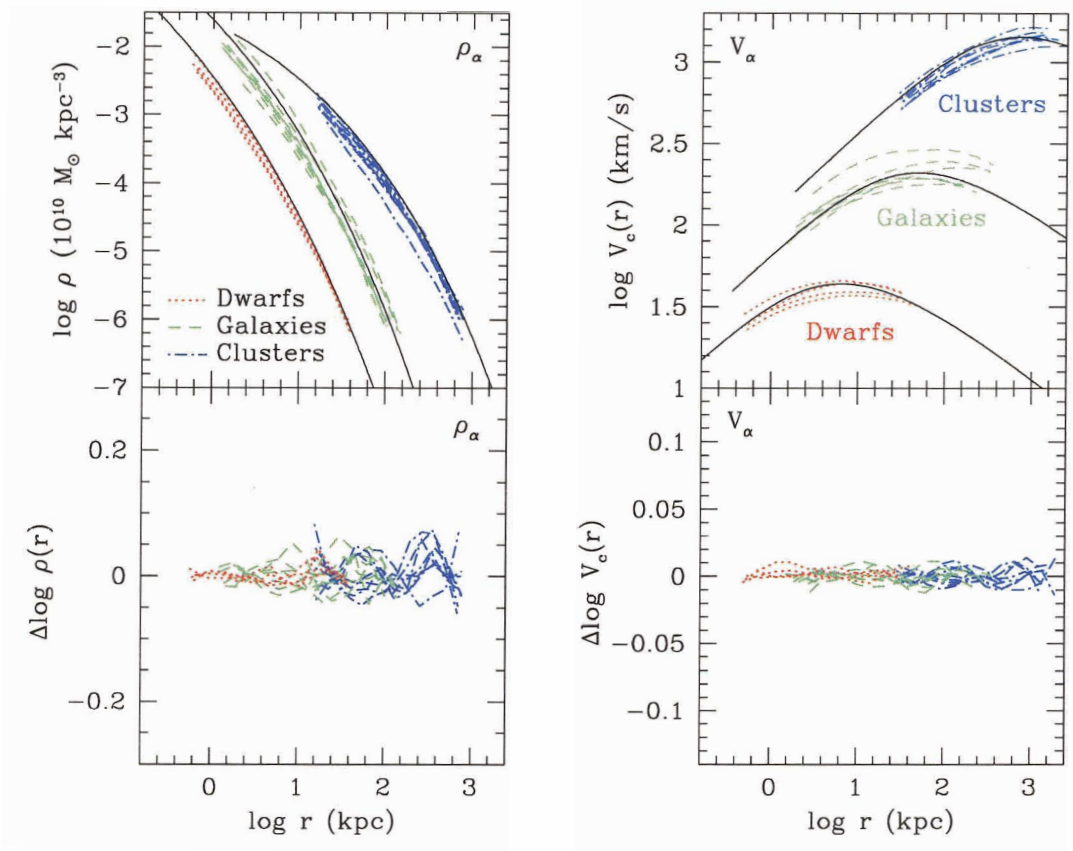

Figure 3.9: As Figures 3.4 and 3.5, but for the density (left panels) and circular velocity (right panels) profiles corresponding to the ρ_α fitting formula presented in eq. 3.5. Thick solid lines in the top panels illustrate the expected halo profile for each mass range according to the prescription proposed by NFW. Bottom panels indicate the deviation from the *best* ρ_α and V_α fits achieved for each individual halo. Note the improvement in the fits compared with those achieved with the NFW or M99 profile and shown in Figure 3.4.

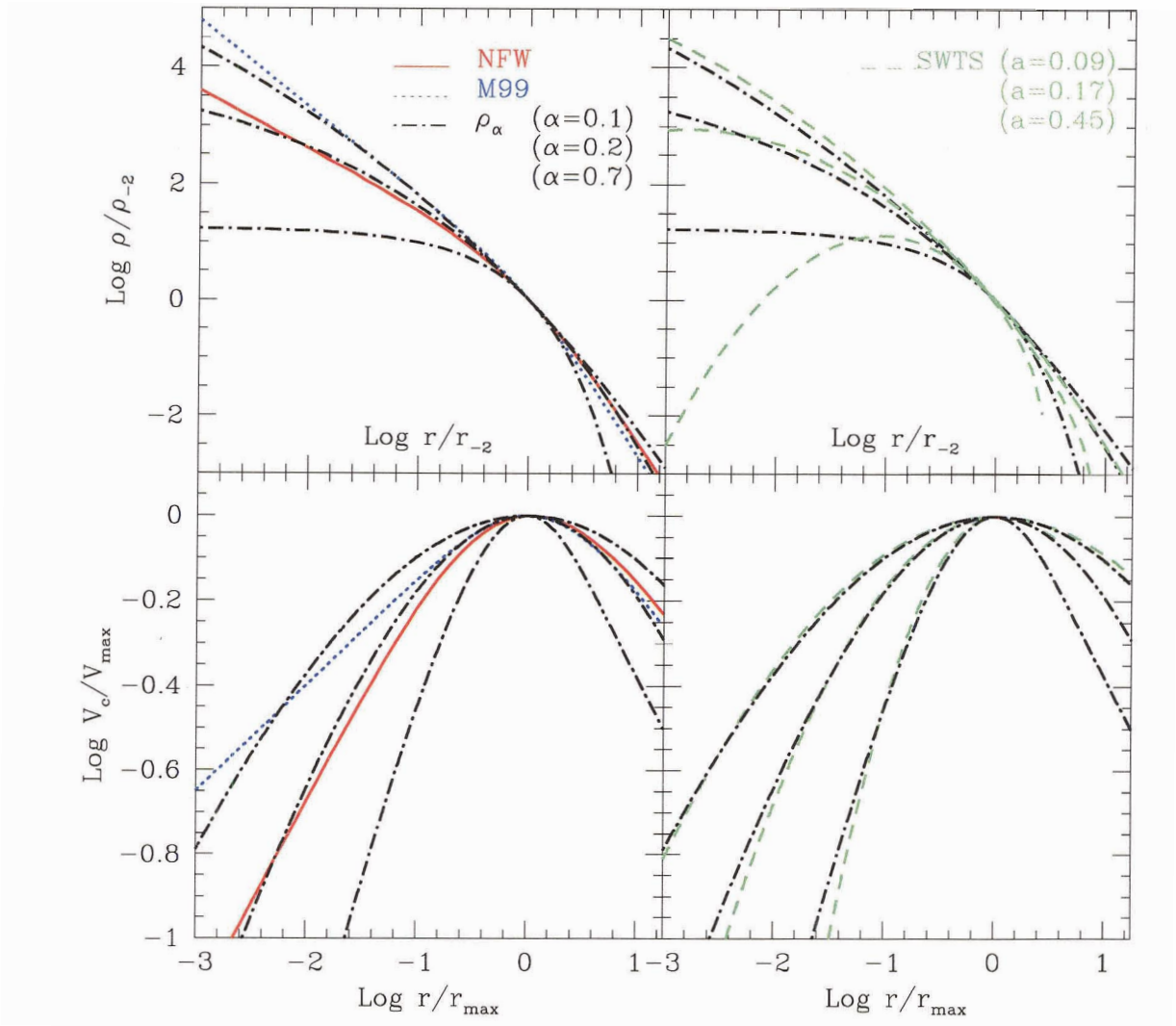

Figure 3.10: Comparison between the density (top) and circular velocity (bottom) profiles corresponding to four different fitting formulae: NFW (solid curves, eq. 3.1), M99 (dotted curves, eq. 3.2), SWTS (dashed curves, eq. 3.6), as well as ρ_α (dot-dashed curves, eq. 3.5). Circular velocity profiles are scaled to the maximum, $V_{\rm max}$, and to the radius where that is reached, $r_{\rm max}$. Density profiles are scaled as in Figure 3.8. Note that, despite having a finite central density, the ρ_α formula matches, for about 3 decades in radius, the NFW profile (for $\alpha = 0.2$) or the M99 profile (for $\alpha = 0.1$, see top left panel). It also matches closely the SWTS "parabolic" circular velocity profiles intended to reproduce *substructure* halos (see bottom right panel): the V_c profile with $\alpha = 0.7$ is very similar to the SWTS profile with $a = 0.45$, the median value of the fits to substructure halos reported by SWTS. See text for further discussion.

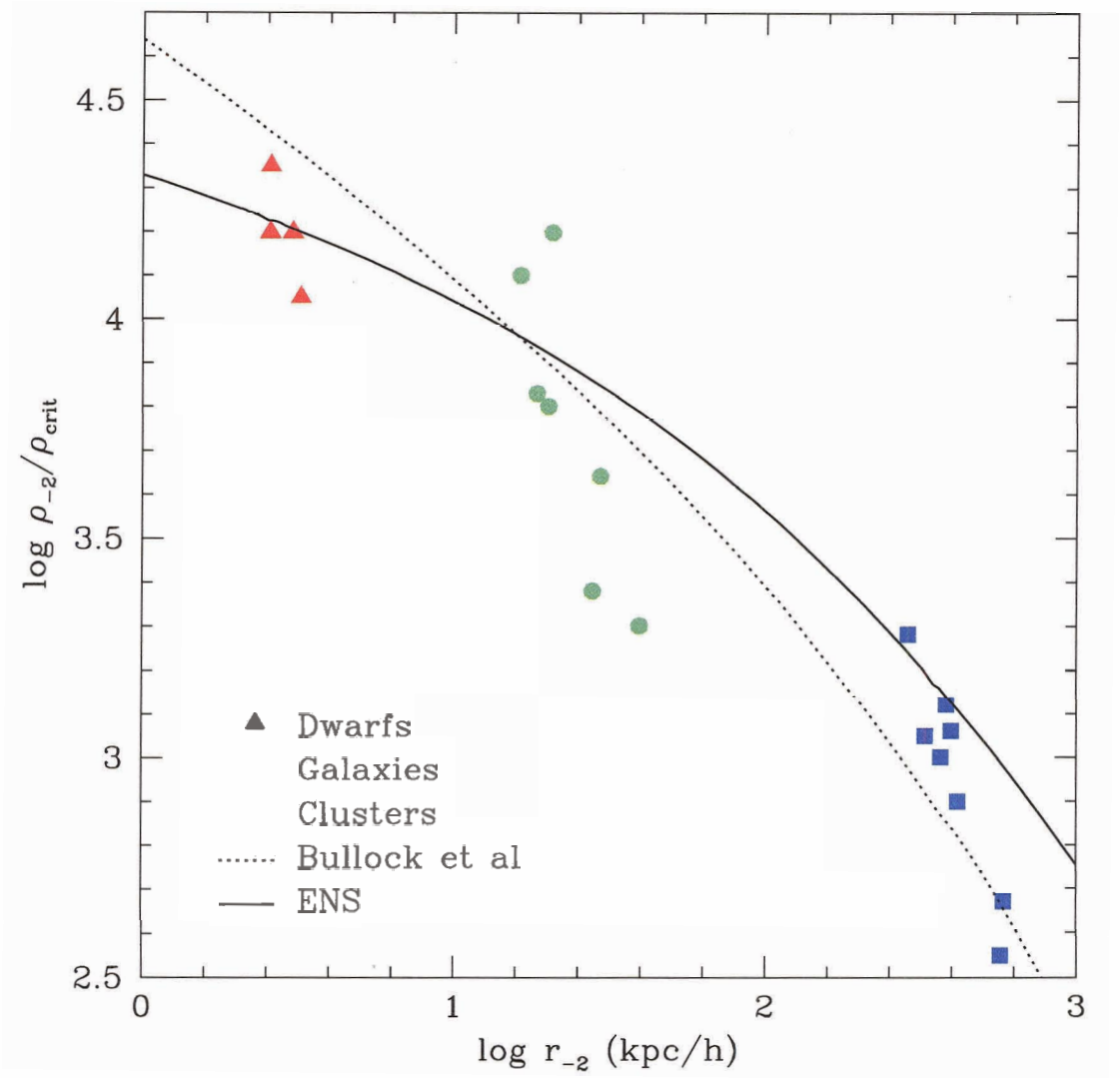

Figure 3.11: The radius, r_{-2}, where the logarithmic slope of the density profile takes the "isothermal" value, $\beta(r_{-2}) = 2$, plotted versus the local density at that radius, $\rho_{-2} = \rho(r_{-2})$, for all simulated halos in our series. This figure illustrates the mass dependence of the central concentration of dark matter halos: low mass halos are systematically denser than their more massive counterparts. Solid and dotted lines indicate the mass-density correlation predicted by the formalisms presented by Eke, Navarro & Steinmetz (2001) and Bullock et al (2001). These parameters may be used, in conjunction with eq. 3.5, to predict the mass profile of ΛCDM halos.

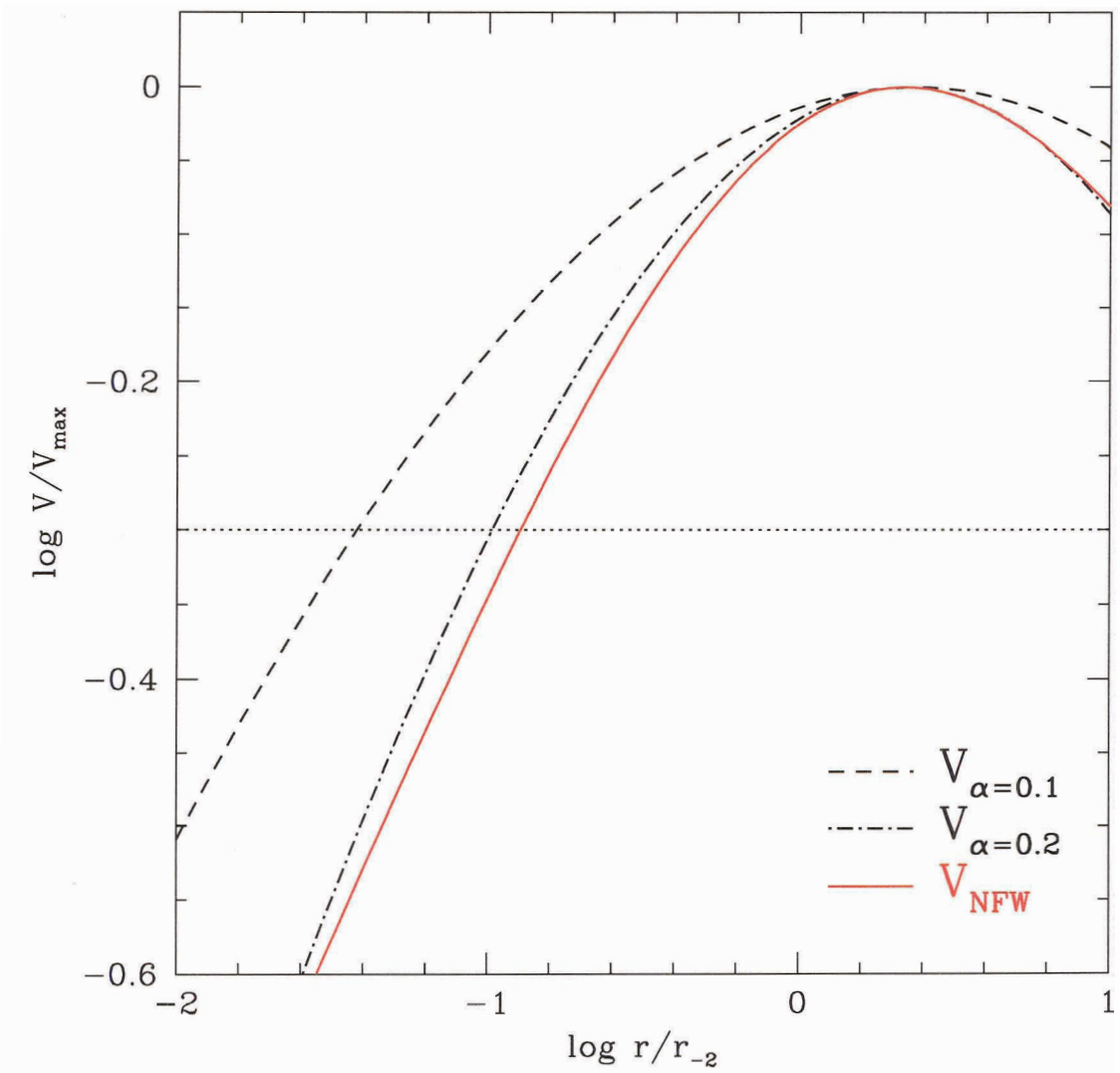

Figure 3.12: Velocity profiles corresponding to eq. 3.5 for $\alpha = 0.1$ and $\alpha = 0.2$ compared to the NFW V_c profile. Profiles are scaled horizontally to the radius, r_{-2}, and vertically to the maximum velocity, $V_{\rm max}$ of each profile. Dotted horizontal line indicates $V = 0.5\ V_{\rm max}$. For $\alpha = 0.1$, the radius $r_{V/2}$ at which the V_α profile reaches $0.5\ V_{\rm max}$ is smaller by a factor of 2.5 relative to the NFW profile. As a result, the central density $\Delta_{V/2} \propto (V_{\rm max}/r_{V/2})^2$ of the NFW profile tends to underestimate that of simulated halos by up to a factor of ~ 6 for $\alpha = 0.1$.

Chapter 4

Disk Galaxy Rotation Curves in Triaxial CDM Halos

Abstract

We use N-body hydrodynamical simulations to study the structure of disks in triaxial potentials resembling CDM halos. Our analysis focuses on the accuracy of the dark mass distribution inferred from rotation curves derived from simulated long-slit spectra. We consider a massless disk embedded in a halo with axis ratios of 0.5: 0.6: 1.0 and with its rotation axis aligned with the minor axis of the halo. Closed orbits for the gaseous particles deviate from coplanar circular symmetry, resulting in a variety of long-slit rotation curve shapes, depending on the orientation of the disk relative to the line of sight. Rotation curves may thus differ significantly from the spherically-averaged circular velocity profile of the dark matter halo. "Solid-body" rotation curves—typically interpreted as a signature of a constant density core in the dark matter distribution—are obtained about 20% of the time for random orientations although the dark matter follows the cuspy density profile proposed by Navarro, Frenk & White (NFW). We conclude that the discrepancies reported between the shape of the rotation curve of low surface brightness galaxies and the structure of CDM halos may be resolved once the complex effects of halo triaxiality on the dynamics of the gas component is properly taken into account. This proposal should be substantiated by a proper statistical analysis of the frequency of solid-body rotators expected within CDM halos and by the identification of corroborating evidence for triaxiality in two-dimensional velocity field data.

4.1 Introduction

It is commonly believed that the inner regions of low surface brightness (LSB) galaxies are ideal probes of the inner structure of dark matter halos. Given the small contribution of the baryonic component to the mass budget in these galaxies, dynamical tracers of the potential such as rotation curves are expected to cleanly trace the dark matter distribution. This provides important astrophysical clues to the nature of dark matter, since the spatial distribution of dark material in these highly non-linear regions is expected to be quite sensitive to the physical properties of the dark matter.

LSB rotation curves can thus be contrasted directly with theoretical predictions of the inner structure of halos, and there is now an extensive body of work in the literature that reports substantial disagreement between the shape of LSB rotation curves and that of circular velocity curves of simulated cold dark matter (CDM) halos (see, e.g., Flores and Primack, 1994; Moore, 1994; McGaugh and de Blok, 1998; de Blok et al., 2001b). Some of these rotation curves are fit better by circular velocity curves arising from density profiles with a constant density "core" rather than by the "cuspy" density profiles commonly used to fit the structure of CDM halos (Navarro, Frenk & White 1996, 1997, hereafter NFW). This discrepancy adds to a growing list of concerns regarding the consistency of CDM with observational constraints on the scale of individual galaxies (see, e.g., Sellwood and Kosowsky, 2001) that has prompted calls for a radical revision of the CDM paradigm on small scales (see, e.g., Spergel and Steinhardt, 2000).

Before accepting the need for radical modifications to CDM it is important to note a number of caveats that apply to the LSB rotation curve problem.

- Many of the early rotation curves where the disagreement was noted were significantly affected by beam smearing in the HI data (Swaters et al., 2000). The observational situation has now improved substantially thanks to higher-

resolution rotation curves obtained from long-slit Hα observations (see, e.g., de Blok and Bosma, 2002; Swaters et al., 2003a). We shall restrict our analysis to these newer datasets in what follows.

- Strictly speaking, the observational disagreement is with the fitting formulae used to parameterize the structure of simulated CDM halos (usually the profile proposed by NFW), rather than with the structure of simulated halos themselves. Although the fitting formulae provide a simple and reasonably accurate description of the mass profile of CDM halos, the radial range over which they have been validated often does not coincide with the scales where the disagreement has been identified.

- Small but significant deviations between the NFW profile and simulated halos have been reported as the mass and spatial resolution of the simulations has increased (Moore et al., 1998; Ghigna et al., 2000; Fukushige and Makino, 1997, 2001). Although there is no broad consensus yet regarding how these deviations may affect the comparison with observed rotation curves (see, e.g., Power et al., 2003; Hayashi et al., 2003; Navarro et al., 2004), the fact that the deviations worsen towards the centre advise against using extrapolations of simple fitting formulae such as the NFW profile to assess consistency with observation.

- Finally, it must be emphasized that the "cusp vs. core" problem arises when comparing rotation speeds of LSB disks to spherically-averaged circular velocities of dark matter halos. Given that CDM halos are expected to be significantly non-spherical (Davis et al., 1985; Frenk et al., 1988; Jing et al., 1995; Jing and Suto, 2002), some differences between the two are to be expected. It is therefore important to use the full 3D structure of CDM halos to make predictions regarding the rotation curves of gaseous disks that may be compared directly to observation.

We address the latter issue in this chapter, by exploring numerically the closed orbits of gaseous particles within the potential of an idealized triaxial CDM halo. We embed a massless, isothermal gaseous disk within a cuspy dark matter halo and evolve it until equilibrium is reached.

We focus our analysis on the *shape* of the rotation curves inferred for the disk from simulated long-slit observations of the velocity field; on deviations from the spherically-averaged circular velocity curve; and on the possibility that such deviations might account for the discrepancy between LSB rotation curves and NFW profile fits to CDM halos.

4.2 LSB rotation curves

Figure 4.1 illustrates the disagreement alluded to above. This figure shows the Hα rotation curves of two LSB galaxies (points with error bars) selected from the sample of de Blok and Bosma (2002, B02) and Swaters et al. (2003a, S03). The data points have been fitted using a simple formula, $V_{\rm rot}(r) = V_0(1 + (r/r_t)^{-\gamma})^{-1/\gamma}$ (Courteau, 1997). Here V_0 and r_t are dimensional scaling parameters, whereas γ is a dimensionless parameter that characterizes the *shape* of the rotation curve. This three-parameter formula provides excellent fits to both LSBs, as illustrated by the quality of the (solid line) fits shown in Figure 4.1.

In order to emphasize discrepancies in shape, the rotation curves in Figure 4.1 have been scaled to the radius, $r_{0.3}$, and velocity, $V_{0.3}$, where the logarithmic slope of the curve is $d\log V_{\rm rot}/d\log r = 0.3$. The two galaxies shown in Figure 4.1 have different values of γ, and have been chosen to illustrate the extreme cases in the B02 and S03 datasets. Roughly one third of their LSBs have $\gamma \lesssim 1$, having rotation curves with shapes similar to UGC 5721 ($\gamma = 0.6$).

The dashed line in Figure 4.1 shows the V_c profile of an NFW halo, which is fixed in these scaled units. Galaxies with $\gamma \lesssim 1$ are consistent with NFW, whereas those

with $\gamma \gg 1$ are clearly inconsistent. Figure 4.1 also shows the spherically-averaged V_c profiles of all galaxy-sized halos presented in Chapters 2 and 3 at redshifts $1 < z < 0$, scaled to $r_{0.3}$ and $V_{0.3}$. We find that the shapes of the dark halo V_c curves are in fact quite similar to NFW. In terms of the γ parameter, most halos (about 95%) have $\gamma \lesssim 1$, which implies that LSBs with $\gamma \gg 1$ are quite difficult to reconcile with the V_c profiles of simulated CDM halos.

On further examination, however, we note in Chapter 2 that most rotation curves that have best fit values of $\gamma > 1$ also have acceptable fits with $\gamma \leq 1$. As a result, only a small minority of LSBs (about 10%) are robustly inconsistent with CDM halo V_c profiles. Most of these curves are characterized by a linear rise in velocity with radius and have best fit values of $\gamma \gtrsim 5$. One such example, UGC 5750, is shown in Figure 4.1, along with a dot-dashed line that illustrates the $V \propto r$ dependence expected in the presence of a constant density core.

Does this result rule out the presence of a cusp in the dark matter density profile in such galaxies? As noted in § 4.1, before concluding so one must take into account possible systematic differences between rotation speed and circular velocity in gaseous disks embedded within realistic, triaxial halos. This is a complex issue that involves a number of parameters, such as the degree of triaxiality, the role of the disk's self-gravity, size, and orientation, as well as the possibility of transient deviations from equilibrium.

To keep matters simple, we have decided to address this issue by evolving a massless gaseous disk at the centre of a fixed triaxial halo. We use the N-body/hydrodynamical code `GASOLINE`, developed by J.Wadsley, J.Stadel, and T.Quinn (Wadsley et al., 2004). `GASOLINE` combines a tree-based Poisson solver for gravitational interactions with the Smooth Particle Hydrodynamics (SPH) technique. The dark matter halo is modelled with a particle realization of an NFW mass profile; the mass, virial radius and concentration of the halo are normalized to $M_{200} = 10^{11}\ M_{\odot}/h$, $r_{200} = 75\ h^{-1}$kpc and $c = 12$, respectively. In order to reduce computational expense, the halo is trun-

cated at an outermost radius, $r_{\rm trunc} = 37.5\ h^{-1}$kpc and the number of particles within this radius is set to 1.7×10^5. The halo is made triaxial by multiplying the x-, y-, and z-coordinates of the halo particles by factors of 1.36, 0.82, and 0.68, respectively, so that the spherically-averaged mass profile remains unchanged, but the axis ratios of the halo are 0.5: 0.6: 1.0. We note that such halo shapes (roughly prolate with elongation 2:1) are among the most common ones found in cosmological simulations (see, e.g., Jing and Suto, 2002). The gravitational potential is derived directly from the dark matter particle positions and is assumed to remain constant in time.

An exponential disk consisting of 10^4 massless gas particles is placed at the centre of the halo, in the plane of the major and intermediate axes of the halo (see Figure 4.2). The exponential scale length of the disk is $r_d = 3.6\ h^{-1}$kpc, and its outermost radius is $r_{\rm outer} = 18.0\ h^{-1}$kpc. The vertical distribution of the disk material is given by $\rho(z) \propto {\rm sech}^2(z/z_0)$, with $z_0 = 0.6\ h^{-1}$kpc, and the disk is truncated at $z_{\rm max} = 3.0\ h^{-1}$kpc. The gas is given a temperature $T = 100\ K$, well below the virial temperature of the halo, $T_{\rm vir} \simeq 2 \times 10^5$ K, and is assumed to remain isothermal during the evolution. Pressure forces are thus unimportant for the dynamics of the gas, and the hydrodynamical treatment simply forces the gas to provide a massless tracer of the closed orbits within the halo potential.

The disk particles are initially given tangential velocities consistent with the spherically-averaged circular velocity profile of the triaxial dark matter halo. As a result the gaseous disk is not initially in equilibrium and it evolves rapidly to a configuration characterized by departures from circular symmetry (the disk becomes elliptical, see Figure 4.2). The effect of such departures from circular symmetry on rotation curves derived from long-slit spectra is complex, as illustrated in Figure 4.3. This figure compares the rotation speed of the gas, as inferred from line-of-sight velocities measured on a slit placed along the photometric major axis of the disk determined from the projected particle distribution. The disk is inclined by 67°, and velocities are corrected by the sine of the inclination angle, $i_{\rm obs}$, as derived from the

aspect ratio of the isodensity contours of the gas.[1]

The left panels in Figure 4.3 show that initially, when the disk is circularly symmetric by construction, the disk inclination is recovered reasonably accurately and the rotation speed inferred from line-of-sight velocities (open circles) agree well with the spherically-averaged circular velocity (dashed line). Fitting the halo V_c profile out to $r_{\rm outer} = 18\ \ h^{-1}$kpc using the (r_t, γ, V_0) formula results in best fit values of $\gamma = 1$, whereas the initial disk rotation curve is best fit by $\gamma = 1.3$.

At later times the evolution of the disk leads to poorer estimates of the inclination as well as to significant deviations between inferred rotation speed and circular velocity. The *shape* of the rotation curve, in particular, is affected, as shown in the right-hand panels in Figure 4.3. On some projections, rotation curves appear to rise and turn abruptly, and they would be (erroneously) taken to imply the existence of a constant-density core in simple models that assume spherical symmetry. Fits to the disk rotation curves using the (r_t, γ, V_0) formula introduced above often have $\gamma \gg 1$, consistent with galaxies where NFW profiles provide a particularly poor fit to the rotation curve data. The open triangles in the lower panels of Figure 4.3 show the rotation curves obtained with the slit oriented along the minor axis of the disk. The misalignment between the photometric and kinematic axes of the disk after 7.0 Gyr is clearly evident.

We have calculated the distribution of γ values for rotation curves obtained by observing the simulated disk at time $t = 7.0$ Gyr from 1000 random lines-of-sight with inclination angles limited to $30° < i < 70°$. A large fraction of rotation curves have values of γ significantly higher than the initial value of $\gamma = 1.3$. To be precise, approximately $45\%, 25\%$, and 7%, have $\gamma > 2, > 3$, and > 4, respectively. Furthermore, minor axis rotation is seen with a peak amplitude exceeding 20% of the major axis amplitude in 70% of simulated rotation curves with $\gamma > 3$.

[1]This is inferred to be $\simeq 58°$ because the disk is not circularly symmetric.

In Figure 4.5, we compare the high-γ LSB rotation curve shown in Figure 4.1 with one obtained from the projection of the disk shown in Figure 4.3. The agreement between the simulated and observed rotation curves is excellent, suggesting that deviations from spherical symmetry in CDM halos might reconcile disk rotation curves that appear to favour the presence of constant density cores with cusps in the dark matter density profiles.

4.3 Discussion

Given that we are able to match discrepant rotation curve shapes with a disk embedded in a cuspy triaxial halo, the outlook for reconciling dark matter cusps with LSB rotation curves is rather encouraging. However, it would be premature to argue that the problem has been fully solved. After all, given the number of extra "free" parameters introduced by relaxing the assumption of spherical symmetry, it is perhaps not surprising that one is able to improve the agreement with LSB rotation curves.

It is therefore important to build a more compelling case for this interpretation of LSB rotation curves, so as to render it falsifiable. Are there any corroborating traits that may be used to confirm or exclude the hypothesis that halos surrounding LSBs are indeed triaxial? In particular, we would like to understand better the particular combination of perspective and triaxiality that results in rotation curves with values of $\gamma > 1$. How can one best verify the triaxial-halo interpretation in two-dimensional velocity maps? Identifying a clean and unambiguous indication of triaxiality, such as the unusual minor axis kinematics shown in Figure 4.3, will be as important as the success of aspherical halos in reproducing the rich variety of shapes of LSB rotation curves. Only if this is accomplished shall we be able to conclude that LSB rotation curves do not preclude the presence of dark matter density cusps, thereby freeing the CDM paradigm of one vexing challenge on small scales.

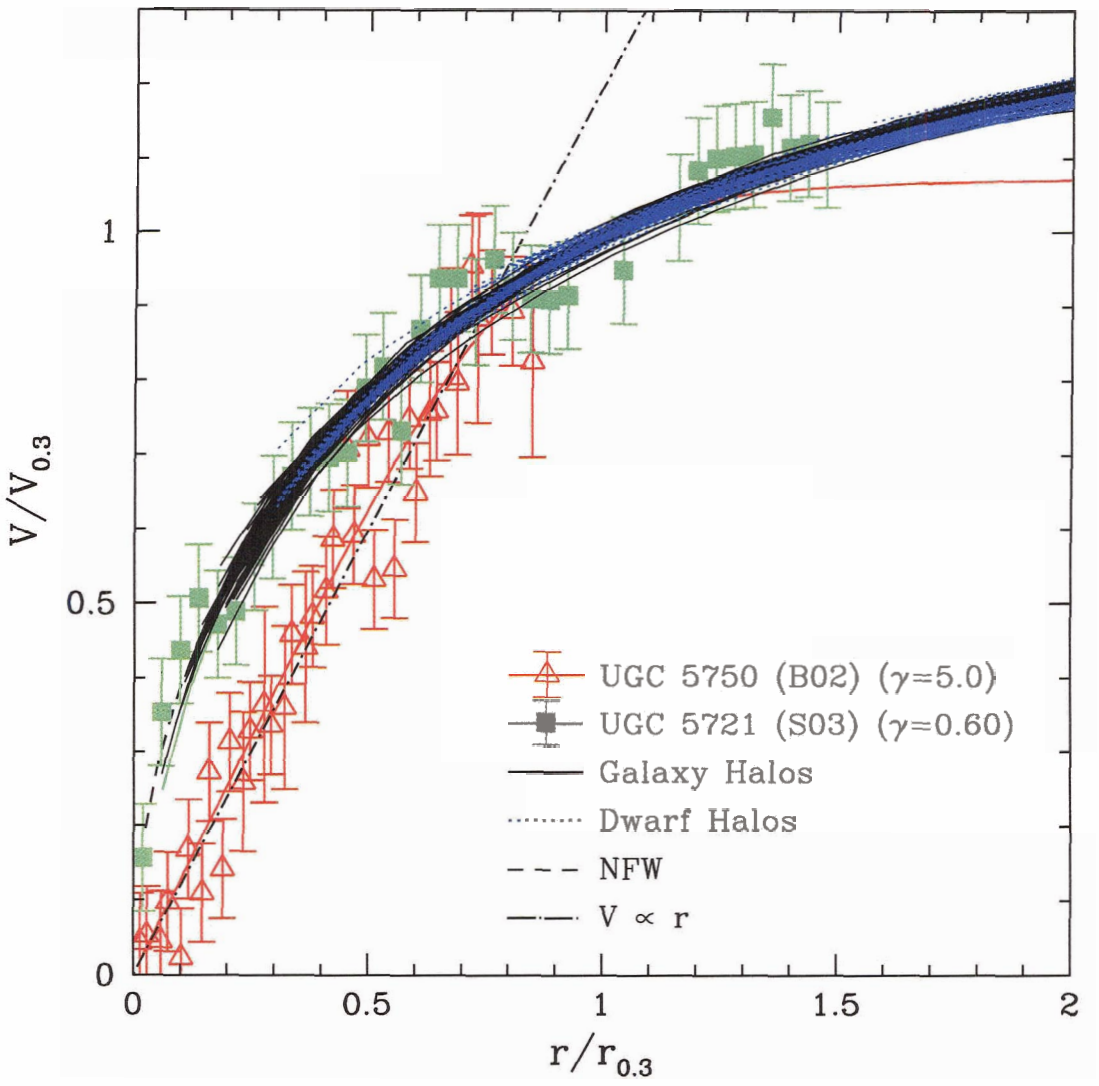

Figure 4.1: Rotation curves of two LSB galaxies from the samples of de Blok and Bosma (2002, B02) and Swaters et al. (2003a, S03), chosen to illustrate their various shapes, as measured by the parameter γ from fits with the Courteau (1997) fitting formula. Rotation curves have been scaled to the radius $r_{0.3}$ and corresponding velocity $V_{0.3}$ where where the slope of the curve is $d\log V_{\rm rot}/d\log r = 0.3$. Fits with large γ values are characterized by a linear rise in velocity with radius followed by a sharp transition to the flat part of the curve. The NFW profile (dashed line) and the V_c profiles of simulated dwarf- (dotted lines) and galaxy-sized halos (solid lines) match reasonably well systems with $\gamma \lesssim 1$ but cannot account for those with $\gamma \gg 1$.

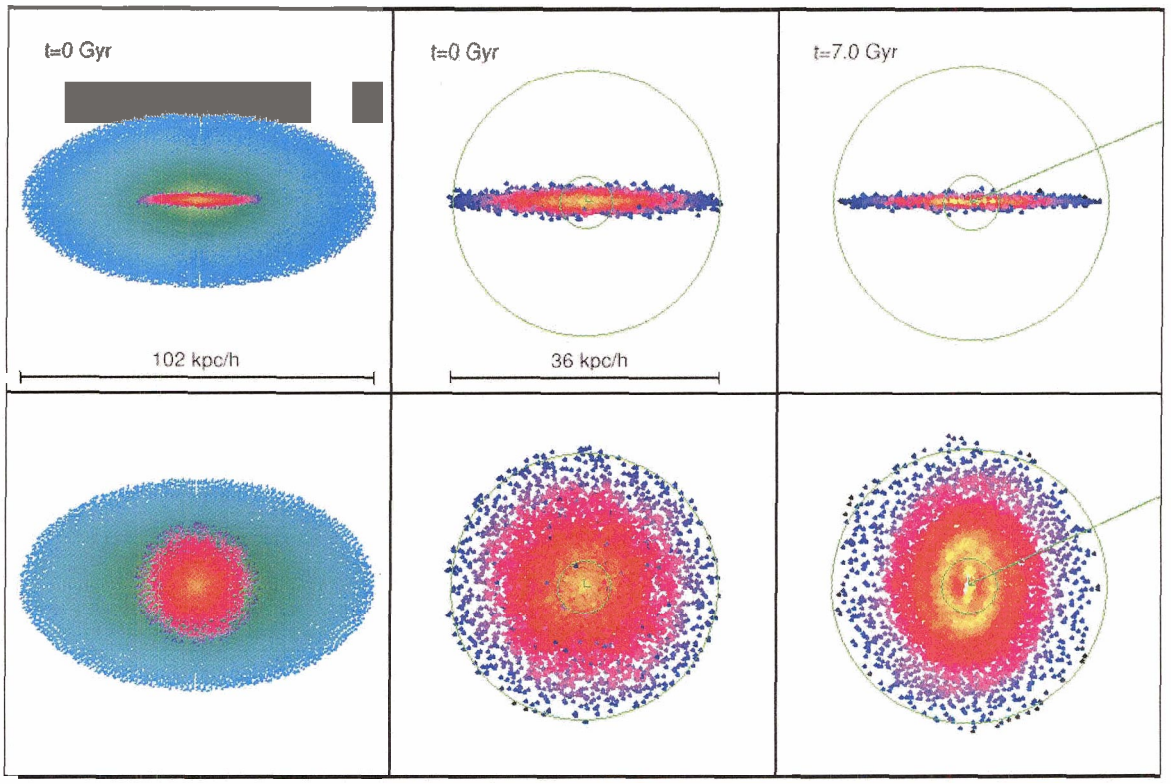

Figure 4.2: Evolution of a massless gaseous disk in the 3D potential of a simulated CDM halo. Upper (lower) panel shows edge-on (face-on) projections of the disk. Left panels shows halo and disk particles at the initial time, color-coded by local dark matter and gas density, respectively. Middle and right panels shows disk particles only at initial time and after 7.0 Gyr, respectively. Inner and outer circles have radii equal to the exponential scale length of the disk, $r_d = 3.6\ h^{-1}$kpc, and the outermost radius of the disk, $r_{\rm outer} = 18.0\ h^{-1}$kpc, at $t = 0$, respectively. The diagonal line in the lower right panel indicates the line-of-sight used to generate the rotation curve in the lower right panel of Figure 4.3. Triaxiality in the halo mass distribution leads to significant evolution in the structure of the disk and to strong deviations from circular symmetry.

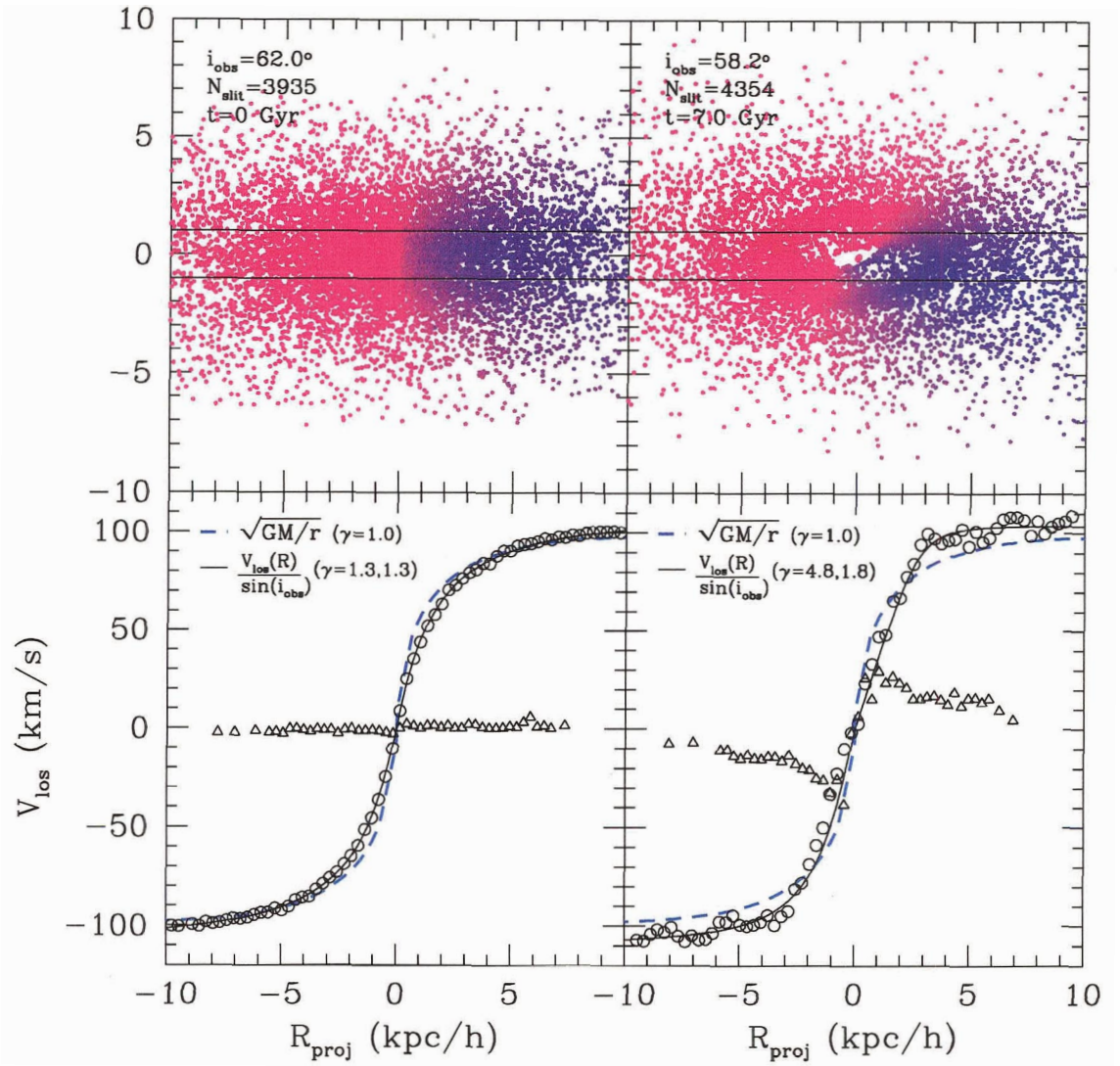

Figure 4.3: Projected image and rotation curves of the simulated disk. Upper panels show the projected positions of the disk particles after the disk has been inclined by 67° relative to the initial plane of the disk. Disk particles are color-coded by line-of-sight velocity. Solid horizontal lines indicate the position of a 2 h^{-1}kpc wide slit oriented along the photometric major axis of the projected disk. Open circles (triangles) in bottom panels show the rotation curve as inferred from simulated long-slit radial velocity data with slit placed across the major (minor) axis of the disk. The major axis rotation curve agrees well initially ($t = 0$) with the V_c profile of the halo (dashed curve) but significant deviations and misalignment of the kinematic and photometric major axes result from the evolution of the disk in the triaxial potential of the halo. A rich variety of rotation curve shapes result, allowing for improved fits to LSB rotation curves (see Figure 4.5).

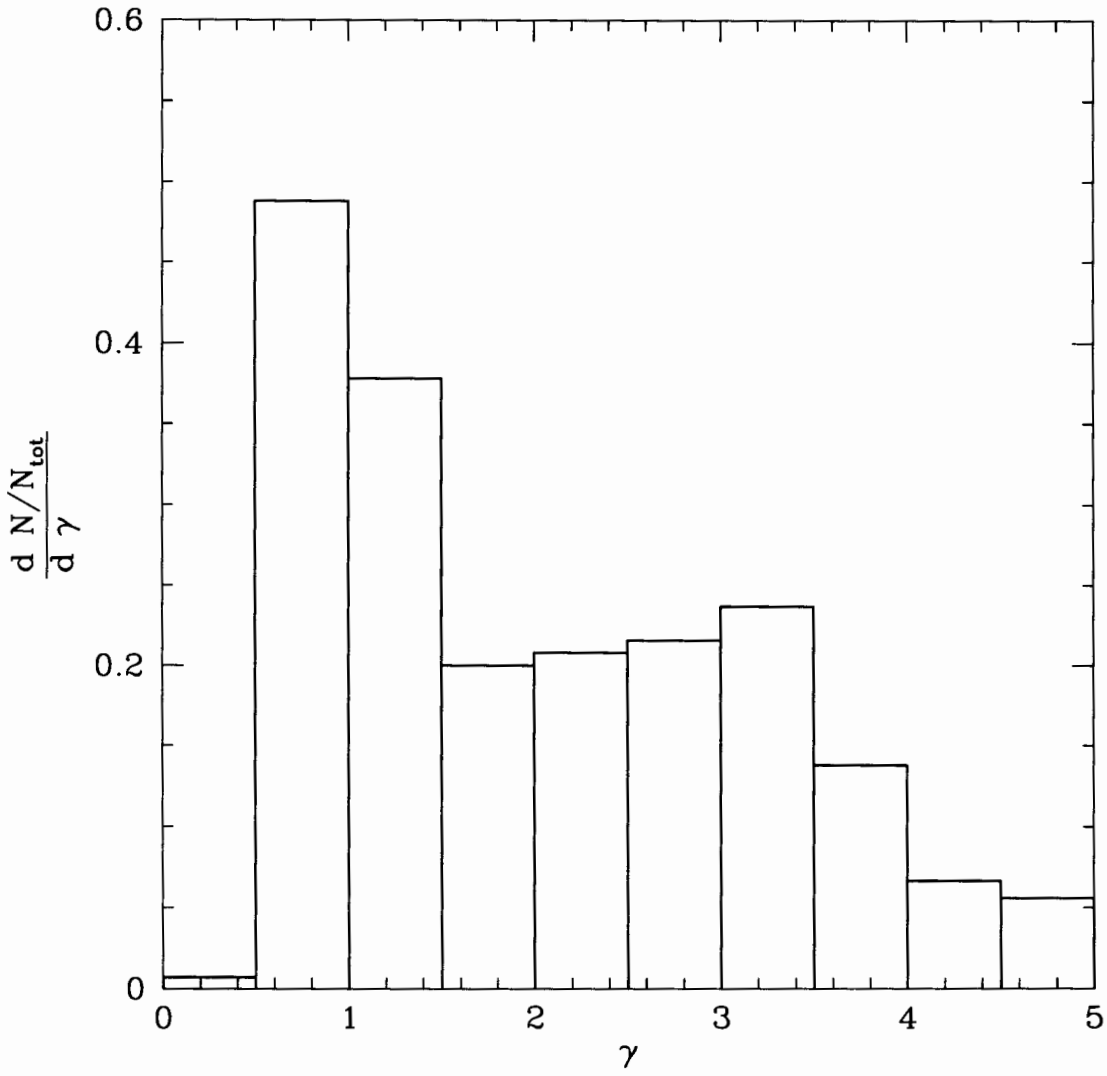

Figure 4.4: Distribution of γ values for rotation curves obtained by observing the simulated disk at time $t = 7.0$ Gyr from 1000 random lines-of-sight. A large fraction of rotation curves have values of γ significantly higher than the initial value of $\gamma = 1.3$.

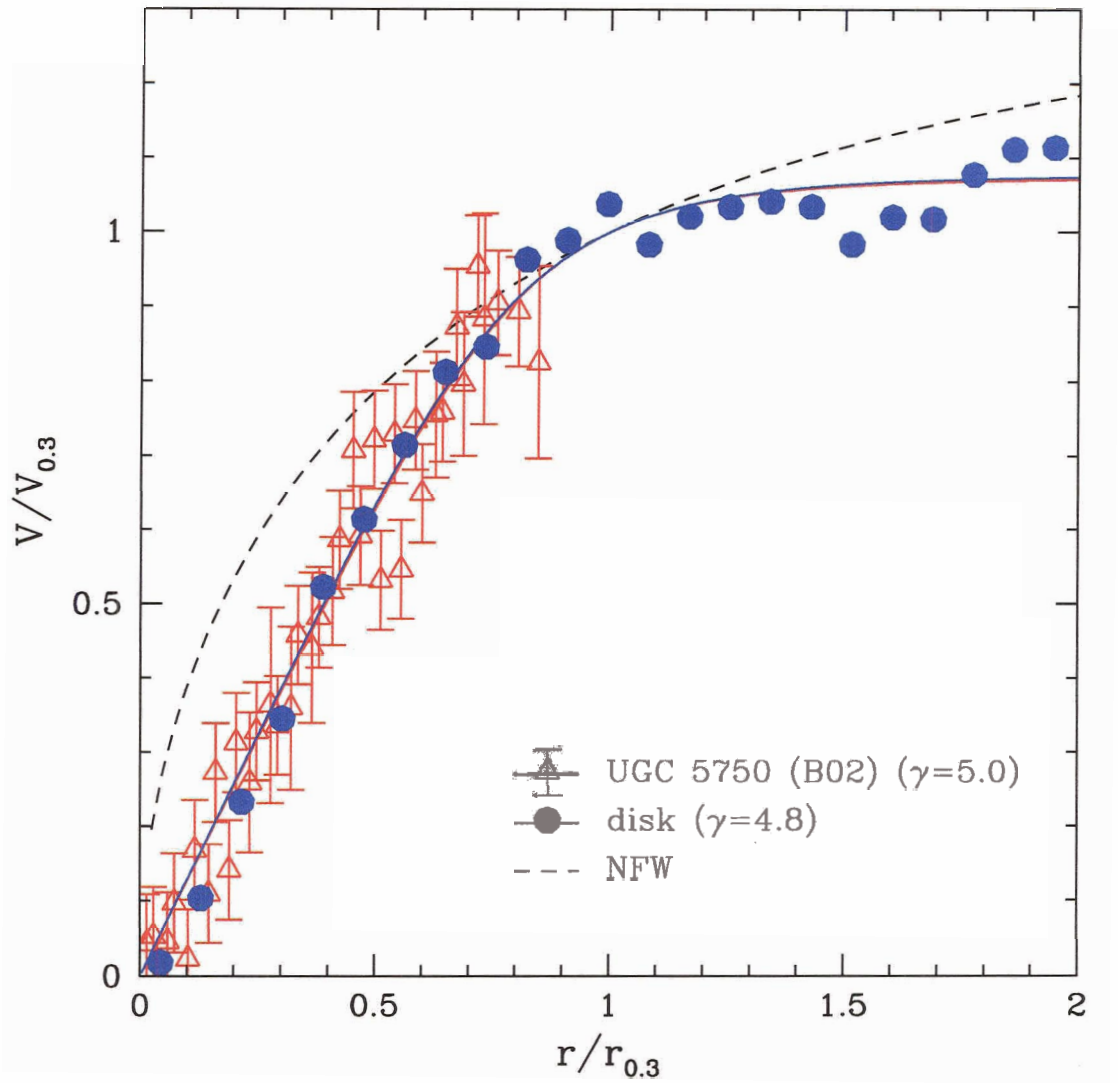

Figure 4.5: Systematic deviations from circular velocity induced by the triaxiality of the halo lead to rotation curve shapes in better agreement with LSBs with high γ. Open circles correspond to rotation curves inferred from simulated long-slit data for the disk shown in Figure 4.3.

Chapter 5

Concluding Remarks

The main conclusion of the work presented in this thesis is that LSB galaxy rotation curves are not manifestly inconsistent with the structure of CDM halos predicted by cosmological simulations. In Chapter 2 we find that only 10% of the LSB rotation curves we examine exhibit the linear rise in velocity with radius that many authors have interpreted as a signature of solid body rotation, i.e., circular motion in a halo with a constant density core. In Chapter 4, however, we show that the kinematics of a disk in a triaxial halo deviate significantly from strictly circular motion; the resulting rotation curve can often resemble that of a disk in solid body rotation. In other words, deviations from spherical symmetry in the shape of the potential can "mask" the presence of a cusp in a triaxial halo.

In Chapter 3, we investigated the structure of simulated CDM halos over a wide range in masses, from dwarf galaxies to galaxy clusters. These simulations confirm that the structure of CDM halos is independent of halo mass and that halos have cuspy density profiles, i.e., the density continues to rise down to the innermost reliably resolved radius. The structure of halos is reasonably well-described by the fitting formula originally proposed by Navarro et al. (1996b, 1997), however, systematic deviations are also evident. In particular, we find no indications of convergence to a

well-defined asymptotic value of the inner slope in the density profiles of our simulated halos. Whether this is borne out by higher resolution simulations remains to be seen, however, the results of the convergence study presented in Chapter 2 indicate that reducing the innermost reliably resolved radius by a factor of 10 will require increasing the halo particle number by a factor of 200 over the highest resolution galaxy-sized halos presented in this thesis. As noted by Stoehr et al. (2003), this is probably unattainable within the next few years, unless radical new techniques are invented. The new fitting formula we propose provides a more accurate description of halo profiles, but we caution that direct comparison between observations and simulations (as opposed to fitting formulae) is preferable whenever possible.

If the density of CDM halos does in fact converge to a finite value at the centre, as suggested by the simulations presented in Chapters 2 and 3, this may represent a significant clue for understanding the origins of cuspy halos. Several attempts to model the formation of the inner density profile have focused on the importance of mergers in building up the central cusp (Syer and White, 1998; Nusser and Sheth, 1999; Subramanian et al., 2000b). In these models, dynamical friction causes merging satellite halos to spiral towards the centre of the host halo and the inner density profile is built up either by tidally stripped material from these satellites (Syer and White, 1998), or by their undigested cores (Subramanian et al., 2000b). These models often predict a dependence of the central density profile on the initial power spectrum of density fluctuations that is not evident in cosmological simulations (Navarro et al., 1997), however, Dekel et al. (2003a,b) show that tidal stripping of a single fairly massive satellite halo can generate a stable inner cusp in an initially cored host halo, a result they claim is independent of the fluctuation power spectrum.

The importance of mergers in the formation of the universal profile has been called into question by simulations in which a cutoff in the initial power spectrum is imposed on small scales, as expected in a universe dominated by warm dark matter (Moore et al., 1999b; Avila-Reese et al., 2001; Bullock et al., 2002). Furthermore,

Huss et al. (1999) conclude from spherical collapse simulations in which the amount of substructure and angular momentum is systematically varied that NFW-like density profiles are a generic prediction of gravitational collapse, independent of the initial conditions and formation history. Subramanian (2000), Subramanian et al. (2000b) and Łokas and Hoffman (2000) use spherical collapse models to derive broad limits on the inner slope expected for collisionless gravitational collapse. Taylor and Navarro (2001) noted recently that the observed phase-space density, ρ/σ^3, of simulated halos closely follows a power law over two decades in radius, in contrast with the density profile which steepens gradually with radius over the same range. Using this as a constraint, these authors present a solution to the spherically symmetric and isotropic Jeans equation which closely follows the density profile of simulated halos and asymptotically approaches $\rho \propto r^{-0.75}$ at small radii. Why the phase-space density should obey a power law in radius remains a mystery, however.

The vast majority of numerical and analytical studies have concluded that cuspy halos are a robust prediction of structure formation CDM-dominated universe. A notable exception is the work of Weinberg (2001a,b) who suggests that noise due to transient perturbations, such as substructure halos on decaying orbits, can excite resonant modes which drive the evolution of the halo toward a density profile with a flat inner core. This author contends that Poisson noise on small scales in N-body simulations can smear out resonance structure, even in simulations with large ($N \simeq 10^6$) numbers of particles. If so, future generations of N-body simulations may converge to a far different halo density profile than the cuspy profiles presented in this thesis and in previous numerical studies. However, Dekel et al. (2003b) argues that even if Weinberg is correct about this resonant behaviour, it may not be relevant in real galaxies, where baryonic structures are likely to introduce clumpiness at level comparable to the granularity in current N-body simulations.

In a related series of papers, Weinberg and Katz (2002) and Holley-Bockelmann et al. (2003) explore the evolution of a halo due to a rotating bar in an embedded disk.

Using low-noise N-body simulations performed using self-consistent field methods, these authors find that a Lindblad-like resonance couples the rotating bar to halo particle orbits in the central cusp, rapidly flattening it. Holley-Bockelmann et al. (2003) find that a bar triggered by an external quadrupole potential sweeps out a constant density core. Although this core is typically an order of magnitude smaller than those suggested by rotation curves, they argue that satellite encounters and/or multiple epochs of bar formation can result in the formation of much larger bars and subsequently, much larger cores. In contrast, Sellwood (2003) finds that a disk grown adiabatically within a cuspy halo naturally develops a bar that is too short to produce a core of any significant size. The efficacy of bar-induced evolution of dark matter cusps remains an open question that continues to be hotly debated in the literature.

Supermassive black holes might also play a role in disrupting a central cusp. The simulations of Merritt and Cruz (2001) show that black holes at the centres of two merging galaxies can eject enough material to convert an r^{-1} cusp into a shallower, $r^{-0.5}$ cusp. Similarly, Milosavljević and Merritt (2001) find that the merger of two systems containing supermassive black holes results in the formation of a hard binary black hole that transfers enough energy to the surrounding material to shallow the cusp within a radius that contains several times its mass. These authors point out that this is probably not applicable to LSB and dwarf galaxies since there is no evidence for supermassive black holes in these galaxies; the black hole mass predicted for such galaxies by the correlation between black hole mass and stellar velocity dispersion (Ferrarese and Merritt, 2000; Gebhardt et al., 2000) is much less than the "missing cusp mass" implied by their rotation curves.

Another possibility was recently suggested by El-Zant et al. (2001) to explain the shallow dark matter density profiles recently derived by Tyson et al. (1998); Sand et al. (2004) for several galaxy clusters based on constraints from strong gravitational lensing. These authors propose a scenario in which gas cools radiatively and collapses in the potential wells of dark matter halos, forming highly concentrated baryonic cores

as envisaged by White and Rees (1978) and confirmed by N-body/gasdynamical simulations (see, e.g., Katz et al., 1992, 1996). These tightly bound knots of gas are overdense with respect to the dark matter, and are therefore much more resistant to tidal disruption as they spiral towards the centre of the host halo via dynamical friction. El-Zant et al. (2001) and El-Zant et al. (2004) show that these concentrated satellites lose enough orbital energy to the dark matter to heat up and flatten the central cusp. As a result, their model predicts a core-like structure for the inner dark matter density profile of the cluster, but a galaxy distribution that is stepper than the original NFW-like cusp. While this model may help to explain the possible discrepancy between the predictions of CDM and lensing observations of galaxy clusters, it may not apply to the dark matter halo of a galaxy since most subhalos on these scales apparently do not contain a significant amount of baryons, as evidenced by the paucity of observable dwarf satellite galaxies in the Local Group (Klypin et al., 1999; Moore et al., 1999a). In the absence of a concentrated baryonic core, subhalos will be tidally disrupted before they reach the central cusp (Hayashi, 2001), and will therefore be unable to significantly heat up the central cusp.

Navarro et al. (1996a) investigated the possibility that sudden mass loss due to supernova-driven winds could result in the formation of a core in an initially cuspy dark matter density profile. These authors simulated the gravitational effect of a sudden mass outflow by instantaneously removing the potential of an exponential disk grown adiabatically within a cuspy halo. The size of the flattened core produced depends on the mass and size of the outblown disk, and Navarro et al. (1996a) show that one can reproduce the rotation curves of dwarf galaxies with a relatively weak perturbation due to the loss of a disk of mass and size consistent with observational constraints. Gnedin and Zhao (2002) revisited this scenario, however, and find that although a sudden outflow reduces the inner density of the halo, the effect is not strong enough to produce a core as large as those implied by dwarf rotation curves. The disagreement between the two groups might stem from the fact that the simulations

of Gnedin and Zhao (2002) are one-dimensional, albeit of higher resolution than the three-dimensional simulations of Navarro et al. (1996a).

Finally, the work of Stoehr et al. (2002, 2003) suggests that the inner density profile of substructure halos can become significantly shallower as they orbit in the potential of a more massive host halo. These authors find the circular velocity profiles of subhalos are well fit by a parabolic fitting formula whose corresponding density profile becomes shallower with decreasing radius. As noted in Chapter 3, their fitting formula reaches a flat slope at a finite radius and the density actually begins to decrease if one extrapolates their fitting formula to smaller radii, indicating that the formula may not be valid close to the halo centre. Nevertheless, fits to the subhalo profiles indicate that tidal heating can make the central cusp shallower. Stoehr (2004) shows that the circular velocity profile of a highly stripped subhalo provides a good match to an LSB rotation curve with a high value of γ taken from the sample presented in Chapter 2. But he also points out that these galaxies appear to be isolated systems which are not obviously subject to strong tidal fields that might alter their inner density structure.

Clearly there is no shortage of ideas for ways to reconcile the cusp-core discrepancy. All of the proposals described above rely on physical mechanisms for flattening the inner cusp. The scenario we present in Chapter 4 is closer in spirit to the proposal of Rhee et al. (2003), who use N-body simulations and tilted-ring fitting models to investigate the effects of stellar disks with bars and bulges on rotation curves. These authors find that bars generate non-circular motions and random velocities in the stellar disk which can cause the circular velocity to be significantly underestimated, sometimes resulting in the false inference that the density profile of the halo flattens near the centre. Rhee et al. (2003) argue that signatures of bars can be difficult to detect in the surface brightness profiles of galaxies, thereby explaining why many LSB galaxies with "core-like" rotation curves do not appear to be barred galaxies.

Which, if any, of these proposals turns out to be the correct solution to the cusp-

core discrepancy, is a question that will be answered only by careful analysis of galaxy kinematics and comparison with the detailed predictions of theoretical models. The results presented in Chapter 4 regarding the effect of a triaxial halo on the kinematics of a galactic disk are suggestive, but by no means conclusive. The halo required to significantly alter the kinematics from circular motion is significantly triaxial with axis ratios of 0.5:0.6:1.0. In comparison, Bullock et al. (2001) finds the average short-to-long axis ratio of galaxy-sized halos in cosmological simulations to be 0.70 ± 0.17, albeit with a significant tail of highly flattened halos. This might explain why only a small minority of LSB rotation curves are clearly inconsistent with the spherically-averaged circular velocity profiles of CDM halos. In order to support this hypothesis, we plan to conduct many additional simulations of disks in a sample of halos with a realistic distribution of shapes. We also intend to use non-static halo potentials, i.e., halos made up of "live" N-body particles, halos containing substructure, and self-gravitating disks to further investigate the structure and evolution of disks in a realistic cosmological context.

Recently, several groups have presented two-dimensional velocity fields for disk galaxies observed with fibre-array fed spectrographs (Bolatto et al., 2001, 2002; Swaters et al., 2003b; Simon et al., 2003), millimetre wavelength interferometers (Bolatto et al., 2001, 2002; Simon et al., 2003), and Fabry-Perot interferometers (Beauvais and Bothun, 1999; Blais-Ouellette et al., 2001). Rotation curves derived from these data do not suffer from many of the systematic uncertainties such as slit positioning errors that afflict long slit rotation curve studies (Simon et al., 2003). We intend to compare directly the rotation curves derived from the two-dimensional line-of-sight velocity fields of simulated and observed disk galaxies using tilted ring-fitting algorithms like those developed by Simon et al. (2003). Since full three-dimensional position and velocity information is available for both the dark matter and baryonic components of simulated galaxies, this will lead to a better understanding of the systematic errors involved in inferring the distribution of dark matter from tilted ring model fits to

two-dimensional velocity field data. Consequently, this might lead to more effective algorithms for the analysis of two-dimensional velocity data and, ultimately, more reliable estimates as to how accurately one can determine the structure of dark matter halos from observations of disk galaxy kinematics given the degeneracy between the orientation, shape and structural parameters of both the disk and halo components.

Appendix A

LSB Galaxy Properties and Images

Table A.1: Properties of LSB galaxies

Galaxy ID	M_R (mag)	h (kpc)	$\mu_{0,R}$ ($\frac{\text{mag}}{\text{arcsec}^2}$)	i (°)	D (Mpc)	L_R ($L_\odot$)
McGaugh et al. (2001, M01):						
ESO014-0040	-22.5[a]	–	–	35	212	6.19×10^{10}
ESO084-0411	-19.0[a]	–	–	90	80	2.47×10^{9}
ESO120-0211	-16.5[a]	–	–	70	15	2.47×10^{8}
ESO187-0510	-17.4[a]	–	–	58	18	5.65×10^{8}
ESO206-0150	-20.1[a]	–	–	39	60	6.79×10^{9}
ESO302-0120	-20.0[a]	–	–	55	69	6.19×10^{9}
ESO305-0090	-18.2[a]	–	–	53	11	1.18×10^{9}
ESO425-0180	-21.4[a]	–	–	33	86	2.25×10^{10}
ESO488-0490	-17.7[a]	–	–	63	22	7.45×10^{8}
F563-1	-18.2[a]	2.8[a]	22.7[a]	25	42	1.18×10^{9}
F568-3	-19.2[a]	4.0[a]	22.2[a]	40	77	2.96×10^{9}
F571-8	-18.5	5.2	23.0	90	48	1.56×10^{9}
F579-V1	-19.7	5.1	21.9	26	85	4.70×10^{9}
F583-1	-17.4[a]	1.6[a]	23.2[a]	63	32	5.65×10^{8}
F583-4	-17.8	2.7	22.9	55	49	8.17×10^{8}
F730-V1	-19.0	–	–	50	144	1.42×10^{2}
UGC4115	-13.3	–	–	74	3.2	1.29×10^{7}
UGC5750	-19.6	5.6	22.6	64	56	4.29×10^{9}
UGC6614	-21.2[a]	8.1[a]	22.5[a]	36	85	1.87×10^{10}
UGC11454	-19.5	–	–	64	91	3.91×10^{9}
UGC11557	-20.9[a]	–	–	36	22	1.42×10^{10}
UGC11583	-14.9	–	–	83	5	5.65×10^{7}
UGC11616	-21.2	–	–	60	73	1.87×10^{10}
UGC11648	-21.9	–	–	90	48	3.56×10^{10}
UGC11748	-23.8	–	–	78	73	2.05×10^{11}
UGC11819	-21.2	–	–	66	60	1.87×10^{10}
de Blok and Bosma (2002, B02):						
DDO47	-14.9[a]	1.0[a]	–	30	4	5.65×10^{7}
DDO52	-13.8[a]	0.6[a]	–	60	5.3	2.05×10^{7}
DDO64	-14.7[a]	1.2[a]	–	60	6.1	4.70×10^{7}
DDO185	-15.7	1.2	23.2	80	5.1	1.18×10^{8}
DDO189	-16.2	1.2	22.6	44	12.6	1.87×10^{8}
IC2233	-17.7	2.3	22.5	90	10.5	7.45×10^{8}

continued on next page

continued from previous page

Galaxy ID	M_R (mag)	h (kpc)	$\mu_{0,R}$ ($\frac{\text{mag}}{\text{arcsec}^2}$)	i (°)	D (Mpc)	L_R ($L_\odot$)
F563-1	-18.0	3.5	22.6	25	45	9.82×10^8
NGC100	-17.7[a]	–	–	89	11.2	7.45×10^8
NGC1560	-15.9[a]	1.3[a]	23.2[a]	82	3	1.42×10^8
NGC2366	-16.9	1.5	22.6	59	3.4	3.56×10^8
NGC3274	-16.7	0.5	20.2	64	6.7	2.96×10^8
NGC4395	-18.1	2.3	22.2	46	3.5	1.08×10^9
NGC4455	-16.9	0.7	20.8	78	6.8	3.56×10^8
NGC5023	-17.2	0.8	20.9	90	4.8	4.70×10^8
UGC628	-19.2	4.7	22.1	56	65	2.96×10^9
UGC711	-17.7[a]	–	–	90	26.4	7.45×10^8
UGC731	-16.6	1.7	23.0	57	8	2.70×10^8
UGC1230	-19.1	4.5	22.6	22	51	2.70×10^9
UGC1281	-16.2	1.7	22.7	90	5.5	1.87×10^8
UGC3137	-18.7	2	23.2	90	18.4	1.87×10^9
UGC3371	-17.7	3.1	23.3	49	12.8	7.45×10^8
UGC4173	-17.8	4.5	24.3	40	16.8	8.17×10^8
UGC4325	-18.1	1.6	21.6	41	10.1	1.08×10^9
UGC5005	-18.6	4.4	22.9	41	52	1.71×10^9
UGC5750	-19.5	5.6	22.6	64	56	3.91×10^9
UGC10310	-17.9	1.9	22	34	15.6	8.95×10^8
Swaters et al. (2003a, S03):						
F563-V2	-19.0[a]	2.1[a]	21.3[a]	29	61	2.47×10^9
F568-1	-18.9	4.41	22.7	26	85	2.25×10^9
F568-3	-19.2	4.48	22.4	40	77	2.96×10^9
F568-v1	-18.7	3.96	22.7	40	80	1.87×10^9
F574-1	-19.2	4.24	22.2	65	96	2.96×10^9
UGC731	-16.6	1.65	20.3	57	8	2.70×10^8
UGC2259	-17.8[b]	1.29[b]	21.2[b]	41	9.8	8.17×10^8
UGC4325	-18.1	1.63	21.6	41	10.1	1.08×10^9
UGC4499	-17.8	1.49	21.5	50	13	8.17×10^8
UGC5721	-16.6	0.45	20.2	61	6.7	2.70×10^8
UGC8490	-17.3	0.66	20.5	50	4.9	5.15×10^8
UGC11557	-19.7	3.1	21.0	94	15.9	4.70×10^9
UGC11707	-18.6	4.3	23.1	57	25.1	1.71×10^9
UGC11861	-20.8	6.06	21.4	39	13.2	1.29×10^{10}
UGC12732	-18.0	2.21	22.4	14	96	9.82×10^8

continued on next page

continued from previous page

Galaxy ID	M_R (mag)	h (kpc)	$\mu_{0,R}$ ($\frac{\text{mag}}{\text{arcsec}^2}$)	i (°)	D (Mpc)	L_R ($L_\odot$)

Note. — (1) Name of galaxy, (2) absolute R-band magnutude, (3) scale length, (4) central surface brightness in R-band, (5) inclination, (6) distance, based on a Hubble constant of 75 $\text{km}\,\text{s}^{-1}\text{Mpc}^{-1}$, (7) R-band luminosity. Data taken from tables in McGaugh et al. (2001), de Blok and Bosma (2002), and Swaters et al. (2003a), respectively.

[a] Converted from B-band observations assuming $B - R = 0.9$.

[b] Converted from I-band observations assuming $R - I = 0.5$.

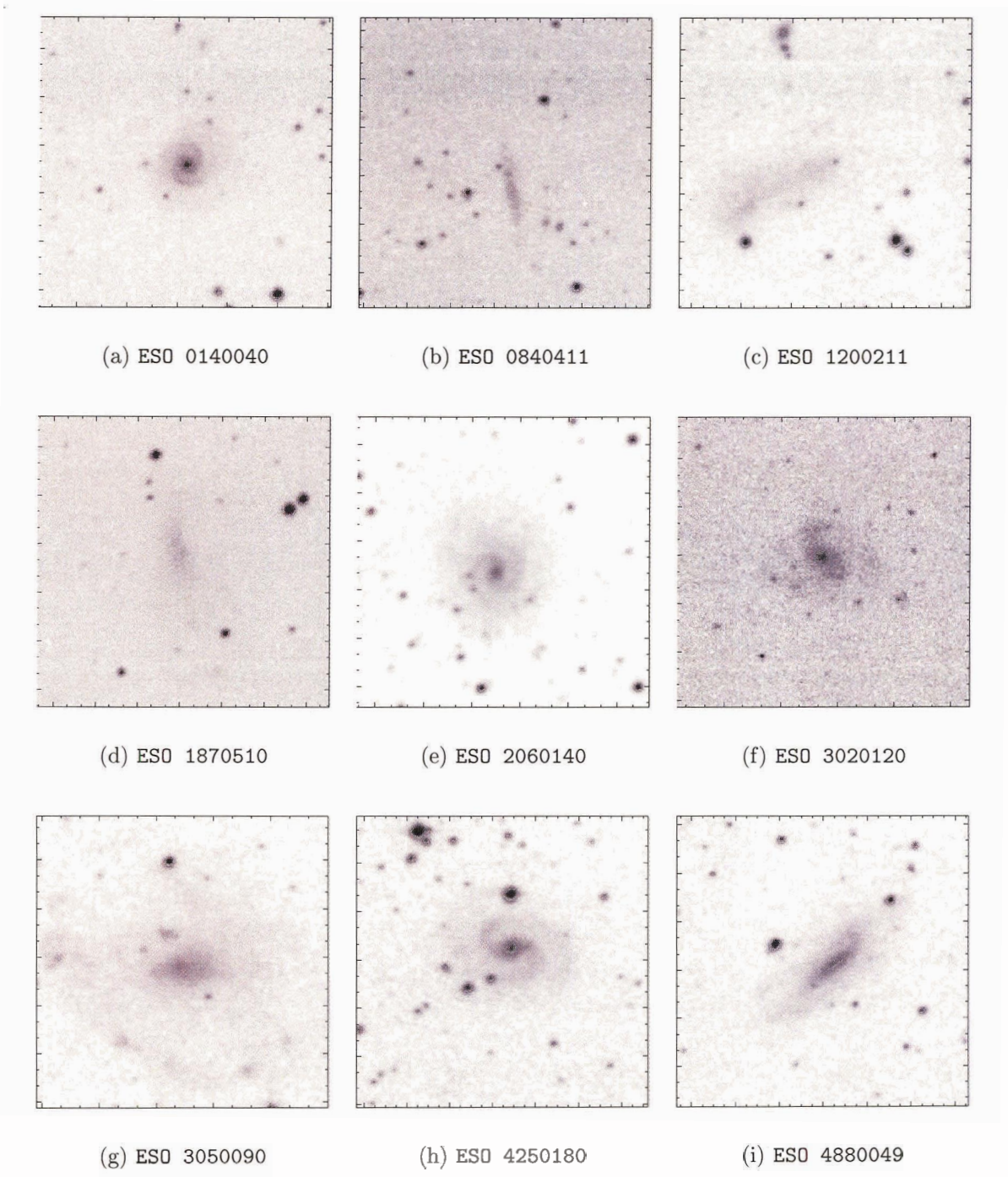

(a) ESO 0140040 (b) ESO 0840411 (c) ESO 1200211

(d) ESO 1870510 (e) ESO 2060140 (f) ESO 3020120

(g) ESO 3050090 (h) ESO 4250180 (i) ESO 4880049

Figure A.1: R-band images ($3' \times 3'$) of LSB galaxies taken from the Second Generation Digitized Sky Survey (see `http://cadcwww.hia.nrc.ca/cadcbin/getdss`).

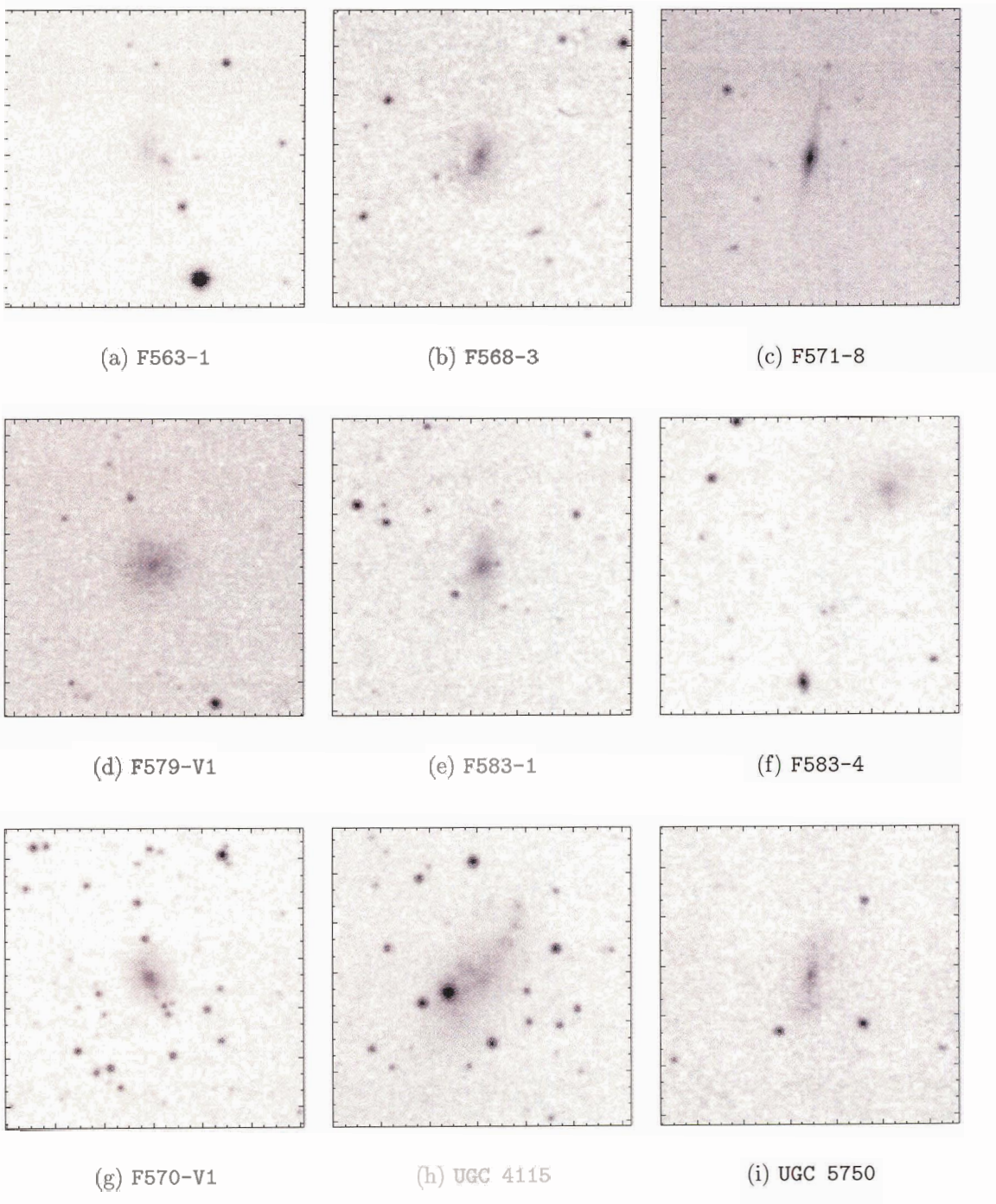

(a) F563-1 (b) F568-3 (c) F571-8

(d) F579-V1 (e) F583-1 (f) F583-4

(g) F570-V1 (h) UGC 4115 (i) UGC 5750

Figure A.2: Same as Figure A.1.

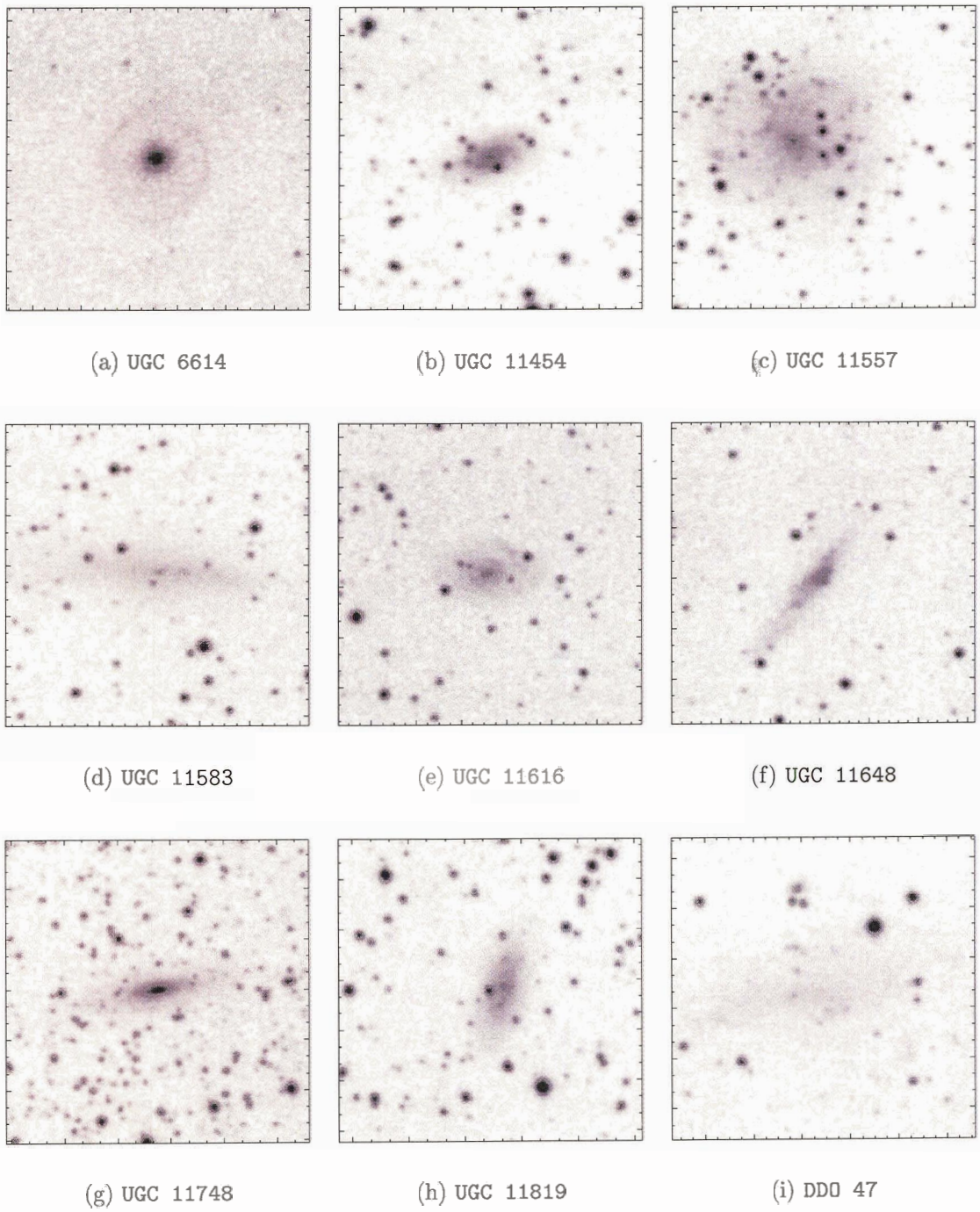

(a) UGC 6614 (b) UGC 11454 (c) UGC 11557

(d) UGC 11583 (e) UGC 11616 (f) UGC 11648

(g) UGC 11748 (h) UGC 11819 (i) DDO 47

Figure A.3: Same as Figure A.1.

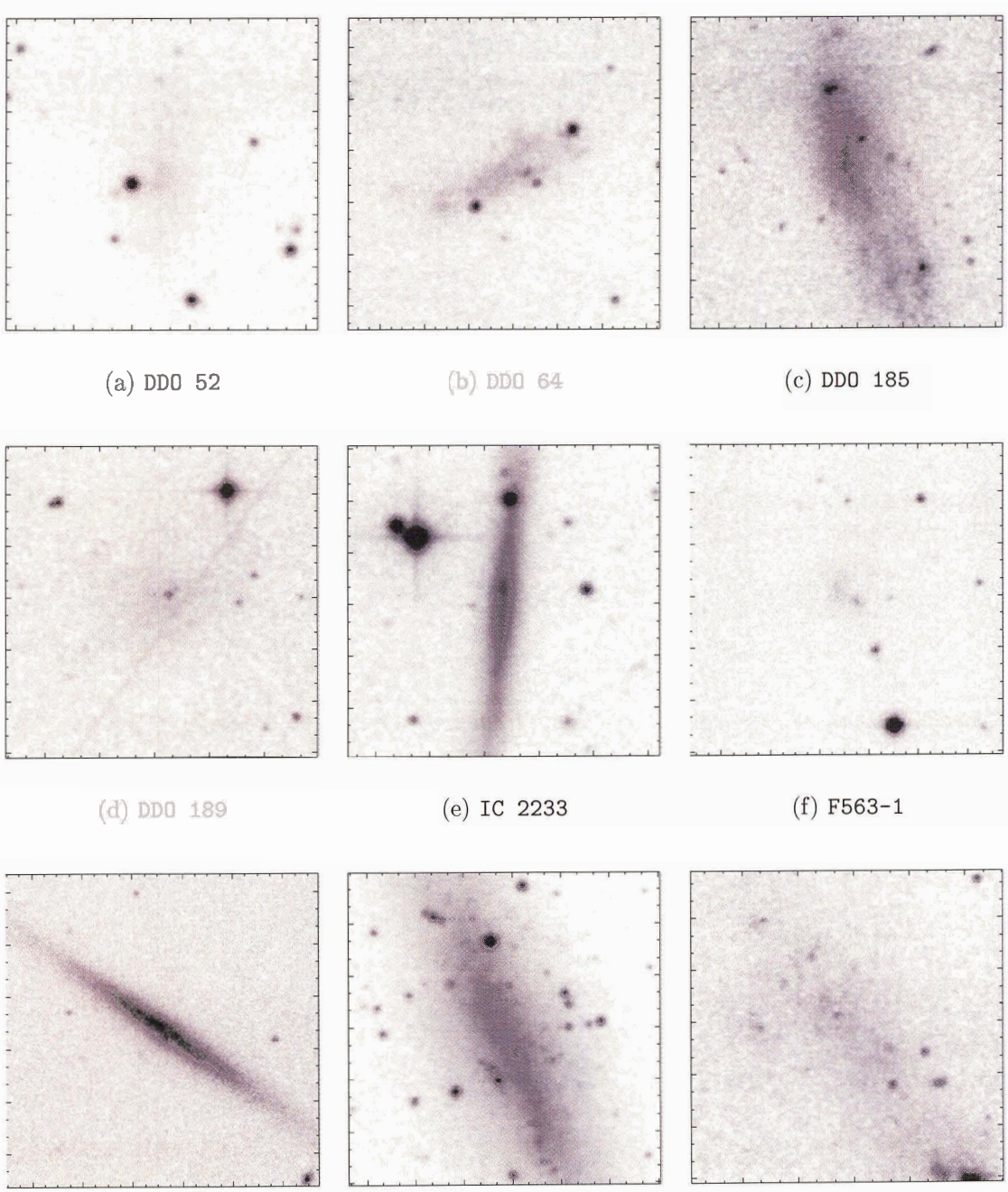

(a) DDO 52 (b) DDO 64 (c) DDO 185

(d) DDO 189 (e) IC 2233 (f) F563-1

(g) NGC 100 (h) NGC 1560 (i) NGC 2366

Figure A.4: Same as Figure A.1.

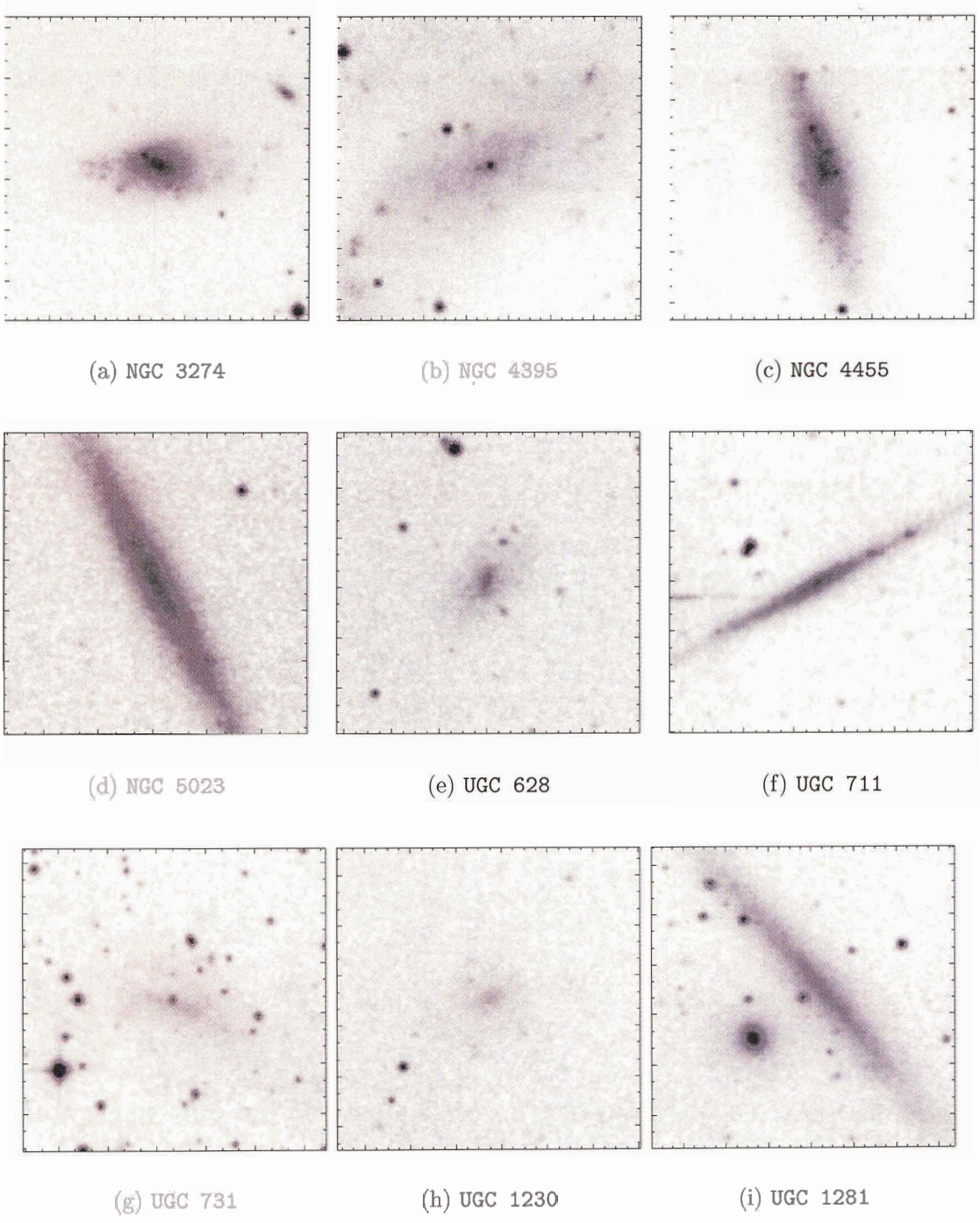

(a) NGC 3274 (b) NGC 4395 (c) NGC 4455

(d) NGC 5023 (e) UGC 628 (f) UGC 711

(g) UGC 731 (h) UGC 1230 (i) UGC 1281

Figure A.5: Same as Figure A.1.

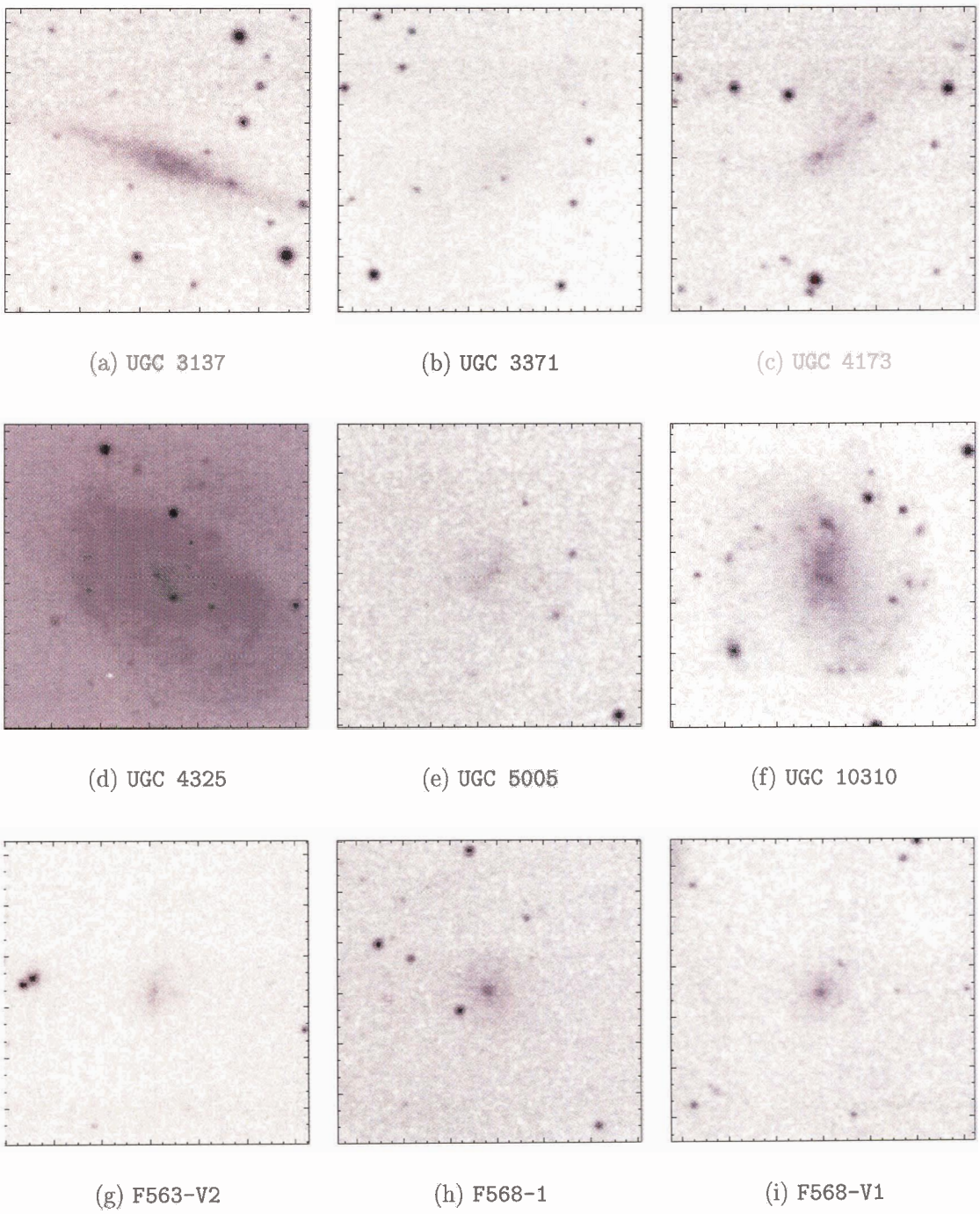

(a) UGC 3137 (b) UGC 3371 (c) UGC 4173

(d) UGC 4325 (e) UGC 5005 (f) UGC 10310

(g) F563-V2 (h) F568-1 (i) F568-V1

Figure A.6: Same as Figure A.1.

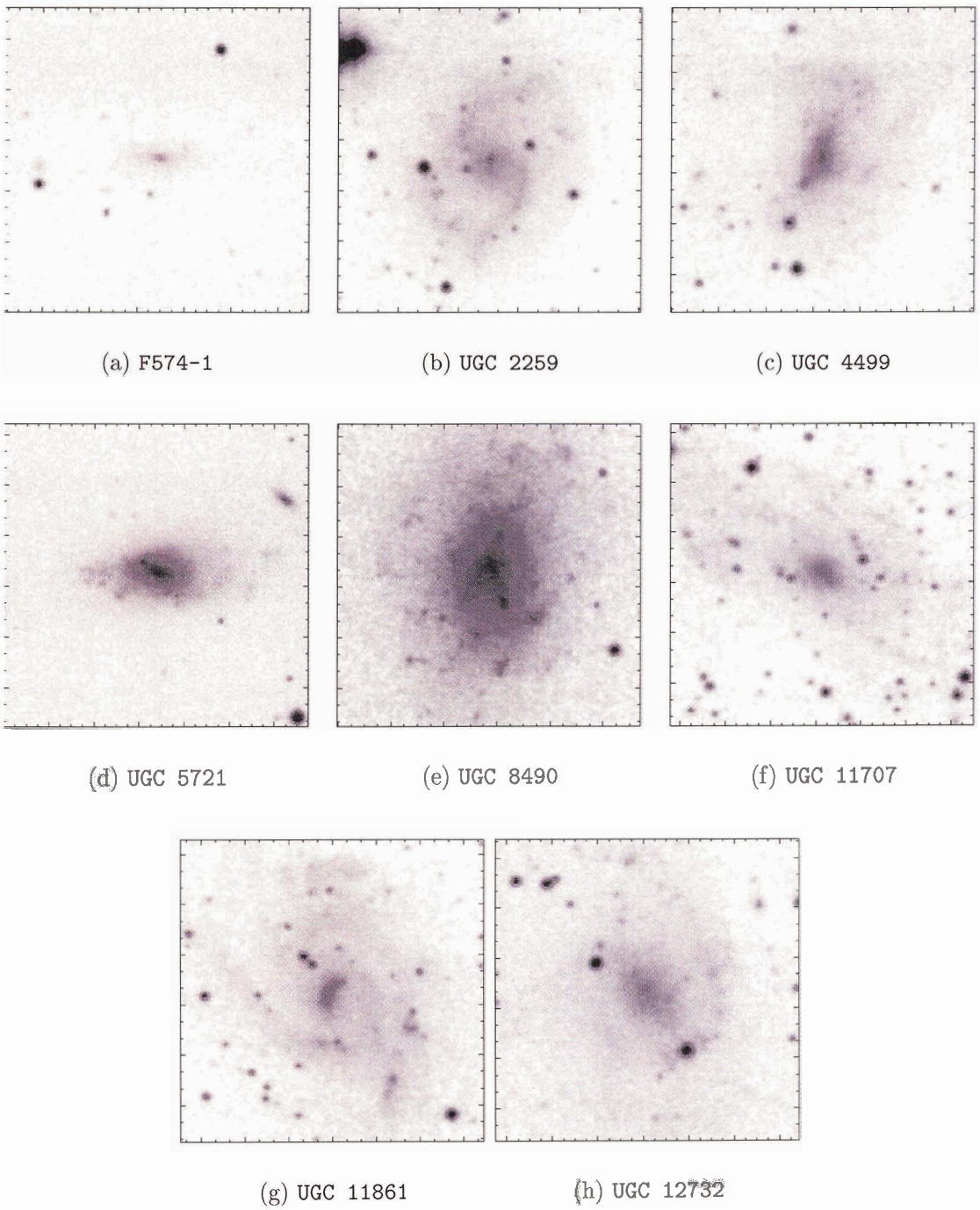

(a) F574-1 (b) UGC 2259 (c) UGC 4499

(d) UGC 5721 (e) UGC 8490 (f) UGC 11707

(g) UGC 11861 (h) UGC 12732

Figure A.7: Same as Figure A.1.

Appendix B

LSB Rotation Curve Fits

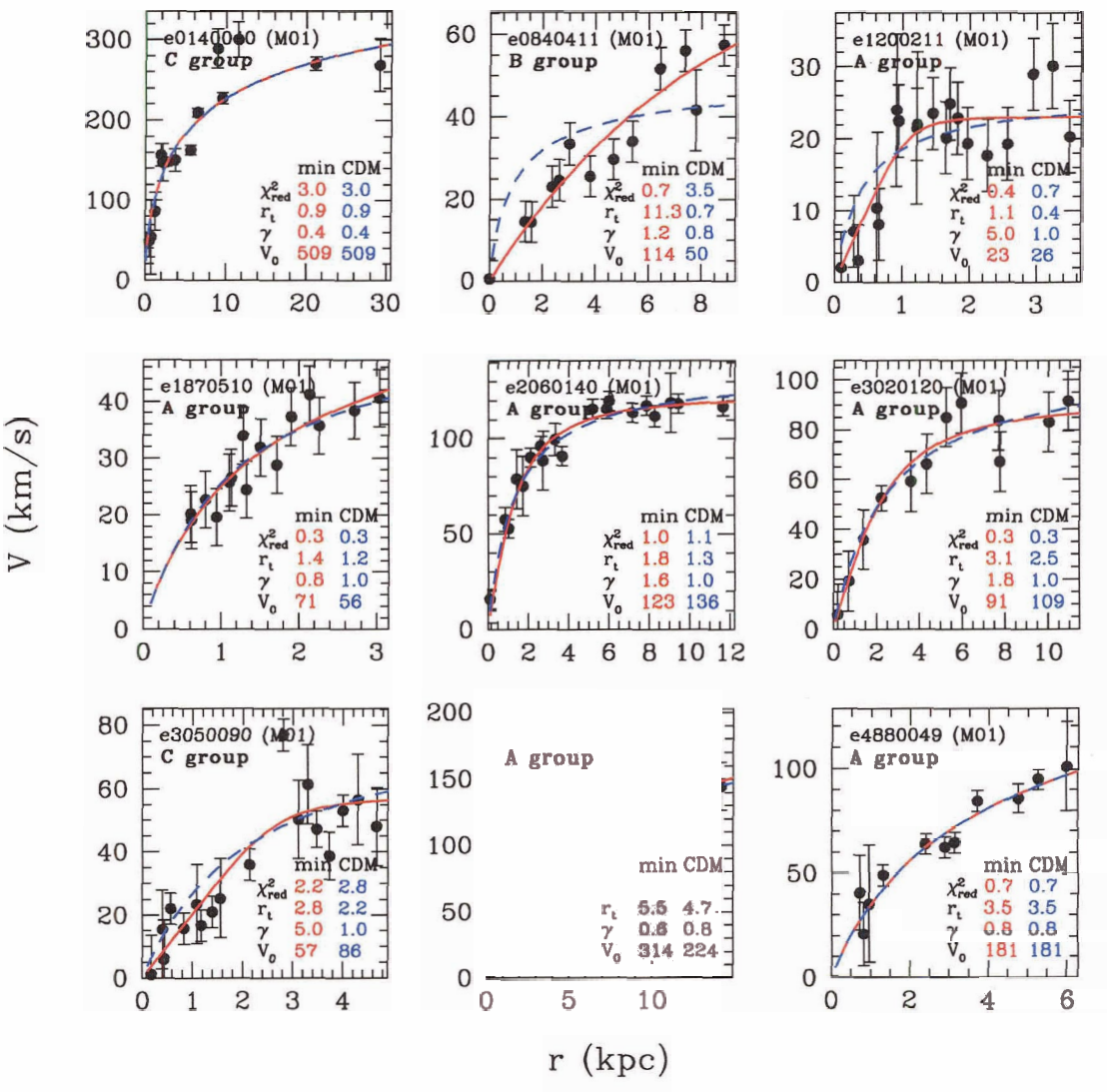

Figure B.1: Hα rotation curves of LSB galaxies from the sample of McGaugh et al. (2001, M01) (first of three figures). Solid curves show best fits using the multi-parameter fitting formula given by eq. 2.8 with fit parameters and χ^2_{red} values listed under "min" column in each panel. Dashed curves show the best fits which can be obtained with ΛCDM-compatible parameters, listed under "CDM" column. Rotation curves are labelled with χ^2 groups A, B, and C, as defined in Figure 2.17.

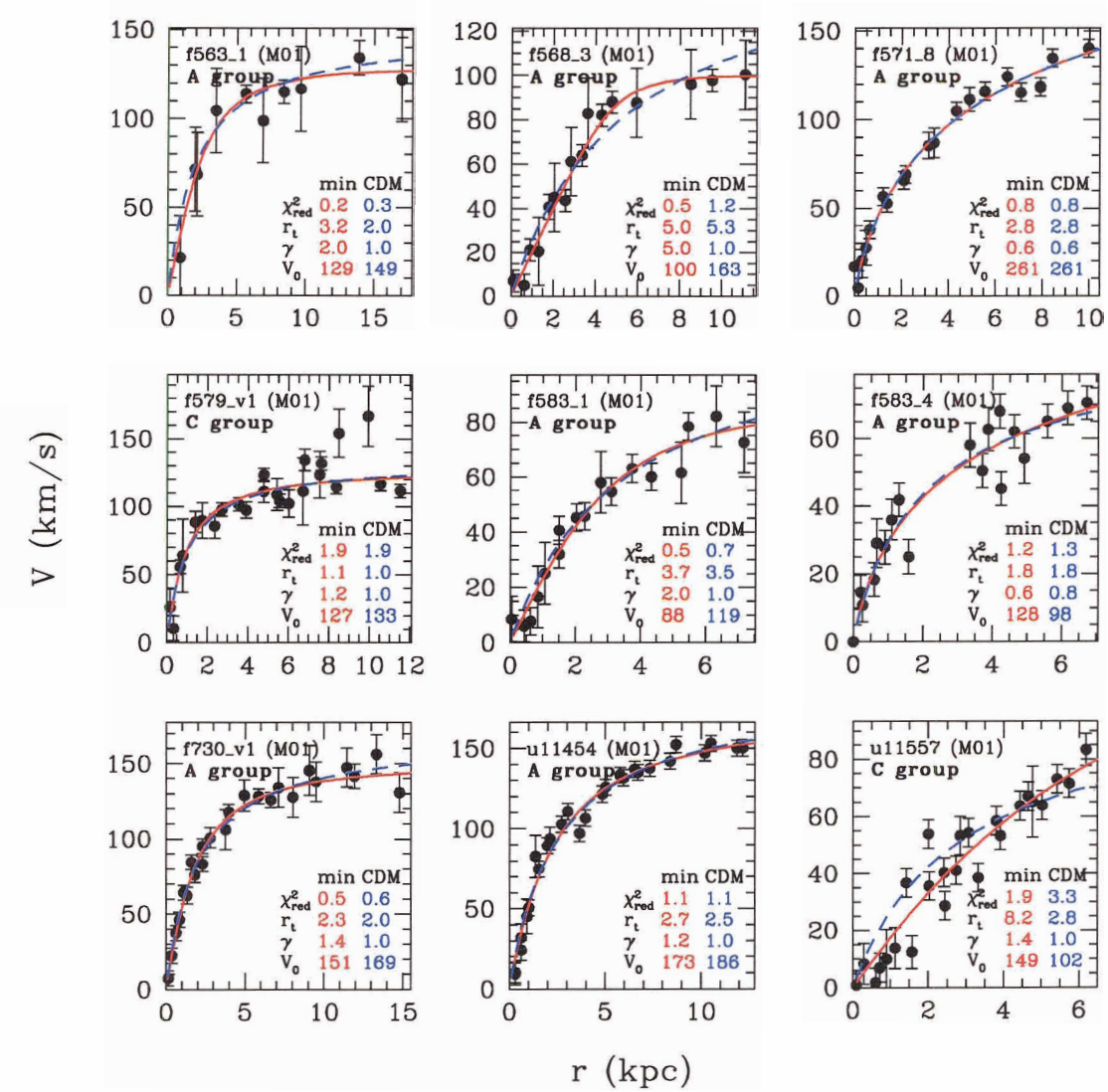

Figure B.2: e
q. 2.8 for McGaugh et al. (2001) sample (second of three figures)] same as Figure B.1 (second of three figures).

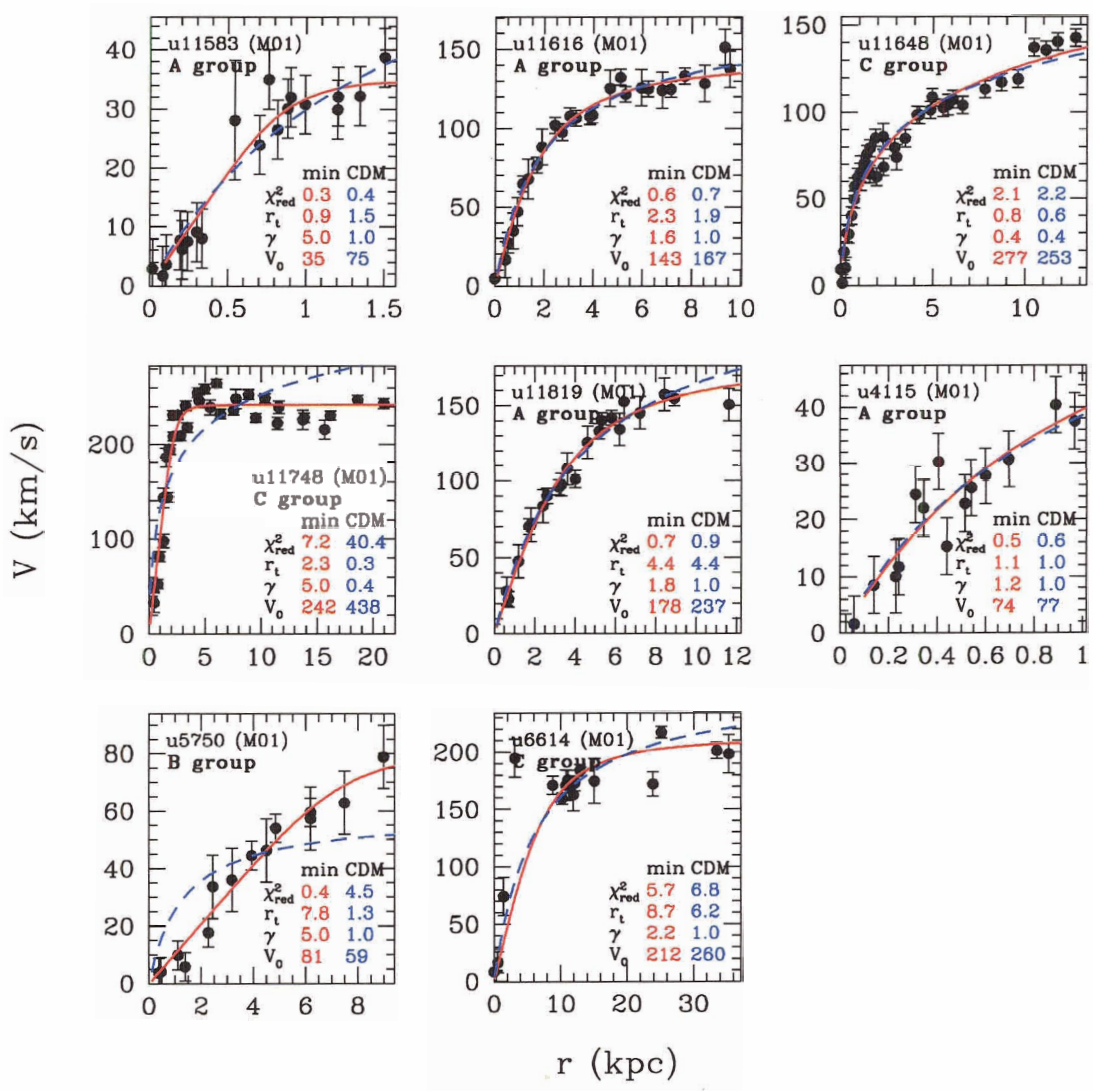

Figure B.3: e
q. 2.8 for McGaugh et al. (2001) sample (third of three figures)] same as Figure B.1 (third of three figures).

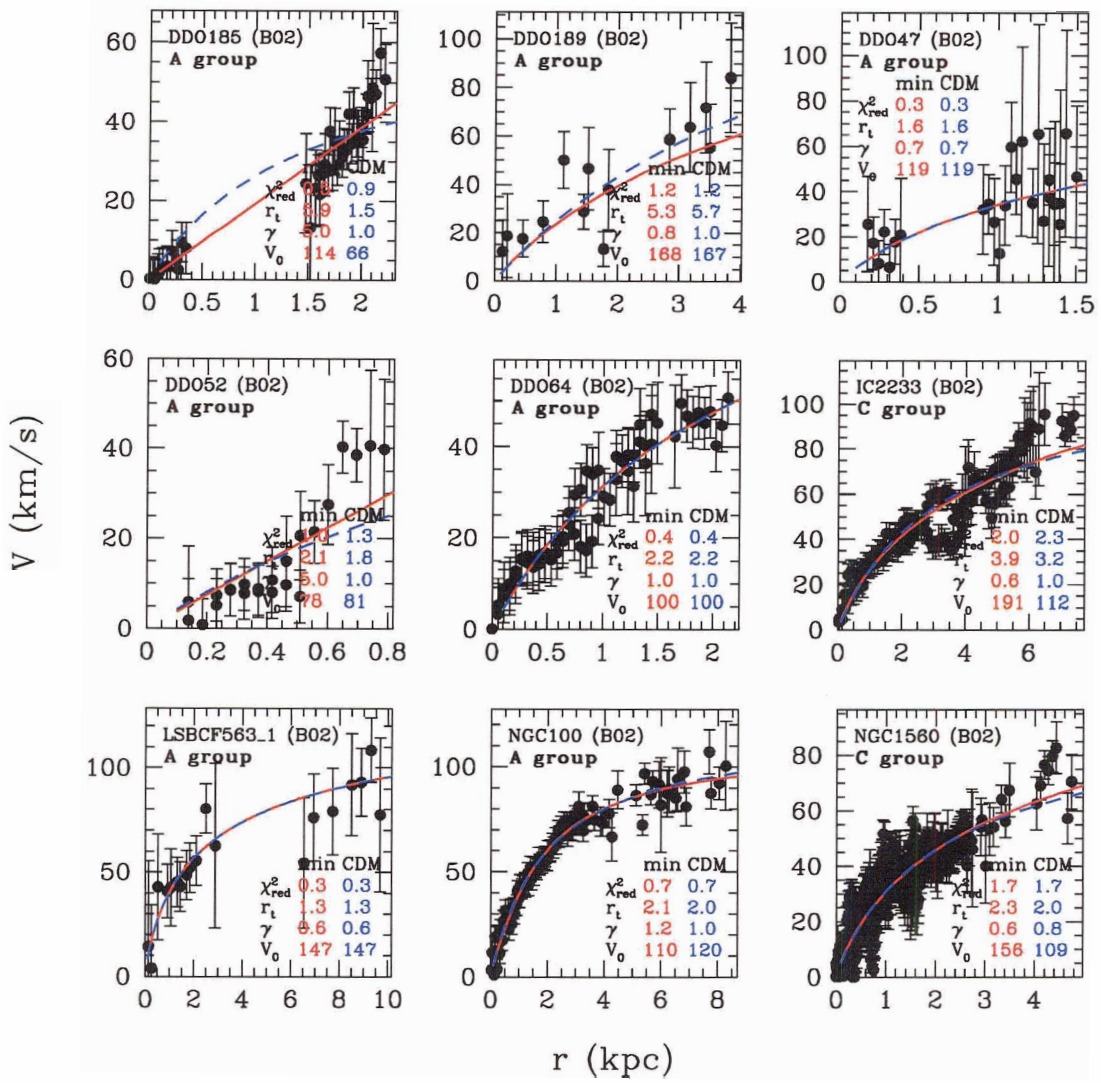

Figure B.4: e
q. 2.8 for de Blok and Bosma (2002) sample (first of three figures)] same as Figure B.1 but for LSB galaxies from the sample of de Blok and Bosma (2002, B02) (first of three figures).

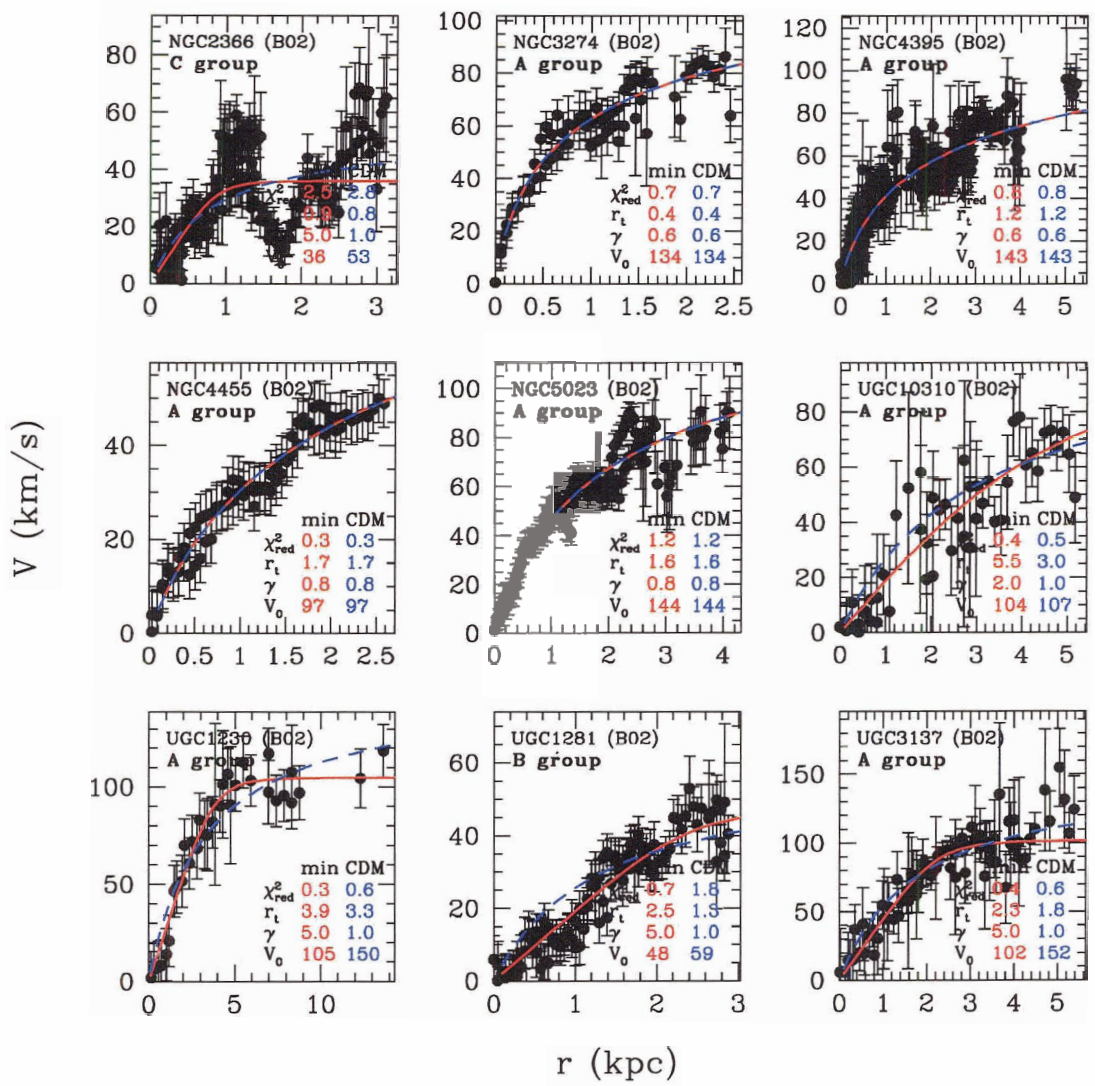

Figure B.5: e
q. 2.8 for de Blok and Bosma (2002) sample (second of three figures)] same as Figure B.4 (second of three figures).

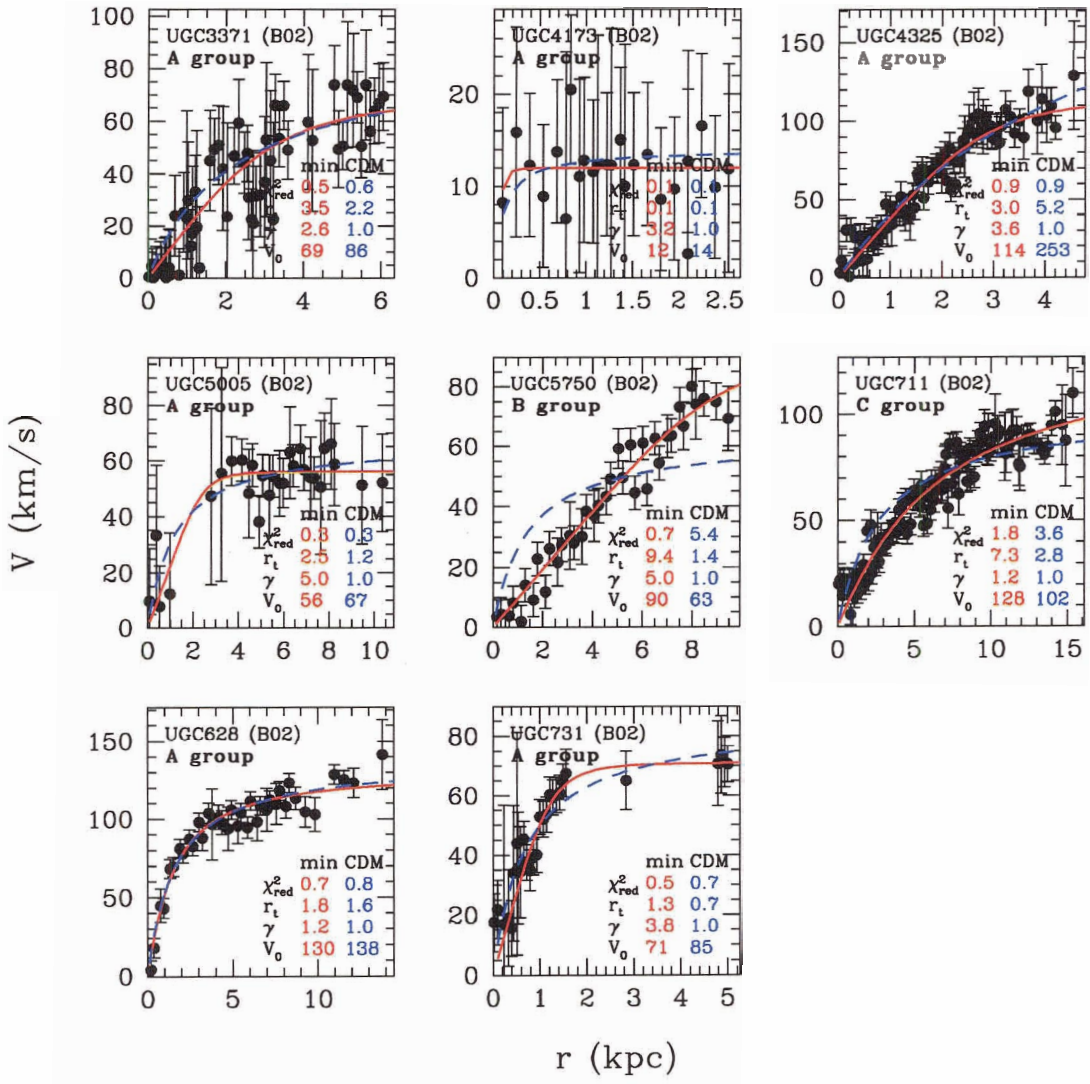

Figure B.6: e
q. 2.8 for de Blok and Bosma (2002) sample (third of three figures)] same as Figure B.4 (third of three figures).

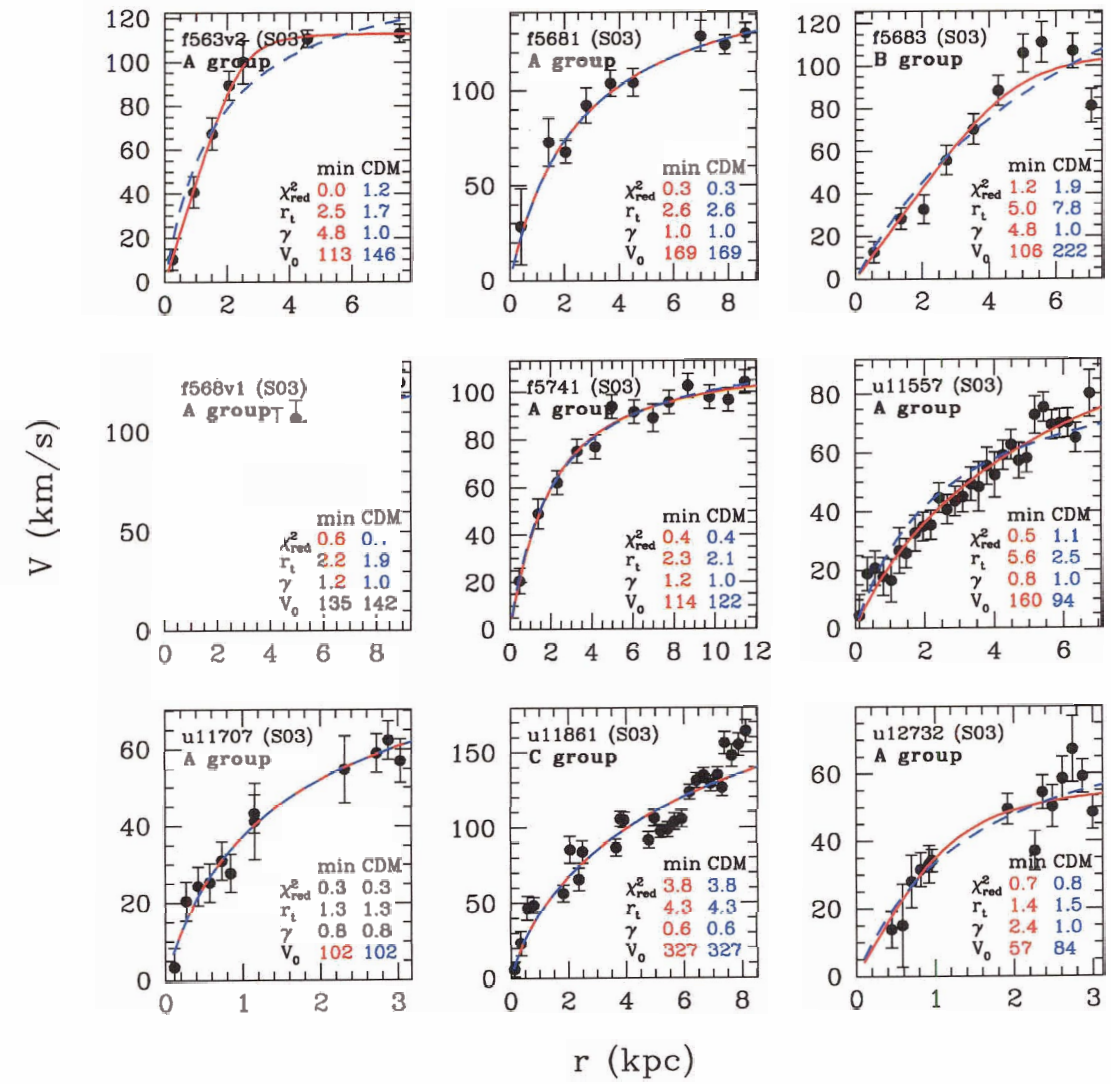

Figure B.7: e

q. 2.8 for Swaters et al. (2003a) sample (first of two figures)] same as Figure B.1 but for LSB galaxies from the sample of Swaters et al. (2003a, S03) (first of two figures).

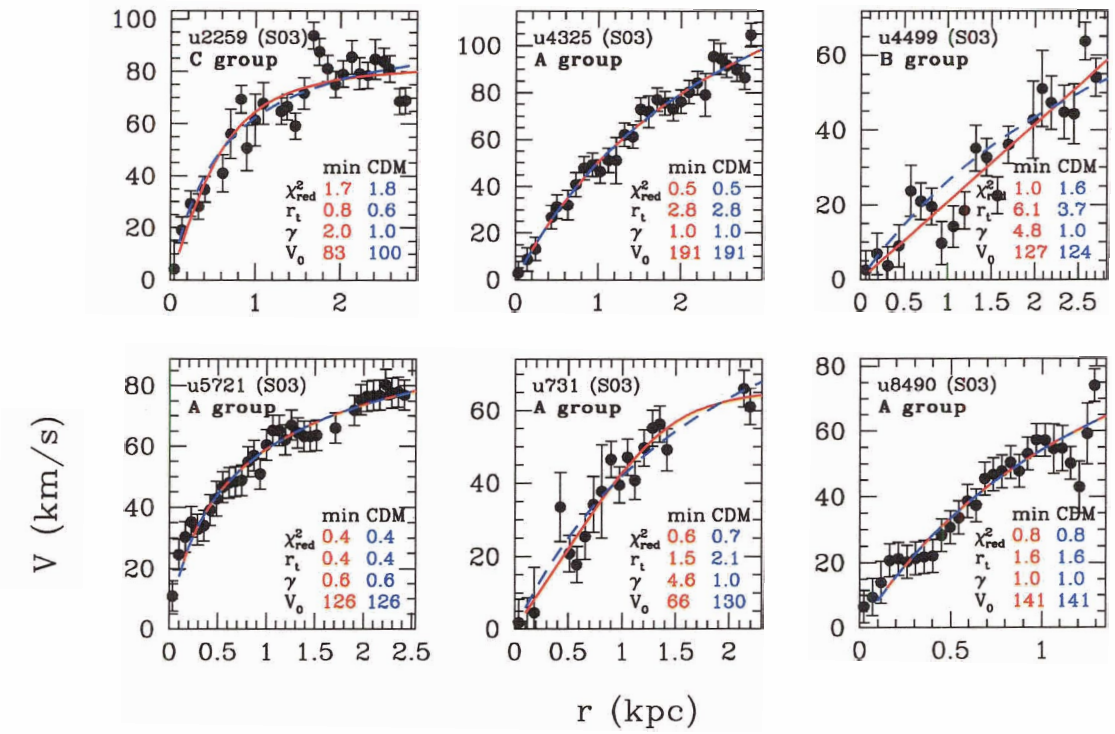

Figure B.8: e
q. 2.8 for Swaters et al. (2003a) sample (second of two figures)] same as Figure B.7 (second of two figures).

Bibliography

Aguirre, A., Burgess, C. P., Friedland, A., and Nolte, D.: 2001, *Class. Quant. Grav.* **18**, R223, Preprint [hep-ph/0105083]

Aguirre, A., Schaye, J., and Quataert, E.: 2001, *Astrophys. J.* **561**, 550

Alam, S. M. K., Bullock, J. S., and Weinberg, D. H.: 2002, *Astrophys. J.* **572**, 34

Avila-Reese, V., Colín, P., Valenzuela, O., D'Onghia, E., and Firmani, C.: 2001, *Astrophys. J.* **559**, 516

Babcock, H. W.: 1939, *Lick Observatory Bulletin* **498**, 41

Bardeen, J. M., Bond, J. R., Kaiser, N., and Szalay, A. S.: 1986, *Astrophys. J.* **304**, 15

Barnes, J. and Efstathiou, G.: 1987, *Astrophys. J.* **319**, 575

Beauvais, C. and Bothun, G.: 1999, *Astrophys. J. Supp.* **125**, 99

Bennett, C. L., Halpern, M., Hinshaw, G., Jarosik, N., Kogut, A., Limon, M., Meyer, S. S., Page, L., Spergel, D. N., Tucker, G. S., Wollack, E., Wright, E. L., Barnes, C., Greason, M. R., Hill, R. S., Komatsu, E., Nolta, M. R., Odegard, N., Peiris, H. V., Verde, L., and Weiland, J. L.: 2003, *Astrophys. J. Supp.* **148**, 1

Berezinsky, V. S., Bottino, A., and Mignola, G.: 1994, *Physics Letters B* **325**, 136

Berezinsky, V. S., Gurevich, A. V., and Zybin, K. P.: 1992, *Physics Letters B* **294**, 221

Binney, J.: 2004, in *Dark Matter in Galaxies*, IAU Symposium No. 220

Blais-Ouellette, S., Amram, P., and Carignan, C.: 2001, *Astron. J.* **121**, 1952

Blumenthal, G. R., Faber, S. M., Primack, J. R., and Rees, M. J.: 1984, *Nature* **311**, 517

Bolatto, A. D., Leroy, A., Simon, J. D., and Blitz, L.: 2001, *Bulletin of the American Astronomical Society* **33**, 816

Bolatto, A. D., Simon, J. D., Leroy, A., and Blitz, L.: 2002, *Astrophys. J.* **565**, 238

Bothun, G., Impey, C., and McGaugh, S.: 1997, *PASP* **109**, 745

Bullock, J. S., Kolatt, T. S., Sigad, Y., Somerville, R. S., Kravtsov, A. V., Klypin, A. A., Primack, J. R., and Dekel, A.: 2001, *Mon. Not. R. Astron. Soc.* **321**, 559

Bullock, J. S., Kravtsov, a. A. V., and Colín, P.: 2002, *Astrophys. J.* **564**, L1

Burkert, A.: 1995, *Astrophys. J.* **447**, L25+

Côté, S., Carignan, C., and Freeman, K. C.: 2000, *Astron. J.* **120**, 3027

Calcáneo-Roldán, C. and Moore, B.: 2000, *Phys. Rev. D* **62(12)**, 123005

Cole, S. and Lacey, C.: 1996, *Mon. Not. R. Astron. Soc.* **281**, 716

Courteau, S.: 1997, *Astron. J.* **114**, 2402

Crone, M. M., Evrard, A. E., and Richstone, D. O.: 1994, *Astrophys. J.* **434**, 402

Davis, M., Efstathiou, G., Frenk, C. S., and White, S. D. M.: 1985, *Astrophys. J.* **292**, 371

de Blok, W. J. G. and Bosma, A.: 2002, *Astron. & Astrophys.* **385**, 816

de Blok, W. J. G., McGaugh, S. S., Bosma, A., and Rubin, V. C.: 2001a, *Astrophys. J.* **552**, L23

de Blok, W. J. G., McGaugh, S. S., and Rubin, V. C.: 2001b, *Astron. J.* **122**, 2396

Debattista, V. P. and Sellwood, J. A.: 1998, *Astrophys. J.* **493**, L5+

Dekel, A., Arad, I., Devor, J., and Birnboim, Y.: 2003a, *Astrophys. J.* **588**, 680

Dekel, A., Devor, J., and Hetzroni, G.: 2003b, *Mon. Not. R. Astron. Soc.* **341**, 326

Dubinski, J. and Carlberg, R. G.: 1991, *Astrophys. J.* **378**, 496

Eke, V. R., Navarro, J. F., and Steinmetz, M.: 2001, *Astrophys. J.* **554**, 114

El-Zant, A., Shlosman, I., and Hoffman, Y.: 2001, *Astrophys. J.* **560**, 636

El-Zant, A. A., Hoffman, Y., Primack, J., Combes, F., and Shlosman, I.: 2004, *Flat-Cored Dark Matter in Cuspy Clusters of Galaxies*, Preprint [astro-ph/0309412]

Ferrarese, L. and Merritt, D.: 2000, *Astrophys. J.* **539**, L9

Fillmore, J. A. and Goldreich, P.: 1984, *Astrophys. J.* **281**, 1

Finzi, A.: 1963, *Mon. Not. R. Astron. Soc.* **127**, 21

Flores, R. A. and Primack, J. R.: 1994, *Astrophys. J.* **427**, L1

Frenk, C. S., White, S. D. M., Davis, M., and Efstathiou, G.: 1988, *Astrophys. J.* **327**, 507

Frenk, C. S., White, S. D. M., Efstathiou, G., and Davis, M.: 1985, *Nature* **317**, 595

Fukugita, M., Hogan, C. J., and Peebles, P. J. E.: 1998, *Astrophys. J.* **503**, 518

Fukushige, T., Kawai, A., and Makino, J.: 2003, Preprint [astro-ph/0306203]

Fukushige, T. and Makino, J.: 1997, *Astrophys. J.* **477**, L9

Fukushige, T. and Makino, J.: 2001, *Astrophys. J.* **557**, 533

Gebhardt, K., Bender, R., Bower, G., Dressler, A., Faber, S. M., Filippenko, A. V., Green, R., Grillmair, C., Ho, L. C., Kormendy, J., Lauer, T. R., Magorrian, J., Pinkney, J., Richstone, D., and Tremaine, S.: 2000, *Astrophys. J.* **539**, L13

Ghigna, S., Moore, B., Governato, F., Lake, G., Quinn, T., and Stadel, J.: 2000, *Astrophys. J.* **544**, 616

Gnedin, O. Y. and Zhao, H.: 2002, *Mon. Not. R. Astron. Soc.* **333**, 299

Gunn, J. E. and Gott, J. R. I.: 1972, *Astrophys. J.* **176**, 1

Hayashi, E.: 2001, *M.Sc. Thesis*

Hayashi, E., Navarro, J. F., Power, C., Jenkins, A., Frenk, C., White, S. D. M., Springel, V., Stadel, J., and Quinn, T.: 2003, Preprint [astro-ph/0310576]

Hoffman, Y. and Shaham, J.: 1985, *Astrophys. J.* **297**, 16

Holley-Bockelmann, K., Weinberg, M., and Katz, N.: 2003, Preprint [astro-ph/0306374]

Hubble, E. P.: 1936, *Realm of the Nebulae*, Yale University Press

Huss, A., Jain, B., and Steinmetz, M.: 1999, *Astrophys. J.* **517**, 64

Jimenez, R., Verde, L., and Oh, S. P.: 2003, *Mon. Not. R. Astron. Soc.* **339**, 243

Jing, Y. P., Mo, H. J., Borner, G., and Fang, L. Z.: 1995, *Mon. Not. R. Astron. Soc.* **276**, 417

Jing, Y. P. and Suto, Y.: 2000, *Astrophys. J.* **529**, L69

Jing, Y. P. and Suto, Y.: 2002, *Astrophys. J.* **574**, 538

Kaplinghat, M. and Turner, M.: 2002, *Astrophys. J.* **569**, L19

Katz, N., Hernquist, L., and Weinberg, D. H.: 1992, *Astrophys. J.* **399**, L109

Katz, N., Weinberg, D. H., and Hernquist, L.: 1996, *Astrophys. J. Supp.* **105**, 19

Klypin, A., Kravtsov, A. V., Bullock, J. S., and Primack, J. R.: 2001, *Astrophys. J.* **554**, 903

Klypin, A., Kravtsov, A. V., Valenzuela, O., and Prada, F.: 1999, *Astrophys. J.* **522**, 82 (K99a)

Kravtsov, A. V., Klypin, A. A., Bullock, J. S., and Primack, J. R.: 1998, *Astrophys. J.* **502**, 48

Lacey, C. and Cole, S.: 1993, *Mon. Not. R. Astron. Soc.* **262**, 627

Łokas, E. L. and Hoffman, Y.: 2000, *Astrophys. J.* **542**, L139

Lyubimov, V. A., Novikov, E. G., Nozik, V. Z., Tretyakov, E. F., and Kosik, V. S.: 1980, *Phys. Lett.* **B94**, 266

Mathewson, D. S., Ford, V. L., and Buchhorn, M.: 1992, *Astrophys. J. Supp.* **81**, 413

McGaugh, S. S., Barker, M. K., and de Blok, W. J. G.: 2003, *Astrophys. J.* **584**, 566

McGaugh, S. S. and de Blok, W. J. G.: 1998, *Astrophys. J.* **499**, 41

McGaugh, S. S., Rubin, V. C., and de Blok, W. J. G.: 2001, *Astron. J.* **122**, 2381 (M01)

Merrifield, M. R., in *Dark Matter in Galaxies*, IAU Symposium No. 220

Merritt, D. and Cruz, F.: 2001, *Astrophys. J.* **551**, L41

Milgrom, M.: 1983a, *Astrophys. J.* **270**, 384

Milgrom, M.: 1983b, *Astrophys. J.* **270**, 365

Milosavljević, M. and Merritt, D.: 2001, *Astrophys. J.* **563**, 34

Mo, H. J., Mao, S., and White, S. D. M.: 1998, *Mon. Not. R. Astron. Soc.* **295**, 319

Moore, B.: 1994, *Nature* **370**, 629

Moore, B., Calcáneo-Roldán, C., Stadel, J., Quinn, T., Lake, G., Ghigna, S., and Governato, F.: 2001, *Phys. Rev. D* **64**, 063508

Moore, B., Ghigna, S., Governato, F., Lake, G., Quinn, T., Stadel, J., and Tozzi, P.: 1999a, *Astrophys. J.* **524**, L19 (M99)

Moore, B., Governato, F., Quinn, T., Stadel, J., and Lake, G.: 1998, *Astrophys. J.* **499**, L5

Moore, B., Quinn, T., Governato, F., Stadel, J., and Lake, G.: 1999b, *Mon. Not. R. Astron. Soc.* **310**, 1147

Navarro, J. F.: 2003, in J. Makino and P.Hut (eds.), *Astrophysical SuperComputing using Particles*, pp 261–+, IAU Symposium No. 208

Navarro, J. F., Eke, V. R., and Frenk, C. S.: 1996a, *Mon. Not. R. Astron. Soc.* **283**, L72

Navarro, J. F., Frenk, C. S., and White, S. D. M.: 1995, *Mon. Not. R. Astron. Soc.* **275**, 720

Navarro, J. F., Frenk, C. S., and White, S. D. M.: 1996b, *Astrophys. J.* **462**, 563 (NFW)

Navarro, J. F., Frenk, C. S., and White, S. D. M.: 1997, *Astrophys. J.* **490**, 493

Navarro, J. F., Hayashi, E., Power, C., Jenkins, A. R., Frenk, C. S., White, S. D. M., Springel, V., Stadel, J., and Quinn, T. R.: 2004, *Mon. Not. R. Astron. Soc.* **349**, 1039

Nusser, A. and Sheth, R. K.: 1999, *Mon. Not. R. Astron. Soc.* **303**, 685

Ostriker, J. P. and Peebles, P. J. E.: 1973, *Astrophys. J.* **186**, 467

Ostriker, J. P., Peebles, P. J. E., and Yahil, A.: 1974, *Astrophys. J.* **193**, L1

Peacock, J. A.: 1999, *Cosmological physics*, Cambridge University Press

Peccei, R. D. and Quinn, H. R.: 1977, *Phys. Rev. D* **16**, 1791

Peebles, P. J. E.: 1982, *Astrophys. J.* **263**, L1

Perlmutter, S., Aldering, G., Goldhaber, G., Knop, R. A., Nugent, P., Castro, P. G., Deustua, S., Fabbro, S., Goobar, A., Groom, D. E., Hook, I. M., Kim, A. G., Kim, M. Y., Lee, J. C., Nunes, N. J., Pain, R., Pennypacker, C. R., Quimby, R., Lidman, C., Ellis, R. S., Irwin, M., McMahon, R. G., Ruiz-Lapuente, P., Walton, N., Schaefer, B., Boyle, B. J., Filippenko, A. V., Matheson, T., Fruchter, A. S., Panagia, N., Newberg, H. J. M., Couch, W. J., and The Supernova Cosmology Project: 1999, *Astrophys. J.* **517**, 565

Power, C., Navarro, J. F., Jenkins, A., Frenk, C. S., White, S. D. M., Springel, V., Stadel, J., and Quinn, T.: 2003, *Mon. Not. R. Astron. Soc.* **338**, 14 (P03)

Quinn, P. J., Salmon, J. K., and Zurek, W. H.: 1986, *Nature* **322**, 329

Rhee, G., Klypin, A., and Valenzuela, O.: 2003, Preprint [astro-ph/0311020]

Ricotti, M.: 2003, *Mon. Not. R. Astron. Soc.* **344**, 1237

Riess, A. G., Filippenko, A. V., Challis, P., Clocchiatti, A., Diercks, A., Garnavich, P. M., Gilliland, R. L., Hogan, C. J., Jha, S., Kirshner, R. P., Leibundgut, B., Phillips, M. M., Reiss, D., Schmidt, B. P., Schommer, R. A., Smith, R. C., Spyromilio, J., Stubbs, C., Suntzeff, N. B., and Tonry, J.: 1998, *Astron. J.* **116**, 1009

Roberts, M. S. and Whitehurst, R. N.: 1975, *Astrophys. J.* **201**, 327

Rogstad, D. H. and Shostak, G. S.: 1972, *Astrophys. J.* **176**, 315

Rosenberg, L. J.: 1998, *Proceedings of the National Academy of Science* **95**, 59

Rubin, V. C. and Ford, W. K. J.: 1970, *Astrophys. J.* **159**, 379

Sand, D. J., Treu, T., Smith, G. P., and Ellis, R. S.: 2004, *Astrophys. J.* **604**, 88

Sanders, R. H.: 1984, *Astron. & Astrophys.* **136**, L21

Sanders, R. H. and McGaugh, S. S.: 2002, *Annual Review of Astron. & Astrophys* **40**, 263

Seljak, U. and Zaldarriaga, M.: 1996, *Astrophys. J.* **469**, 437

Sellwood, J. A.: 2003, *Astrophys. J.* **587**, 638

Sellwood, J. A. and Kosowsky, A.: 2001, in *ASP Conf. Ser. 240: Gas and Galaxy Evolution*, pp 311–+

Simon, J. D., Bolatto, A. D., Leroy, A., and Blitz, L.: 2003, *Astrophys. J.* **596**, 957

Spergel, D. N. and Steinhardt, P. J.: 2000, *Physical Review Letters* **84**, 3760

Springel, V., Yoshida, N., and White, S. D. M.: 2001, *New Astronomy* **6**, 79

Stadel, J. G.: 2001, *Ph.D. thesis*, University of Washington

Stoehr, F.: 2004, Preprint [astro-ph/0403077]

Stoehr, F., White, S. D. M., Springel, V., Tormen, G., and Yoshida, N.: 2003, *Mon. Not. R. Astron. Soc.* **345**, 1313

Stoehr, F., White, S. D. M., Tormen, G., and Springel, V.: 2002, *Mon. Not. R. Astron. Soc.* **335**, L84

Subramanian, K.: 2000, *Astrophys. J.* **538**, 517

Subramanian, K., Cen, R., and Ostriker, J. P.: 2000a, *Astrophys. J.* **538**, 528

Subramanian, K., Cen, R., and Ostriker, J. P.: 2000b, *Astrophys. J.* **538**, 528

Swaters, R. A., Madore, B. F., and Trewhella, M.: 2000, *Astrophys. J.* **531**, L107

Swaters, R. A., Madore, B. F., van den Bosch, F. C., and Balcells, M.: 2003a, *Astrophys. J.* **583**, 732 (S03)

Swaters, R. A., Verheijen, M. A. W., Bershady, M. A., and Andersen, D. R.: 2003b, *Astrophys. J.* **587**, L19

Syer, D. and White, S. D. M.: 1998, *Mon. Not. R. Astron. Soc.* **293**, 337

Taylor, J. E. and Navarro, J. F.: 2001, *Astrophys. J.* **563**, 483

Taylor, J. E. and Silk, J.: 2003, *Mon. Not. R. Astron. Soc.* **339**, 505

Thomas, P. A., Colberg, J. M., Couchman, H. M. P., Efstathiou, G. P., Frenk, C. S., Jenkins, A. R., Nelson, A. H., Hutchings, R. M., Peacock, J. A., Pearce, F. R., and White, S. D. M.: 1998, *Mon. Not. R. Astron. Soc.* **296**, 1061

Tohline, J. E.: 1983, in *IAU Symp. 100: Internal Kinematics and Dynamics of Galaxies*, pp 205–+

Turner, M. S.: 1999, in M. Campbell and T. Wells (eds.), *The Proceedings of Physics in Collision*, IAU Symposium No. 208, Preprint [astro-ph/9912211]

Tyson, J. A., Kochanski, G. P., and dell'Antonio, I. P.: 1998, *Astrophys. J.* **498**, L107+

van den Bergh, S.: 1999, *PASP* **111**, 657

van den Bosch, F. C., Robertson, B. E., Dalcanton, J. J., and de Blok, W. J. G.: 2000, *Astron. J.* **119**, 1579

van den Bosch, F. C. and Swaters, R. A.: 2001, *Mon. Not. R. Astron. Soc.* **325**, 1017

Wadsley, J. W., Stadel, J., and Quinn, T.: 2004, *New Astronomy* **9**, 137

Wagoner, R. V., Fowler, W. A., and Hoyle, F.: 1967, *Astrophys. J.* **148**, 3

Warren, M. S., Quinn, P. J., Salmon, J. K., and Zurek, W. H.: 1992, *Astrophys. J.* **399**, 405

Wechsler, R. H., Bullock, J. S., Primack, J. R., Kravtsov, A. V., and Dekel, A.: 2002, *Astrophys. J.* **568**, 52

Weinberg, M. D.: 2001a, *Mon. Not. R. Astron. Soc.* **328**, 311

Weinberg, M. D.: 2001b, *Mon. Not. R. Astron. Soc.* **328**, 321

Weinberg, M. D. and Katz, N.: 2002, *Astrophys. J.* **580**, 627

White, S. D. M.: 1976, *Mon. Not. R. Astron. Soc.* **177**, 717

White, S. D. M., Davis, M., and Frenk, C. S.: 1984, *Mon. Not. R. Astron. Soc.* **209**, 27P

White, S. D. M., Frenk, C. S., and Davis, M.: 1983, *Astrophys. J.* **274**, L1

White, S. D. M., Frenk, C. S., Davis, M., and Efstathiou, G.: 1987, *Astrophys. J.* **313**, 505

White, S. D. M. and Rees, M. J.: 1978, *Mon. Not. R. Astron. Soc.* **183**, 341

White, S. D. M. and Zaritsky, D.: 1992, *Astrophys. J.* **394**, 1

Yoshida, N., Sheth, R. K., and Diaferio, A.: 2001, *Mon. Not. R. Astron. Soc.* **328**, 669

Zentner, A. R. and Bullock, J. S.: 2002, *Phys. Rev. D* **66**, 43003

Zwicky, F.: 1933, *Helvetica Phys. Acta* **6**, 110